2021

# Equation of State and Shear Strength Studies on Transition Metals and Mransition Metal Borides

Kaleb C. Burrage
*University Of Alabama At Birmingham*

# EQUATION OF STATE AND SHEAR STRENGTH STUDIES ON TRANSITION METALS AND TRANSITION METAL BORIDES

by

KALEB C. BURRAGE

YOGESH K. VOHRA, COMMITTEE CHAIR
SHANE AARON CATLEDGE
CHENG-CHIEN CHEN
PATRICIA KALITA
HAIBIN NING

A DISSERTATION

Submitted to the graduate faculty of The University of Alabama at Birmingham,
in partial fulfillment of the requirements for the degree of
Doctor of Philosophy

BIRMINGHAM, ALABAMA

2021

EQUATION OF STATE AND SHEAR STRENGTH STUDIES ON TRANSITION METALS AND TRANSITION METAL BORIDES

KALEB C. BURRAGE

PHYSICS

ABSTRACT

This work employs a broad and in-depth range of experimental x-ray diffraction techniques to probe anisotropic compression effects and shear deformation behavior in transition metals and their borides to ultra-high pressures. These techniques include the custom designed toroidal diamond anvils fabricated by focused ion beam machining to compress samples to pressure of 358 GPa equating to that at the Earth's core. This has been used to generate a new equation of state for *Ta* metal for pressure calibration within the field of high-pressure physics and test the validation of other pressure calibrations claiming > 500 GPa of pressure. This has also enabled high pressure studies on *Re* and *Os*-based metal borides that have shown considerable strength and incompressibility rivaling that of diamond to pressures 3-5 times greater than any previous studies.

The techniques within this work include the employment of Radial X-ray Diffraction and Lattice Strain Theory to determine hydrostatic compression and shear strength measurements on transition metal Os and transition metal boride $ReB_2$. This technique has allowed the validation of Density Functional Theory (DFT) calculations by estimating hydrostatic compression parameters (pressure, volume) for accurate theory-experiment comparisons. These hydrostatic experimental measurements have elucidated details of anomalies present within lattice parameters of *Os* under compression and

anisotropic compression documented in $ReB_2$ and $Os_2B_3$ by comparison with non-hydrostatic compression studies and DFT.

Finally, high pressure and high temperature studies on transition metal boride $Os_2B_3$ were conducted to 5.4 GPa and 1273 K to map out the thermal equation of state and determine its mechanical properties and thermal expansion coefficients at high temperatures. The thermal phase stability and high strength have suggested the use of this material into hypersonic engine devices, high strength coatings, and industrial tools. The experiments conducted in these studies were done in collaboration with major national laboratories such as Argonne National Laboratory and Los Alamos National Laboratory and provided for the first-time anisotropic compression data and shear strength data on transition metals and their borides under extreme environments.

Keywords: High Pressures, Toroidal Diamond Anvils, Transition Metal Borides, X-ray Diffraction, Shear Strength, Equation of State

DEDICATION

*"To He who made this world and all of its marvelous mysteries, who imparted a love of knowledge and gave His love to me, Jesus Christ…"*

ACKNOWLEDGMENTS

I would like to provide my sincere gratitude to all of those who have contributed to the work presented here. For help, guidance, collaboration and insight, your help has made this work possible.

To Dr. Yogesh Vohra, who has acted as a mentor and guided my career in materials science with insight, a special thanks is due. Your guidance has provided professional opportunities and collaborations that have undoubtedly led to the success of the works presented here. Your professionalism and high standard of research conduct will carry over with me to the next season of my career, of which I hope remains in close contact. It has been a pleasure to be associated as one of your graduate students.

To Patricia Kalita, Chris Seagle, and the other staff scientists at Sandia National Laboratories, I would like to extend my gratitude for the opportunity of interning these last two years. Your patience and guidance provided me with worthwhile experiences in the research conduct that is expected at major national laboratories. Your mentorship and professional advice culminated into a successful acceptance into a post-doctoral position at Oak Ridge National Laboratories. Thank you for all the support, and I hope to remain in contact and wish you all success.

To my research committee, thank you for your time and suggestions for the formation and defense of this work. To Dr. Cheng-Chien Chen, thank you for all the work in theoretical calculations that have resulted in many collaborative publications. Your work and your graduate students have seriously impressed me with their

professionalism. To Dr. Aaron Catledge, thank you for your insight and collaboration into transition metal borides and high entropy alloys that have provided collaborative efforts into a new and intriguing field of materials science. I look forward to future works and publications. And to Dr. Haibin Ning, thank you for your support in this dissertation and your professional courtesy and suggestions on my thesis proposal and defense.

I would like to thank the funding agencies for their contributions to this dissertation. To the National Nuclear Security Administration (NNSA Grant No. DE-NA0003916), US National Science Foundation (NSF Grant No. DMR-10904164), and the US Department of Education (GAANN Grant No. P200A180001) special thanks are given for the support of this work.

I would also like to thank the staff scientists at the High Pressure Collaborative Access Team (HPCAT), Advanced Photon Source (APS), Argonne National Laboratory for their assistance with high pressure and x-ray diffraction experiments. Your help and expertise have provided high quality experimental methods and data and contributed to the success of the published works and this dissertation.

Finally, to my parents who instilled a love of learning within me at a young age, thank you for all the support and guidance that has made this work possible. Your guidance and love all these years paid off as I now reach the height of academic achievement. In hopes this work has made you proud.

TABLE OF CONTENTS

*Page*

LIST OF TABLES

LIST OF FIGURES

*Figures* *Page*

## LIST OF ABBREVIATIONS

| | |
|---|---|
| BM | Birch-Murnaghan |
| CIF` | Crystallographic Information File |
| DAC | Diamond Anvil Cell |
| DFT | Density Functional Theory |
| DOS | Density of States |
| EDXD | Energy Dispersive X-ray Diffraction |
| EoS | Equation of State |
| FIB | Focused Ion Beam |
| HEA | High Entropy Alloy |
| HEB | High Entropy Boride |
| HP | High Pressure |
| HPHT | High Pressure High Temperature |
| LANL | Los Alamos National Laboratory |
| LTS | Lattice Strain Theory |
| NCD | Nano-Crystalline Diamond |
| NHS | Non-Hydrostatic Stress |
| NPD | Nano-Polycrystalline Diamond |
| PE Press | Paris-Edinburgh Press |
| R-XRD | Radial X-ray Diffraction |

| | |
|---|---|
| SCD | Single Crystal Diamond |
| SEM | Scanning Electron Microscope |
| TDAC | Toroidal Diamond Anvil Cell |
| TD-1 | Toroidal Design 1 |
| TD-2 | Toroidal Design 2 |
| TMB | Transition Metal Boride |
| Tpa | TeraPascal |
| XRD | X-Ray Diffraction |

# CHAPTER 1

## INTRODUCTION–MATTER AT EXTREMES

The progress of technological advancement has been nothing short of astounding since the late 19$^{th}$ century to the present day. The production of steel and other strong transition metal alloys contributed to high rise constructions to accommodate the increase of population in major cities while the creation of advanced transportation like intercontinental jets, commercial freight, and automobile engines allowed commerce to flourish. Imbedded within these technological achievements are decades of material studies to ensure the survivability and extended use of equipment. Most of modern architecture, abrasives, national security devices, and aircraft engines are subject to extreme pressures and temperatures that degrade, erode, fracture, or induce crystallographic phase transitions that can weaken or change the mechanical behavior of alloys and composite materials. Understanding the mechanical deformation of select materials ensures the performance, survivability, and sustainability of high strength metals, alloys, and compounds needed for the applications listed. Research and development of materials under high pressure - high temperature (HPHT) has resulted in multi–billion-dollar industries and has proven relevant for modern technological expansion.

In particular, Group IV–VIII transition metals are used extensively in industry, as their high electron densities result in strong resistance to compression and shearing

because of Coulomb repulsive interactions. The most notable of these transition metals, in terms of incompressibility, are period 6 elements *W*, *Re*, and *Os*. By adding interstitial layers of light covalently bonded atoms to the metal crystal structure, such as boron, the strength of the material can be further enhanced because of a combination of metallic and covalent bonding resulting in a family of Transition Metal Borides (TMB's) with superior mechanical properties. The TMB's $ReB_2$, $OsB_2$, and $Os_2B_3$ are of chief interest as they boast a bulk modulus rivaling that of diamond (442 GPa) [1], but without the added difficulty of machining due to metallic nature, which enables electro-discharge machining. Thus, TMBs have possible applications to replace diamond in high strength coatings and industrial abrasives. Previous studies have also shown strong thermal stability implicating potential uses in environments such as reactors or engines [2-5]. Until recently, $ReB_2$ and $OsB_2$ have received some attention while $Os_2B_3$ has received little to none despite the superb physical properties reported [6].

The goal of this thesis focuses on anisotropic compression behavior in the family of hexagonal TMBs including $ReB_2$ and $Os_2B_3$, as well as establishing reliable x-ray pressure standards based on the equation of state of transition metal *Ta*. The high pressure–high temperature behavior of $Os_2B_3$ is documented to 5.4 GPa and 1273 K, while the high pressure shear strength behavior is studied in $ReB_2$ and *Os* metal. To accomplish this, novel toroidal-diamond anvil cell (T-DAC) technology has been combined with synchrotron X-ray Diffraction (XRD) to compress materials to near center of the Earth pressures. Energy Dispersive X-ray Diffraction (EDXD), and Radial-XRD (R-XRD) techniques are utilized. The objectives of this study can be summarized in three major aims:

1. Determine the achievable pressure ranges of custom-made T-DACs in comparison with conventional two-stage diamond anvils
2. Determine the anisotropic compression and anomalies in axial (c/a) ratio in hexagonal phase of TMBs and *Os* metal both in hydrostatic and non-hydrostatic environments
3. Comparison of theoretical and experimental shear strength measurements of TMB $ReB_2$ and *Os* metal.

The culmination of this thesis has resulted in multiple collaborations with major national laboratories, resulting in 7 publications with 2 articles submitted for review. [7-15].

# CHAPTER 2

# THE DIAMOND ANVIL CELL

## 2.1 Introduction

The need to study materials under high pressure for applications into national defense, geology, and industrial applications necessitated the search for a reliable compression mechanism. Naturally, researchers in the mid-20$^{th}$ century turned to single crystalline diamond (SCD) to be used as an anvil for ultra-high-pressure generation. Diamond is chemically inert and resistant to damaging radiation, allowing samples that are corrosive, toxic, or reactive to be safely studied while reducing sample contamination. SCD boasts a yield strength of 130 - 140 GPa [16] and has a superb resistance to volumetric incompressibility with a bulk modulus of 442 GPa [17]. These strong physical properties combined with optical transparency of diamond to visible and infrared radiation make diamond the quintessential choice for high pressure spectroscopy and diffraction.

The progress of the diamond anvil cell (DAC) from its first conception to modern day has increased the achievable pressure threshold from ~3 GPa to well above half a TeraPascal (1TPa = 1000 GPa) (the pressure at the center of the Earth is estimated ~350 GPa). Many techniques have been developed to determine sample pressure within a DAC with the most common being ruby fluorescence, x-ray diffraction, and Raman scattering. The DAC can also be used for simultaneous heating and pressure experiments with

multiple methods for laser heating at high pressures. There are some limitations to this, however, as diamond anvils will burn in air around 800 °C and require a vacuum environment or further insulation to ensure diamond survival at higher temperatures. Methods used to work around this makes use of diamond's optical ability to heat samples above 2000 °C by double-sided laser heating [18].

## 2.2 Beveled Diamond Anvils

A typical modern DAC is illustrated in Figure 1.1 (a). Two diamonds are situated on tungsten carbide or cubic boron nitride seats, while the culets (flat tips) of the diamonds are aligned under a microscope. A gasket material typically comprising of a strong metal, such as rhenium or steel, is indented by the diamond anvils to create a fitted seat for sample placement while also testing the stability of the aligned anvils under load.

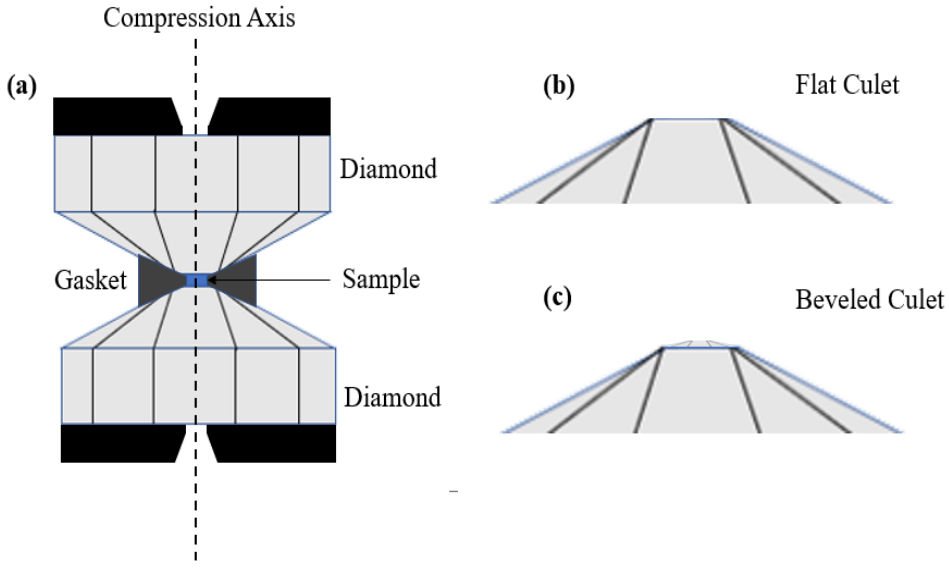


Figure 1. (a) Illustrated diagram of the Diamond Anvil Cell with sample placement and gasket. (b) The tip of a diamond culet with a flat design. (c) Illustration of a beveled culet design.

A sample hole is drilled within the gasket for sample placement centered on the two diamond culets. The mounted gaskets are essential for preventing sample outflow during compression while also reducing the diamonds from contacting each other. The elastic deformation of diamond at ultrahigh pressures can lead to cupping of anvils resulting in diamond-diamond contact and large pressure gradients resulting in failure of diamond anvils. Original designs of the DAC used a flat culet area illustrated in Figure 1.1 (b) for compression. Though useful and easier to align, the larger surface diameter (~1mm) reduced the achievable pressure to a few GPa. Decreasing the diameter to 100-200 microns saw an increase in pressure limitation to ~150 GPa while the creation of a new beveled diamond culet allowed for pressures to reach up to 250-400 GPa [18]. These new designs introduced a bevel to the culet (Figure 1.1 (c)) that reduced the build-up of internal strain in the diamond and decreasing the surface area. The beveled design allowed researchers to study materials to pressures two orders of magnitude higher than the original DAC design enabling ground-breaking work into near room temperature superconductors [19], geophysics in the Earth's mantle [20], and understanding deformation mechanisms seen in extreme environments.

## 2.3 X-ray Diffraction and the Diamond Anvil Cell

The ability of the Diamond Anvil Cell to reach pressures replicating that of interplanetary cores has revealed a surge in the study of materials under high pressure. The primary source of these studies, even since the early beginnings of the DAC, has been high pressure (HP) x-ray diffraction (XRD). Pressure will induce a change in the

atomic distances of a material, which can cause many forms of structural and electronic effects that exhibit profound phase changes, magnetic, and thermal properties. As such, experimentally determining any new atomic arrangement induced by pressure is highly desirable. Known as crystallography, the field of studying crystal structures of materials is often examined by use of XRD. X-rays, being waves of electromagnetic radiation, will scatter off the inter-planar d-spacings of a crystal system given the wavelength is of similar magnitude to the d-spacings. This will produce diffraction patterns as incident x-rays are diffracted at varying angles. The regular array of scatterers in a crystal system will allow for the constructive interference of radiation in specific directions as determined by Bragg's Law [21]:

$$n\lambda = 2dsin\theta \tag{1}$$

where $n$ is an integer, $\lambda$ is the x-ray wavelength, $d$ is spacing between diffracting planes, and $\theta$ is the angle of diffraction. Collected XRD experimental d-spacings with HP DAC compression allows for key understanding and derivation of how volume, lattice parameters, and elastic moduli evolve in extreme environments.

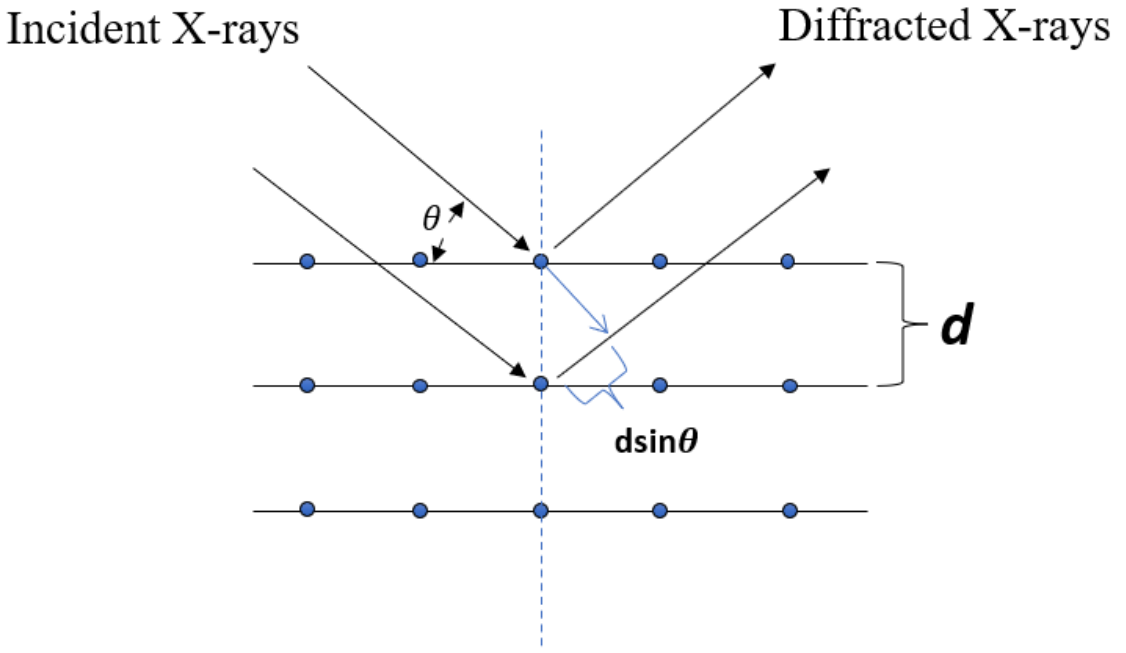


Figure 2. Illustration of x-ray diffraction off an ordered crystal system. X-rays are incident from the upper left side and are scattered from the periodic lattice. Diffracted out going x-rays (upper right) are collected and analyzed for measurement of inter-planar spacing (*d*) as indicated.

Developments in HP x-ray diffraction techniques have improved the ability to determine crystal structures in materials by decreasing the incident beam size to minimize effect of pressure gradients, increasing x-ray beam flux, and increasing sensitivity in detectors. Current beam diameters can be as low as the micrometer, with efforts currently being made to provide nanometer sized x-ray beams [22]. The increased spatial resolution due to smaller beam sizes allows for acquisition of high-quality x-ray diffraction data that can be refined to yield information on lattice parameters of crystalline phases at high pressures. This is also useful for the application of the DAC, as gasket material surrounding sample placement can interfere with larger beams and produce extraneous peaks in the collected XRD pattern.

In the design of the DAC, the diamond anvils are supported by a tungsten carbide and boron nitride seat and are situated so that the incident x-rays propagate along the compression axis. The tungsten carbide seat is placed upstream of the x-rays while the low z-material boron nitride is placed downstream of the incident x-rays to allow for optimal transmission of diffracted x-rays, as seen in Figure 3. The diffracted x-rays are collected onto a detector where the angle of diffraction and intensity can be determined.

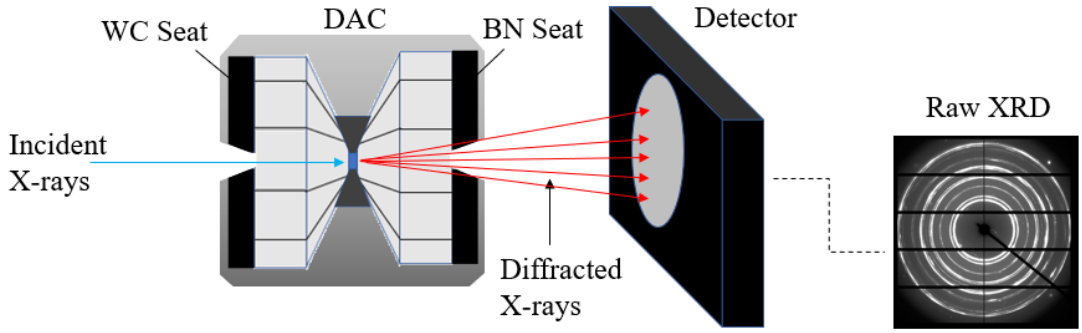


Figure 3. Schematic of XRD within a diamond anvil cell. Incident x-rays pass along the compression axis of the DAC and onto the sample. Diffracted x-rays are collected onto a detector for determination of sample crystal structure based on location of diffracted peak positions and their intensities.

The study of crystallography through use of x-rays is a form of elastic scattering where the diffracted x-rays have the same wavelength as the incident and only differ by direction. This allows for probing of atomic distribution in the sample, as opposed to inelastic scattering where energy is transferred to the material scatterers, allowing for study of material excitations. X-ray sources vary in design, energy output, and beam size, but are commonly acquired from synchrotron devices where high energy and small beam sizes are needed to study complex structures.

# CHAPTER 3

# THE TWO STAGE DIAMOND ANVIL CELL

## 3.1. Introduction

Though modern beveled diamond anvils have enabled high pressures studies into environments replicating every pressure region of the Earth's core, they have been limited by their yield strength. When internal stresses within the DAC breaches the yield strength, the diamonds undergo catastrophic failure and are often not able to be reused. These fractures generally occur around the outer edge of the diamond culets where the facets form an angle with the flat culet, as well as where the most elastic deformation is seen. Dynamic pressure experiments involving rapid shock compression of samples have achieved higher than TeraPascal (TPa) pressures, but such experiments cause intense of heating of samples and are difficult (and costly) to employ.

To extend the available static pressure ranges within the DAC, novel two stage diamond anvils were fabricated by Leonid Dubrovinsky and Natalia Dubrovinskaia in 2012 by synthesizing nano-crystalline diamond (NCD) from glassy carbon micro balls via large volume press [23]. NCD has shown slightly superior qualities of physical toughness compared to its single crystal counterpart and has since drawn attention to its applications within a DAC. Dubrovinsky et al. used two halves of a NCD micro ball as secondary anvils atop a flat diamond culet. The hemispheres provided a smaller surface area for compression and reached a claimed 600 GPa using *Re* and *Au* pressure markers.

Later experiments by this same group claimed even 1 TPa of applied pressure within a DAC using a similar design [24].

### 3.2. Nanocrystalline Diamond Fabrication at UAB

Many difficulties arose in using the NCD micro ball as a two stage DAC. In particular, the placement and alignment of the NCD hemisphere onto the culet of the SCD culet was prone to movement under compression and loading. Misalignment can be severely detrimental to the achievable pressure threshold of the two stage NCD and has resulted in the inability to reproduce the claimed 1TPa of pressure. To resolve this issue, the NCD would need to adhere to the SCD anvil below while retaining accurate placement on the culet. Research has been conducted on the growth of polycrystalline growth of NCD on SCD at the University of Alabama at Birmingham that has resulted in a highly reproducible method of spatially controlled NCD placement [25]. The diamond synthesis laboratory at UAB houses a 2-kW magnetron microwave source with a custom plasma chamber for NCD nucleation. A SCD anvil is coated with a thin tungsten mask using sputter deposition and mask-less lithography to reduce NCD nucleation in undesirable areas. A hole is etched into the tungsten mask at the location for the NCD growth to occur that can be as small as 15 microns in diameter. MPCVD is carried out at a plasma temperature held typically at 820 ℃ with gas chemistries of 9% $CH_4/H_2$, 10% $N_2/CH_4$ for the grown second stage. Two diamond anvils are made in this fashion and offer a highly reproducible method for fabrication of two stage diamond anvil that negates the difficulty of alignment because of the chemical adherence of the NCD to the

SCD. These MPCVD grown two stage DACs have shown more reasonable pressures of between 300-400 GPa [25,26].

### 3.3 Toroidal Diamond Anvils

There have been two distinct approaches in the fabrication of NCD micro-anvils: the first approach is to convert glassy carbon into NCD micro-ball by the application of high pressure and high temperatures [23,24], and the second approach has been to deposit NCD on an existing anvil by combining mask-less lithography and chemical vapor deposition (CVD) as listed above [7,8]. Even though both approaches have shown the ability to generate ultra-high pressures above 300 GPa, direct CVD growth of NCD on existing diamond anvil offers better advantages due to alignment and reproducibility in generation of ultra-high static pressures. However, the random orientation of small grain sizes (nanometer) that typically makes NCD stronger than SCD also makes visual and infrared studies difficult. Light is scattered from the random orientation and can produce weak sample signals on detector collection, which suggests that optimizing SCD anvil techniques to generate higher pressure may be more suitable.

There have been further developments in generating ultra-high pressures by employing focused-ion beam (FIB) shaping to fabricate micro-anvils from single crystal diamond and nano-polycrystalline diamond (NPD) [27–29]. Instead of depositing or placing a second stage diamond until the anvil culet, a second stage is formed from the SCD anvil itself. Very recently, FIB has been utilized to fabricate toroidal diamond anvils to achieve a pressure of ~600 GPa on *Re* metal [30,31]. These toroidal diamond anvils circumvent problems associated with the large elastic deformation experienced by

diamond at multi-megabar pressures. Typical cleaving of SCD anvils occurs along the {110} planes oriented parallel to the compressive stress along the [001] axis in DAC experiments and suggests that by reducing the shear stress lower than the yield strength of diamond (130 GPa) would lead to achieving higher pressures. These toroidal diamond anvil cells (TDAC) have two major advantages: (1) toroidal shape helps prevent sample outflow during compression and (2) reducing internal shear stresses in the diamond anvil.

# CHAPTER 4

# LATTICE STRAIN THEORY

## 4.1. Introduction

A sample under compression within a DAC can be described by a stress state split into radial and axial components [32]. Maximum stress is exerted along the compressive axis of the DAC with a minimum stress being exerted radially inward from the gasket. The asymmetrical stress combined with the limited shear strength of the sample results in a non-hydrostatic stress (NHS) state within the sample chamber. Many physical properties of a material, such as the bulk modulus (Eq. 2), is dependent on the volumetric compression $K = -\frac{V_0 dP}{dV}$ where $K$ is the bulk modulus, $V_0$ is the initial volume, and *dP/dV* is the change in pressure (*P*) per change in volume (*V*). Under non-hydrostatic stress, the volumetric strain can be larger than what is observed in more hydrostatic environments, as shown by Singh et al. [32], and can result in a variation in bulk modulus obtained from the pressure-volume data. With DAC experiments used to determine pressure-volume relations and equation of state (EoS) formation, understanding the stress state of the sample is of paramount importance for proper description of materials deformation behavior.

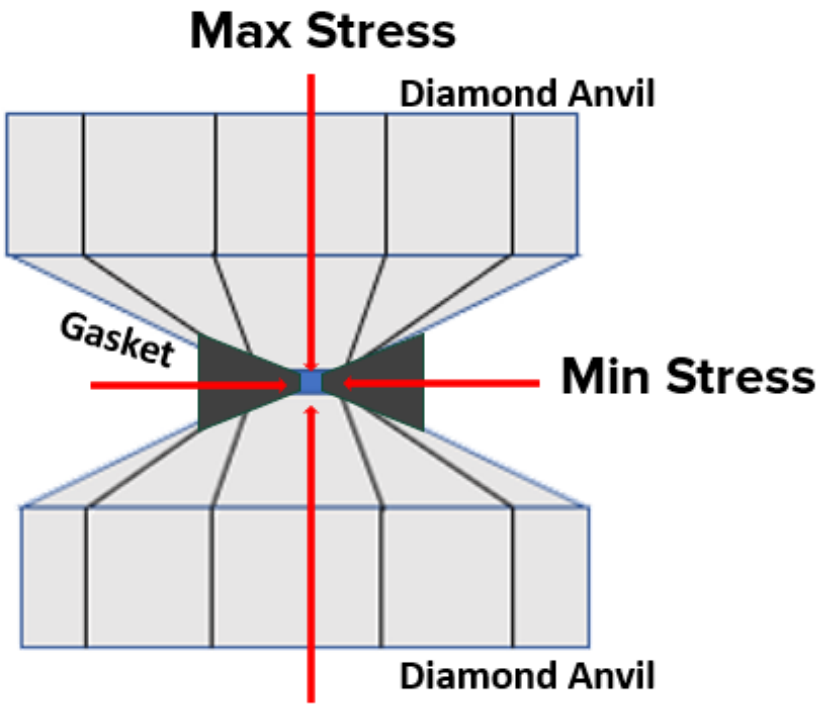


Figure 4. Schematic diagram of differential stress present during sample compression by two diamond anvils. A maximum stress is exerted along the compression axis and a minimum stress exists along the radial direction. The differential stress supported by the sample is directly proportional to its shear strength.

The Lattice Strain Theory (LST) produced by Singh et al. [32] is mostly used in this study of transition metals and transition metal borides to ascertain stress states within a sample being compressed by the DAC. LST provides a powerful method of determining hydrostatic strain components of a sample under non-hydrostatic conditions and thus allowing for accurate EoS formation for comparison with theoretical predictions. LST can also be combined with radial x-ray diffraction (R-XRD) (discussed in section 4.4) to provide an enabling technique for the study of non-hydrostatic compression effects on lattice strains in a crystalline lattice. Although an NHS environment is used to induce strain and shearing in the sample for R-XRD, lattice strain theory enables an estimation of hydrostatic components of compression and its effect on inter-planar d-spacings in the

sample material. This also provides a basis for determining the differential stress between the compression axis (max stress) and radial direction (min stress) from which shear strength, hydrostatic bulk moduli, and equations of state can be derived.

## 4.2. Derivation of Hydrostatic Pressure Values

As mentioned in the previous section, the stress state within a DAC sample chamber can be split into two parts: radial and axial. Singh et al. displays this in matrix notation:

$$\sigma_{ij} = \begin{vmatrix} \sigma_{11} & 0 & 0 \\ 0 & \sigma_{11} & 0 \\ 0 & 0 & \sigma_{33} \end{vmatrix}$$

$$= \begin{vmatrix} \sigma_P & 0 & 0 \\ 0 & \sigma_P & 0 \\ 0 & 0 & \sigma_p \end{vmatrix} + \begin{vmatrix} -t/3 & 0 & 0 \\ 0 & -t/3 & 0 \\ 0 & 0 & -t/3 \end{vmatrix}$$

$$= \sigma_P + D_{ij} \tag{4.1}$$

where the axial and radial stress components are $\sigma_{33}$ and $\sigma_{11}$, $\sigma_P$ is the hydrostatic component of stress, and $D_{ij}$ is the deviatoric (or differential) stress matrix. The differential stress between the axial and radial directions will produce a strain on the sample and can be related to the measured d-spacing $d_m(hkl)$. This is written as:

$$d_m(hkl) = d_p(hkl)[1 + (1 - 3\cos^2\psi)Q(hkl)] \tag{4.2}$$

where $d_p(hkl)$ is the d-spacing under hydrostatic pressure, $\psi$ is the angle between the cell loading axis and diffraction plane normal, and $Q(hkl)$ is the lattice strain corresponding to each *hkl*. The lattice strain term is mainly dictated by the Reuss (iso-stress) and Voigt (iso-strain) conditions for the shear modulus given by $G_R$ *(hkl)* and $G_V$ *respectively*:

$$Q\ (hkl) = \frac{t}{3}\{\alpha[2G_R(hkl)]^{-1} + (1-\alpha)(2G_V)^{-1}\} \quad (4.3)$$

Here, *t* is the differential stress in the sample, and $\alpha$ is a weighted factor of strain that varies between 0 and 1. It is then easy to see from these two equations that experimental determination of $d_m(hkl)$, $Q(hkl)$, and the angle $\psi$ can allow for the calculation of hydrostatic d-spacing $d_p(hkl)$ even while a sample is under non-hydrostatic compression.

## 4.3. Applications to Crystal Geometries

The second major advantage regarding the application of LTS would be its effective use across the seven different crystal systems. We can see that there is a dependence of measured d-spacing $d_p(hkl)$ on the relative strains found under the Reuss and Voigt conditions [32]. Particularly, $G_R\ (hkl)$ is lattice dependent and changes in calculation for different crystal geometries. Though there are seven crystal systems, only the expressions for $G_R\ (hkl)$ of the hexagonal groups are shown here as most transition metal and TMBs in this dissertation belong to this group:

a) Hexagonal System

$$[2G_R(hkl)]^{-1} = \frac{1}{2}[(2S_{11} - S_{12} - S_{13}) + l_3^2(-5S_{11} + S_{12} + 5S_{13} - S_{33} + 3S_{44}) + l_3^4(3S_{11} - 6S_{13} + 3S_{33} - 3S_{44})]$$

here, $l_3^2 = 3a^2l^2/M^2$, $M^2 = [4c^2(h^2 + hk + l^2) + 3a^2l^2]$, $S_{ij}$ are the associated elastic compliances, and the lattice parameters for the hexagonal lattice are *a* and *c*.

The difficulty associated with determining $G_R(hkl)$ is the experimental calculation of $S_{ij}$ for complex crystal systems. A popular experimental method for finding the elastic compliance constants of crystals includes measuring ultrasonic wave propagation through a material of known density. Ultrasonic measurement is a well-studied field but would include experiments beyond the DAC and XRD, which decreases feasibility if ultrasonic data was not available. Therefore, one might rely on theoretical calculations of $G_R(hkl)$ and $G_V$ to determine the degree that strain affects the measured d-spacing $d_m(hkl)$ and the hydrostatic d-spacing $d_p(hkl)$.

### 4.4. Determining Shear Strength

A simplification of $d_m(hkl)$ can be found to avoid the difficulties in shear moduli calculation discussed in the previous section. By exploiting the angle $\psi$ in a particular geometric experimental setting, $\psi = 57.3°$ can be chosen such that the $1 - 3\cos^2\psi$=0. This would allow a direct relation of $d_m(hkl) = d_p(hkl)$ to determine hydrostatic d-spacing while ignoring the lattice strain term $Q(hkl)$. However, differential stress $t$ is still a useful term as shear strength $\tau$ can be found from the relation $t = 2 * \tau$. Choosing $\alpha = 0$ such that the lattice dependent term $G_R(hkl)$ is neglected allows for the simplification of lattice strain $Q(hkl)$ to be:

$$t = 6G < Q(hkl) > \tag{4.4}$$

where $G$ is now the aggregate shear modulus, lattice strain $Q(hkl)$ is averaged from each lattice plane, and $t$ is the differential stress. Since the Reuss approximation is neglected and the shear modulus from lattice strain is ignored, this shear strength from the Voigt approximation is considered a lower bound to the actual shear strength [32,33].

This method is often useful when elastic constants or compliances are not known for a given sample material.

# CHAPTER 5

# GROUP IV-VIII TRANSITION METALS

## 5.1. Introduction

Group IV-VIII transition metals have been very important technological and industrial assets. For instance, titanium is one of the most heavily used metals due to its high strength and resistance to thermal and corrosive environments [34]. Heavy metals with high density such as *W*, *Re*, and *Os* have some of the highest incompressibility and strength of any metal on the periodic table (*Os* is the most incompressible naturally occurring metal), making them exceptional for industrial applications requiring high strength. The Group IV transition metals show electron transfer from s-band to d-band under compression due to relative increase in energy of s-electrons compared to the d-electrons at high pressures [35]. This increase in the d-character of conduction electrons results in high compressibility and phase changes on volumetric compression and has led to much attention for research studies. Moving left to right across the transition metals to Group V and down to the 5-d band, we see higher incompressibility and phase stability as these elements (*Ta*, *W*, *Re*, and *Os* particularly) have high electron densities while exhibiting less $s \rightarrow d$ electron transfer. These intriguing effects of transition metal phase stability have yet to be fully understood and here in this study, many of these metals are studied for the first time to multi-megabar pressures for understanding of phase stability, volumetric compression, and strength.

## 5.2. Tantalum and Rhenium

Tantalum (*Ta*) is a Group V element with outer electrons in the 5-d band, suggesting it is a stable material under high pressure applications. For example, *Ta* is used as a flyer plate for high speed (several km/s) impact of sample targets in shock compression experiments and has many applications in making alloys and electronics due to its strength and high melting point. *Ta* and its alloys are used in hypersonic engines, industrial cutting tools, and even for valve and pipe linings because of its chemical inertness [36]. These applications make *Ta* technologically relevant and is therefore important to determine the deformation and mechanical properties of *Ta* under extreme conditions. The stability of *Ta* under pressure also makes it a viable candidate for pressure calibration and equation of state formation within a DAC. The generation of near-terapascal (TPa, 1 TPa = 1000 GPa) static pressures in DAC devices has necessitated a search for reliable x-ray pressure standards and research on cross-comparison of pressure standards for studies of materials under extreme conditions. *Re* is used extensively as a gasket material in high pressure diamond cell experiments and serves as an internal x-ray pressure standard. Additionally, discrepancies in the *Re* equation of state [37,38] have been exposed to extreme pressures and a new equation of state (EOS) for *Re* has been proposed for use in the multi-megabar regime [38]. Studying *Ta* to high pressure in combination with *Re* allows for a cross comparison of x-ray pressure standards and to determine mechanical properties of *Ta* to high pressure. This study into *Ta* metal seeks to understand the mechanical deformation of *Ta* to multi-megabar pressures while investigating its potential role as a new high-pressure standard.

## 5.3. Osmium

The most incompressible transition metal *Os* has received extensive attention due to its high bulk modulus (incompressible nature), high shear modulus (resistance to deformation), and structural anomalies that have manifested themselves as anisotropic compression and have been attributed to changes in electronic structure under compression [39-43]. As mentioned previously, $s \rightarrow d$ electron transfer slows down for 5-d transition metals resulting in high stability. This makes the claims of changes in electronic structure (and discrepancies between each claim) very intriguing and worthwhile as *Os* offers many industrial and high strength applications. Some have claimed anomalies in c/a ratio at the pressure locations of 25 GPa [44] and 150 GPa [45] while others have noted a smooth monotonic increase in c/a [46]. The technical difficulty within high pressure experiments remains in achieving hydrostatic compression conditions, and particularly in the measurement of axial (*c*/*a*) comparisons of the results obtained under non-hydrostatic compression. In addition, experimentally, resistance to plastic deformation of *Os* under high pressure and a direct measurement of shear strength under high pressures is highly desirable. In this dissertation, I will show high-pressure studies into *Os* metal using XRD techniques to simultaneously probe for the first time hydrostatic and shear strength measurements at ultra-high pressures. This study has clarified the long-standing issue of anomalies present in the *Os* axial ratio under high pressures.

# CHAPTER 6

# TRANSITION METAL BORIDES

## 6.1. Introduction

Borides are formed in compounds where a less electronegative element is combined with the light covalent atom boron. Borides, specifically transition metal borides (TMBs), will often form compounds of profound physical toughness and high melting points that are useful for applications into turbines, engines, and industrial cutting and abrasive tools. Some of these TMBs, such as $MgB_2$, have shown superconducting properties [50] while others such as $OsB_2$ have shown incompressibility rivaling that of diamond [51]. The high incompressibility of the 5d TMB family also shows an indication of high hardness as well since a material of superior hardness will have a high bulk modulus and a high shear modulus to resist deformation. This can in part be attributed to high electron concentrations in 4d and 5d transition metals. The Coulomb repulsion from electron-electron interaction gives the material high resistance to compression while increasing boron concentrations have been shown to increase hardness in TMBs. It has been shown that the 5d TMBs ($ReB_2$, $OsB_2$) have higher bulk moduli than the 4d TMBs because of these phenomena [52].

The formation of TMBs is also somewhat of an easier process than other super hard materials, such as cubic boron nitride, that requires extreme conditions (high pressure–high temperature) to make. TMBs can be formed from arc melting that only

requires high temperature without the effect of pressure. The metallic nature of the TMB also allows for ease of machining as electrical discharge machining can easily shape a bulk sample. In contrast, other hard materials like diamond are difficult and costly to process. These alluring mechanical properties have brought attention to the field of TMBs as private companies now offer hypersonic flight to space, jet propulsion, plasma facing reactor components, and industrial tools.

## 6.2. Intriguing Properties of $ReB_2$

The rigid covalent *B-B* bonding and fascinating mechanical strength of TMBs have turned researchers to the attention of $ReB_2$ [53-55]. $ReB_2$ crystallizes in a hexagonal lattice where one will see boron layers form a puckered structure. As mentioned above, 5d TMBs have very desirable physical properties as $ReB_2$ has shown a high average hardness of 30-60 GPa [54-56] and bulk modulus 334-360 GPa [54,55] that is $3/4^{ths}$ of that of diamond (442 GPa). The single-phase stability of $ReB_2$ has solidified its applicability for environments of extreme conditions requiring high-temperature stability and resistance to plastic deformation. Though $ReB_2$ has been well studied in synthesis and mechanical properties, there remained no high-pressure equation of state to multi-megabar pressures nor high pressure shear strength measures until this study [9,12]. Many materials with super-hardness (hardness > 40 GPa), such as diamond, are prone to oxidation in high temperature environments. $ReB_2$ shows promise as an alternative to diamond for mechanical uses due the compound's stability up to 2000 K and the ease of machining.

Interestingly, $ReB_2$ shows anisotropic behavior between the *a* and *c* lattice parameters with increasing pressure. The *c*-lattice displays the highest resistance to compression with increasing anisotropy. However, previous results into this phenomenon have been done under non-hydrostatic (NHS) or quasi-hydrostatic pressure conditions. Because of the effect differential stress and NHS environments have on volumetric compression (Chapter 4 of this dissertation), it calls into question how the pressure induced lattice phenomena will change regarding pressure environments. This incites the interest of this dissertation to study $ReB_2$ to ultra-high pressure in non-hydrostatic environments and comparing results found from high pressure experiments using R-XRD and lattice strain theory to deduce hydrostatic values and shear strength.

## 6.3. Rationale for Studying $Os_2B_3$

Continuing with the high electron concentration and high strength of 5d transition metal borides, $Os_2B_3$ has received little attention despite its hexagonal counterpart $ReB_2$ and the orthorhombic $OsB_2$ being well studied. This indeed is quite shocking, as preliminary studies have shown $Os_2B_3$ to have a bulk modulus of 395 GPa that is higher than the previously mentioned TMBs. Only recent studies with neutron diffraction have revealed the atomic distances of the *B* and *Os* atoms within the crystal structure [57]. The role high temperature has on the volume of $Os_2B_3$ with simultaneous pressure conditions has not been investigated, leaving the availability for first-time studies on $Os_2B_3$. Similar anisotropic behavior between the *a* and *c* lattice parameter is seen in $Os_2B_3$ as to that documented in $ReB_2$ suggesting similar compression mechanisms of electron densities distributed more so along the *c*-axis than the *a*. These remained undetermined until this

study provided simultaneous P-V-T relationships to 1300 K and 5.4 GPa with additional P-V relationship in isothermal conditions to 358 GPa using novel T-DAC technology. These first-time studies of $Os_2B_3$ to extreme environments above 1300K and 350 GPa support the application for volatile environments as single phase stability under high pressure and temperature solidify its place in ultra-incompressible materials and high strength materials.

# CHAPTER 7

# DESCRIPTION OF EXPERIMENTS

## 7.1. Synchrotron X-ray Diffraction

### *7.1.1. Introduction.*

Synchrotron X-ray Diffraction has been a staple of materials science, as storage rings and other specialized particle accelerators can accelerate electrons to extremely high energies and create x-rays from collisions with heavy metal targets. High x-ray energies, known as hard x-rays, can be as high as 120 keV allowing for an extraordinarily broad range of material x-ray science. High energy x-rays (and correspondingly, low wavelengths) are essential for high pressure study of materials, as the bond distances between atoms are of a comparable distance. This is extremely beneficial for high pressure research, as the bond distances are shortened by the exerted force of the DAC and can be probed with hard x-rays.

Currently, there are efforts to decrease the achievable range of lateral and horizontal x-ray beam width to the sub-micron level and increase brightness by a factor of over 500 from current capabilities at the Advanced Photon Source (APS) at Argonne National Laboratory [58]. The large synchrotron source at APS comprises 34 sectors with multiple beam lines consisting of many research techniques such as x-ray scattering, spectroscopy, and imaging. In particular, all the XRD studies done in this dissertation were conducted at the High Pressure Collaborative Access Team (HPCAT) at Sector 16

of APS. HPCAT offers many HP XRD techniques, including a general purpose XRD table, radiography, RXRD, and HPHT studies. The following sections detail the XRD data collection (7.1.2–7.1.3), RXRD configuration at HPCAT (7.2–7.2.3), and methods of HP and HPHT studies for the listed transition metals and transition metal borides.

### *7.1.2. Overview of X-ray Diffraction at HPCAT*

Beamline 16-IDB at HPCAT offers a 1 μm (vertical) × 2 μm (horizontal) (FWHM) x-ray beam allowing for sample sizes < 10 μm. The small sample and beam size is ideal for HP DAC compression and is utilized for studies into tantalum, osmium, $ReB_2$, and $Os_2B_3$ equations of state. X-ray beam energy and wavelengths used are on the order of λ = 0.40 Å and 30 keV respectively, though, 16-IDB offers beam energies between 18-50 keV [59]. Beamline 16-BMD also offers micro-diffraction techniques for DAC compression using Kirkpatrick-Baez focusing mirrors to deliver a beam of 3 μm (vertical) × 4 μm (horizontal) (FWHM) at 30 keV [60]. The micro XRD set up at 16-BMD is also compatible with RXRD as opposed to only compression axis diffraction techniques. A double multilayer monochromator is used to collimate the x-ray beam, producing a 1.3% bandwidth pink beam that can deliver 50 times more x-ray flux for better XRD statistics [61]. This is essential as the x-ray beam path must pass through the gasket material containing the sample and is described more in section 7.2. Beamline 16-BMB is the only beamline in this study to not use DAC compression but offers a large volume press known as a Paris-Edinburgh (PE) press. This is needed as beamline 16-BMB hosts the capability to deliver simultaneous HPHT applications to ~7 GPa and to 2000 ℃, whereas diamond will burn in air between 700-800 ℃. 16-BMB does not use a

monochromatic x-ray beam, but rather uses a white beam spectrum for energy dispersive x-ray diffraction (EDXD) ranging across the energies 10-120 keV. EDXD can probe or x-ray fluorescence along with nuclear peaks, allowing for accurate determination of constituent atoms and d-spacings of samples with pressure and temperature [59].

### *7.1.3. Overview of Data Collection*

XRD data is collected on a flat detector plate and essentially similar between the three beamlines listed. However, the type of detector used differs. 16-IDB uses two easily interchangeable detectors, a MARCCD and a MAR345 detector with sample to detector distances ranging between 250–1100mm. the '345' indicates the diameter of the image plate and can give resolution up to 3450 pixels with a minimum pixel size of 100 microns. Optimizing the detector distance enhances the spatial resolution of collected XRD peaks and is essential for the data refinement process. CCD detectors typically will reduce the readout time of collected data but are smaller in diameter. For the studies conducted on 16 IDB, the MAR345 detector was chosen. 16-BMD also offers the MAR345 detector along with a Pilatus 1M CCD detector that is based on hybrid photon counting technology where each cell (or pixel) is a detector itself. The theory behind Pilatus detectors is beyond the scope of this dissertation, but they are a common standard at synchrotron sources. Both detectors have been used for R-XRD experiments, the MAR345 for $ReB_2$ studies and Pilatus 1M for *Os* sample. Choice of detector use is a matter of preference, and both were used to output 2300 pixel × 2300-pixel XRD images for R-XRD data refinement. Finally, a solid-state detector using a *Ge* medium was used on beamline 16 BMB for HPHT experiments on $Os_2B_3$ sample. The data refinement

process for angular XRD from data collected at beamlines 16 IDB and BMD are similar in that traditional Rietveld method is used. For EDXD collected from beamline 16-BMB, gaussian fitting is used to determine XRD peak positions and d-spacings. A detailed description of the refinement procedure of data collected for HP and HPHT experiments on transition metals (*Ta*, *Os*, *Re*) and TMB ($ReB_2$, $Os_2B_3$) can be found in Ch. 8 of this dissertation.

## 7.2. Radial X-ray Diffraction

### *7.2.1. Geometric Configuration*

Radial x-ray diffraction (R-XRD) combined with DAC compression is a robust experimental method that can utilize the LST detailed in Chapter 4 to determine estimated hydrostatic compression values and strength. As can be seen in Figure (5), the configuration of the DAC relative to the incident x-ray beam is rotated 90 degrees such that the incident x-ray beam is perpendicular to the axis of compression. Figure (5) is a schematic diagram of the R-XRD setup at beamline 16-BMD at the Advanced Photon Source, Argonne National Laboratory. X-rays produced from the synchrotron source are focused through a set of Kirkpatrick-Baez mirrors and into a collimating pinhole to deliver the desired x-ray beam size (Section 7.1.2). The DAC sits atop a stage with *xyz*-directional motors to align the beam onto the sample. The entire DAC assembly sits on a rotating stage for additional sample alignment. A more detailed diagram of the setup at 16-BMD can be found in reference [60].

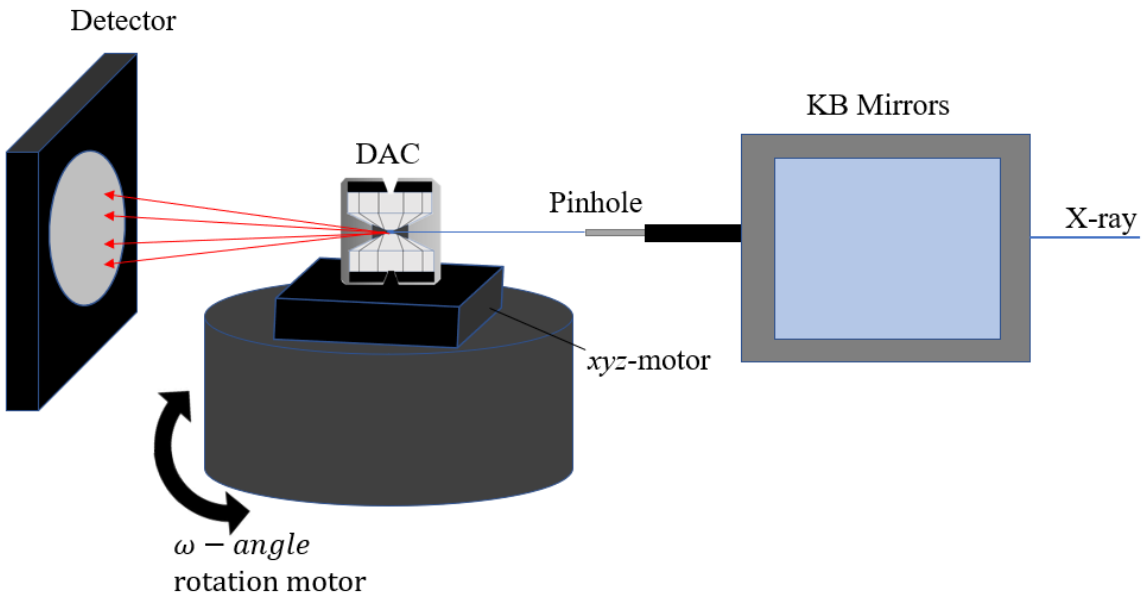


Figure (5). Schematic diagram of the DAC assembly at beamline 16 BMD, HPCAT, Argonne National Laboratories for performing radial x-ray diffraction studies.

The geometry of the DAC position relative to the x-ray beam is essential for the application of LST. As shown and discussed in Figure 4 and Chapter 4, a non-hydrostatic (NHS) environment in a DAC will induce a differential stress in the sample with the maximum stress along the axis of compression. Looking at the inter-planar d-spacing in Figure 6, it is possible to determine some variables needed for equation 4.2 in order to calculate hydrostatic components. The angle $\psi$, which is the angle between the cell compression axis and the diffracting plane normal ($v$), and the angle of diffraction $\theta$ can be determined by refinement of R-XRD patterns (Chapter 8, Section 8.4). Particularly, the angle $\psi = cos\theta cos\delta$ where $\delta$ is just the azimuthal angle around an XRD pattern that can be seen in Figure 7. The angle $\delta = 0$ coordinate position can be arbitrarily chosen but is typically either along the axis where d-spacing is a maximum or minimum. As NHS builds within the sample under compression, the d-spacings are strained unevenly because of the differential stress. When one observes the R-XRD images, there will be a

distortion in $2\theta$ that exhibits itself as a 'wavy' feature when the image is integrated with respect to the azimuthal angle and $2\theta$ (Figure 8).

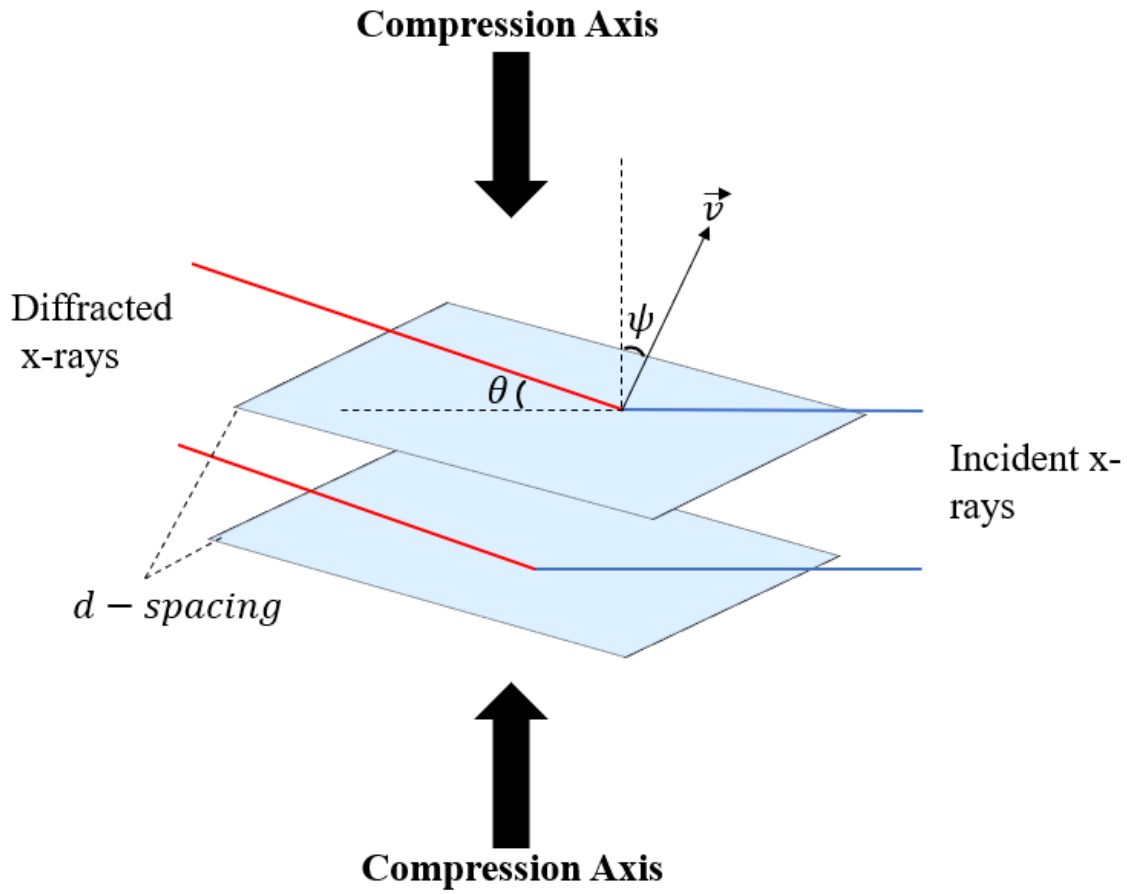


Figure (6). Diagram of x-ray diffraction off sample interplanar d-spacings in a radial geometry. The angle $\psi$ is the angle between the DAC compression axis and the diffracting plane normal $v$. The angle $\theta$ is the angle of diffraction.

This can be seen in Figure 8 (a) where a sample R-XRD image consisting of $ReB_2$ is integrated and plotted with azimuthal and $2\theta$ coordinates. It is noted that the diffraction lines corresponding to each *hkl* are very linear at low pressure. When moving to higher pressure (higher strain) in 8(b), the integrated *hkl* lines are no longer linear but present the wavy feature described above. The maximum deviation of the diffraction line corresponds to a shorter d-spacing (maximum stress) and the minimum to a longer d-

spacing (minimum stress) and here are centered on the angles $\delta = 0, 180°$ ... and $\delta = 90, 270°$ ... respectively. Knowing the relationship between azimuthal angle $\delta$, angle of diffraction $\theta$, and measured d-spacing $d_m(hkl)$ with equation 4.2, LST can be applied to determine strain $Q(hkl)$ and hydrostatic d-spacing, $d_p(hkl)$.

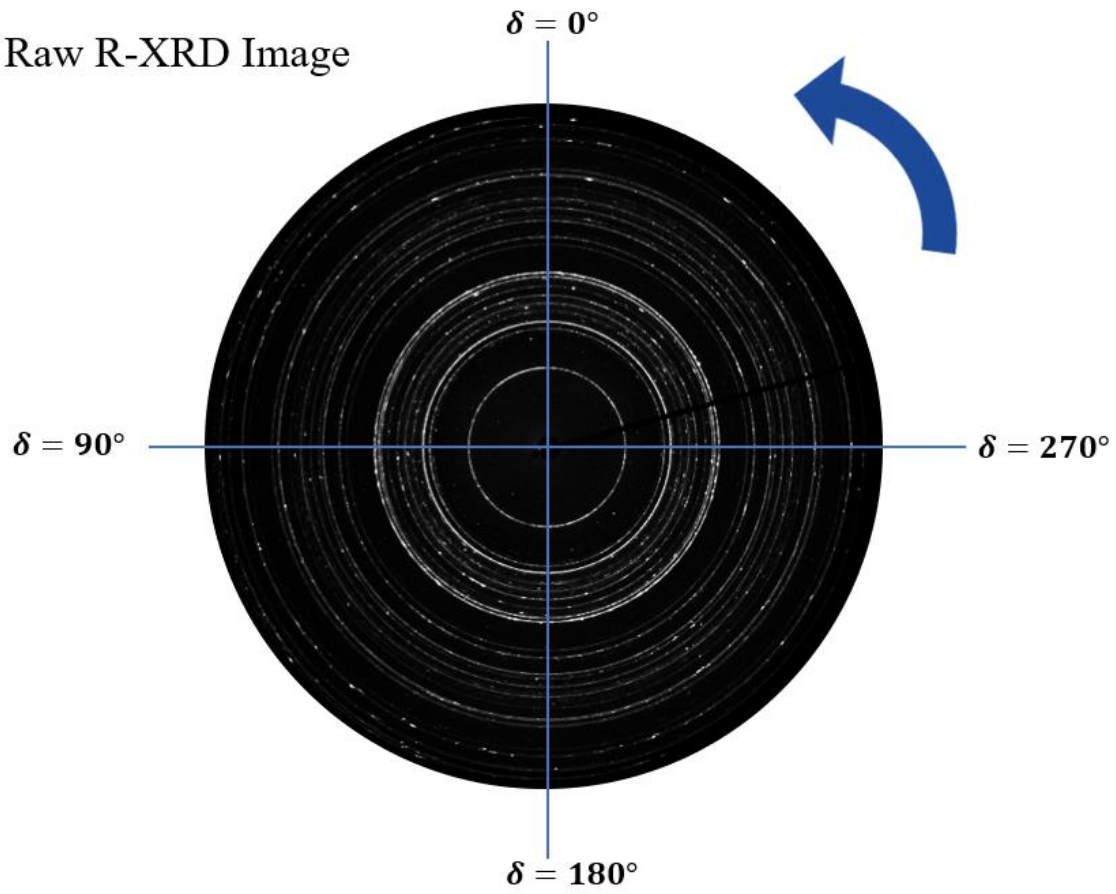


Figure 7. Raw x-ray diffraction image with corresponding azimuthal ($\delta$) angle labels.

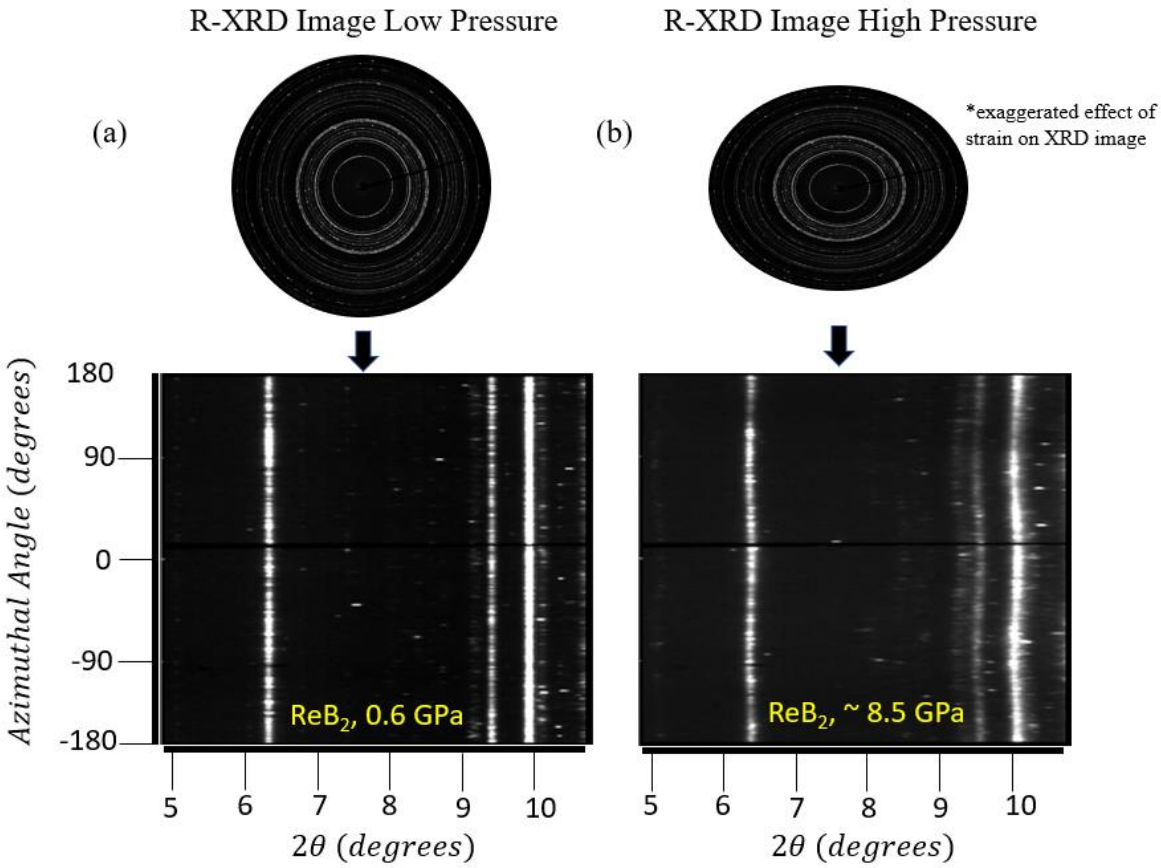


Figure 8. Example of the effects non-hydrostatic pressure has on lattice strain for $ReB_2$. (a) Low pressure R-XRD image and integrated image below at 0.6 GPa. Straight diffraction lines are noted. (b) R-XRD image of $ReB_2$ at 8.5 GPa and corresponding integrated diffraction lines. Non-hydrostatic stress has induced higher lattice strain resulting in 'wavy' diffraction lines.

### *7.2.2. Application of Lattice Strain Theory*

The magnitude of the uniaxial stress component of the DAC is essential for inducing an NHS environment in the sample. As such, no pressure transmitting medium is used to ensure strain is maximized in a sample material. By re-writing equation 4.2 into the following form:

$$d_m(hkl) = d_p(hkl) + dp(hkl)Q(hkl)(1 - 3\cos^2\psi) \tag{7.1}$$

we can see that it is in a linear $y = mx + b$ format. This is advantageous as plotting the measured d-spacing $d_m(hkl)$ taken from collected R-XRD images versus $(1 - 3\cos^2\psi)$ will give a slope of $dp(hkl)Q(hkl)$. This information allows for direct calculation of lattice strain as a function of each *hkl* value once $dp(hkl)$ is known. The hydrostatic components of d-spacing can be easily found from equation 7.1 from observing the cosine relationship that $1 - 3\cos^2(57.3°) = 0$ and thus relating $d_m(hkl) = d_p(hkl)$ at this angle. In a $d_m(hkl)$ vs $(1 - 3\cos^2\psi)$ plot, this will be when the d-spacing crosses the intercept $(1 - 3\cos^2\psi) = 0$. The dependence of the angle $\psi$ on measured d-spacings is general and valid for all crystal systems [32].

The calculation of the differential stress *t* in a sample requires knowledge of the elastic moduli of the specimen as discussed in Chapter 4 Section 4.4. For the samples in this study of transition metals and transition metal borides, elastic moduli were determined from density functional theory (DFT) to calculate the aggregate shear modulus *G* for equation 4.4. As just shown, the experimental value for lattice strain $Q(hkl)$ can be determined from the $d_m(hkl)$ vs $(1 - 3\cos^2\psi)$ plots and used to calculate the differential stress *t*. It is then simple to use equation 4.3 and the relation:

$$< Q(hkl) > \sim \frac{t}{6G}, \quad t = 2\tau$$

To find the sample maximum strength where $\tau$ is the shear strength.

### *7.2.3. Limitations*

R-XRD requires the use of a low-Z gasket materials (typically *Be*) to allow x-ray propagation onto the sample and minimize gasket interference. Low-Z materials are often very brittle and will limit the achievable pressure to ~ 120 GPa as thinning of the

mechanically weak gasket will cause failure of the DAC. Though the low-Z material is essentially invisible to x-rays, propagating through an entire gasket ensures there will be some gasket impurities in XRD images. These peaks can align with sample XRD peaks, causing difficulty or inability to refine XRD for accurate determination of d-spacings and lattice parameters. Samples and pressure markers are chosen to minimize peak overlaps with *Be* gasket.

The equations derived in reference [32] and employed in this dissertation are under the assumption that sample crystallites are randomly oriented. Naturally, this limits the application of LST and R-XRD to polycrystalline systems. Increasing pressure on randomly oriented samples can cause texturing, or preferred orientations, where XRD peak intensities will vary or vanish as crystalline grains align with incident x-rays. Given that many determinations of d-spacing and strain are *hkl* dependent in LST, the effect of extreme texturing on samples is still under investigation as plastic flow, grain sizes, and degree of random orientation are all subject to affect the XRD refinement. One method to avoid this issue would be to assume the *hkl* independent calculations using the Voigt approximation in equation 4.3. This will provide a lower bound to the shear strength but is still very useful for samples with extreme texturing.

### 7.3. Creation of Toroidal DAC for High Pressure Generation

The toroidal anvils in the studies of *Ta*, *Re*, *Os*, and $Os_2B_3$ were created by focused ion-beam (FIB) machining of single crystal diamond anvils by utilizing the TESCAN LYRA3 FIB-SEM at the University of Alabama-Tuscaloosa's Central Analytical Facility. The milling of the diamond surfaces was done using a *Ga*+-ion beam

held at 5 nA and 30 keV delivering a beam size of 50 nm for each toroidal anvil made. An image of the first design can be seen in Figure 9. The first toroidal design (now designated TD- 1) comprised a planar disk with a central flat culet of 16 microns that descended 3-microns in depth to an intermediate region of 40 microns before flattening to an outer 60-micron diameter. This was machined away from the original 25 microns culet that is outlined by the dashed line in Figure 9. Figure 10 details the second design (TD-2) used in this dissertation that consisted of a toroidal groove machined to a depth of 5 microns around the culet with an inner diameter of 20 microns and outer diameter of 35 microns. Again, the dashed line in Figure 10 indicates the original diamond shape and culet of 25 microns before the FIB machining process. For each of these designs, a replica was made for the opposing diamond anvil.

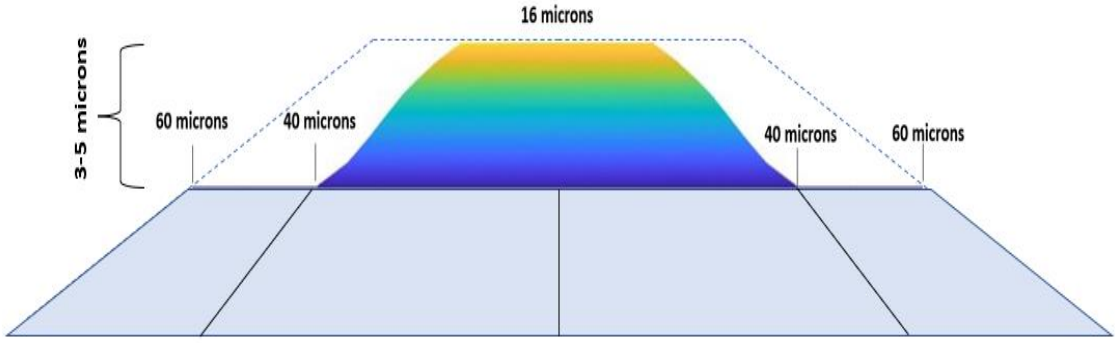


Figure 9. Schematic diagram of the planar toroidal disk design with labeled distances (height not to scale). The dashed line indicates the original diamond shape (25-micron culet) before FIB machining.

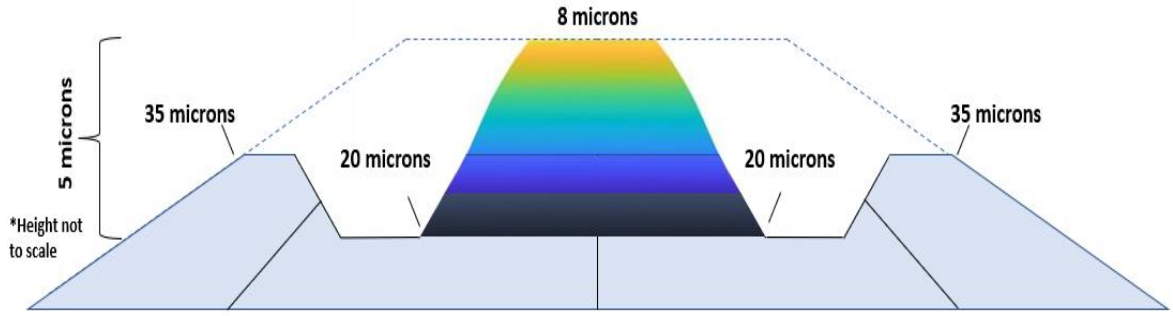


Figure 10. Schematic diagram of the toroidal groove design with labeled diameters. The dashed line indicates the original diamond shape (25-micron culet) before FIB machining.

One particular challenge of FIB machining diamond arises due to the density and hardness of diamond. This creates a very slow milling process from the *Ga+* ion beam which typically resulted in one diamond anvil being machined within a 4–6-hour window. To expedite the milling process, a bitmap image was created using GIMP software [62] that can be uploaded to the Tescan LYRA3 to machine a desired shape with certain specifications. Figure 11 shows the bitmap image used for both designs with labels inlaid to clarify dimensions. The inner black region was centered over the diamond culet and a pixel–to–micron ratio built within the FIB machine allows for accurate control of the outer diameter size. The black region corresponds to areas unaffected by the *Ga+* beam, while areas of increasing white intensity correspond to higher beam energy and thus greater depth of milling. The method of inserting a bitmap image assured accurate dimensions of FIB machining of the diamond without having to manually adjust FIB parameters.

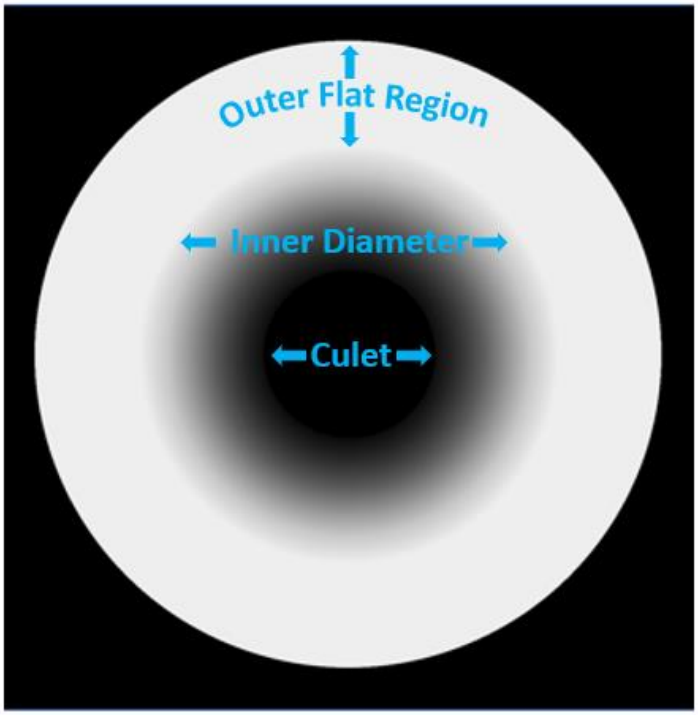


Figure 11. Bitmap image of the toroidal design for Focused Ion Beam milling. The regions for the culet, inner diameter, and outer diameter are labeled.

Another challenge associated with FIB machining displays itself with a sample materials propensity for conducting electrical charge. Diamond, being a stout semi-conductor, will not disperse the charge gathered from the incident *Ga+* beam easily. The clarity and resolution of the electron microscope image within the FIB machine depends on the interactions of electrons with the specimen. The most common imaging mode within an electron microscope is the detection of secondary electrons that are inelastically scattered off the surface and collected onto a detector. Materials, such as diamond, that are not good conductors and are very dense will interfere with this process and cause a blurring or 'drifting' of detector images resulting in improper location of FIB machining. To resolve this issue of drifting, diamond anvils were coated with a thin *W* metal to increase the conductivity. This was done by DC metal sputter deposition and micro-

lithography at the University of Alabama–Birmingham's Center for Nanoscale Materials and Biointegration. A diagram of the lithography and deposition process is detailed in Figure 12. In Figure 12 (a), the diamond is coated with a thin light reactive polymer (in red) and then etched away using light in 12 (b) for the area that *W* will be deposited in. Figure 12 (c) shows the deposited *W* film (in gray) via sputter metal deposition with the remaining polymer removed. The final product is shown in the Scanning Electron Microscope (SEM) image in Figure 12 (d) where the diamond is completely coated in tungsten film with the area around the culet exposed for FIB machining.

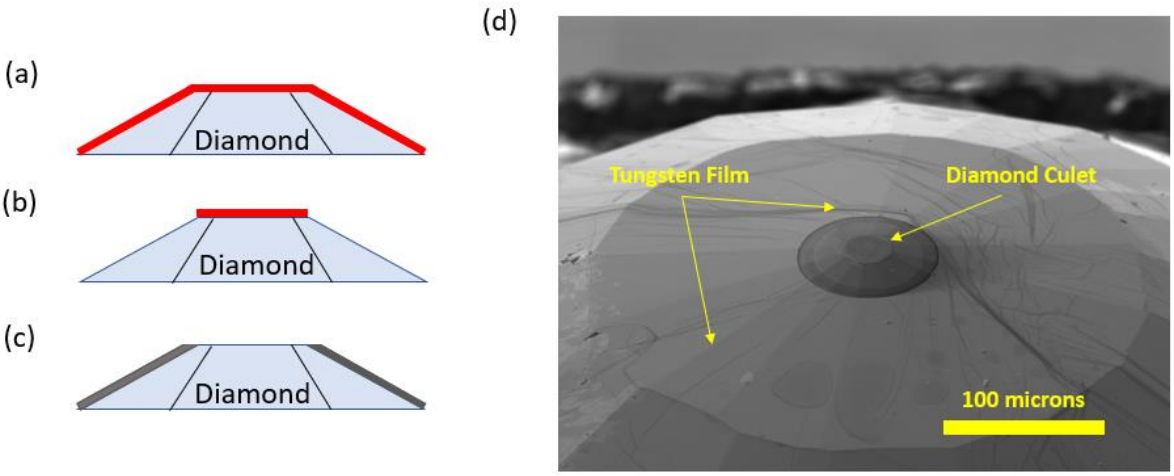


Figure 12. Diagram of diamond anvil during the microlithography and sputter deposition process. (a) The diamond anvil is first coated with a light reactive polymer (in red). (b) Light is used to etch away the polymer in regions where *W* is desired to be deposited. (c) Tungsten is deposited (in gray) and the remaining polymer is removed leaving the diamond culet exposed for FIB machining. (d) SEM image of anvil with tungsten coat.

## 7.4. Samples and Procedures

### *7.4.1. Tantalum – Rhenium High Pressure Studies*

The ultra-high pressure non-hydrostatic experiments in this study used two pairs of toroidal diamond anvils: one using a pair of TD-1 and another using a pair of TD-2.

Two matching anvils were made for each design and employed in an opposing anvil configuration for non-hydrostatic compression and can be seen in Figure 13 (a) and (b). In Figure 13 (a), a diamond anvil featuring the planar design of TD-1 is shown in an SEM image. Beside it in Figure 13 (b) is the created toroidal groove design of TD-2. For both anvils, matching pairs were made with similar dimensions and size with the TD-1 having a culet of 16 microns and TD-2 with the smaller 8 microns.

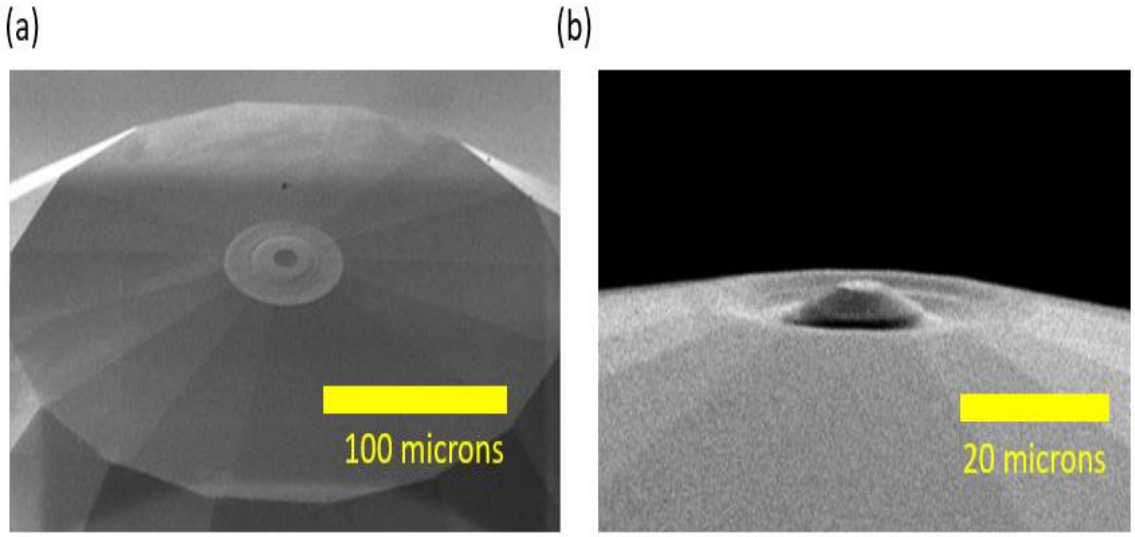


Figure 13. (a) SEM image of implemented TD-1 design onto a diamond anvil for compression of Ta and Re samples. (b) SEM image of TD-2 on a diamond anvil for Ta-Re sample compression. For both designs, matching pairs of toroidal diamond anvils were made. This design reached a pressure of 308 GPa.

The samples used were procured from Alfa Aesar in a polycrystalline foil with purity 99.95% for *Ta* and gasket material *Re* of 99.97% purity. The gasket and sample thicknesses were 25 microns each and were overlaid between the anvils. For high pressure XRD studies and creation of high-pressure calibration with *Ta* and *Re*, Angle-dispersive XRD experiments were conducted at the High Pressure Collaborative Access

Team (HPCAT) beamline 16-ID-B of the Advanced Photon Source at Argonne National Laboratory. The x-ray beam consisted of size 1 μm (vertical) ×2 μm (horizontal) (FWHM) with beam energy 30keV and wavelength λ = 0.4066 Å. The XRD patterns were collected on a Pilatus 1M detector maintaining a sample-to-detector distance of 209.73 mm calibrated using $CeO_2$ XRD pattern. The DACs were compressed using a gas membrane system pumped by *He* gas with pressure steps of 5-10 psi equating to ~ 0.5 - 2 GPa increases.

This study into Ta was also conducted in unison with Los Alamos National Laboratory (LANL) Shock and Detonation Physics group. They provided quasi-hydrostatic compression values for cross comparison using a neon pressure medium and a pair of 200-micron flat diamond anvils. *Ta* sample was of ultra-high purity using *Au* powder as a pressure standard [63]. HPCAT beamline 16-BM-D was used for the Angle-dispersive X-ray diffraction experiments holding a beam wavelength of λ = 0.4246 Å. For their studies, they equipped a Mar345 image plate for data collection with an x-ray beam size of 4 μm (vertical) ×5 μm (horizontal) (FWHM) maintaining a sample-to-detector distance of 465.48 mm. The cross comparison of quasi hydrostatic values was also done with equations of state of *Re* determined from the Dubrovinksy group [64] and Anzellini et al. [65] to ascertain the validity of high pressure generation and accuracy of *Ta* equation of state.

For integration of XRD data from non-hydrostatic and quasi-hydrostatic studies, the software Dioptas [66] was used and followed by structural refinement from GSAS II software [67]. Two equations of state were used to relate the pressure and volumetric changes: the Rydberg-Vinet for quasi-hydrostatic studies [16,68] and the $4^{th}$ Order Birch–

Murnaghan proposed by Dubrovinksy et al. for *Re* in the non-hydrostatic study [64]. For further cross comparison, shock compression studies of *Ta* by R. Mcqueen et al. [69] is included. The following Table details equation of state parameters used for pressure calibration of each study:

Table 1

*Experimental Details for Ta High Pressure Studies*

| Experiment | EoS | Pressure Marker | Bulk Moduli | Pressure Range |
|---|---|---|---|---|
| Non-Hydro 1 | 4th Order BM | Re | $K_0$ = 352.6 GPa $K_0$'= 4.56 [70] | 0-144 GPa |
| Non-Hydro 2 | 4th Order BM | *Re* | $K_0$ = 342 GPa, $K_0$'=6.15 [69] | 0-600 GPa |
| Quasi-Hydro | Rydberg-Vinet | *Au* | $K_0$ = 167 GPa $K_0$'=5.9 [68] | 0-200 GPa |
| Shock [74] | Shock derived isotherm | N/A | N/A | 0-230 GPa |

The ambient pressure lattice parameters for *Ta* were measured independently at the University of Alabama at Birmingham by x-ray diffraction for *Ta* and determined to be a = 3.302 ± 0.003 Å ($V_0$ (*Ta*) = 18.001 Å$^3$/atom).

### *7.4.2. Osmium High Pressure and R-XRD Studies*

To study the intriguing *c*/*a* ratio anomalies as well as provide first time multi-megabar hydrostatic and strength studies into *Os*, extensive experiments were done utilizing axial XRD at HPCAT Beamlines 16 ID-B and R-XRD at 16 BM-D. For high pressure studies at 16 ID-B, two similar toroidal anvils were fabricated in the planar design and dimensions of TD-1 from 30-micron beveled diamonds. To accommodate the small culet size of 16 microns, the x-ray beam was focused to 1 μm x 2 μm using Kirkpatrick-Baez mirrors and wavelength of 0.4066 Å (30.5 keV). The high-pressure axial data was collected onto the Pilatus 1M detector with resolution of 2300 pixels x 2300 pixels. Osmium samples were purchased form Alfa Aesar with 99.95% purity in polycrystalline powder form and was mixed with platinum for pressure calibration (Alpha Aesar 99.97% purity) in a 1:3 volumetric ratio. A gasket of hardened spring steel was indented from 230 microns to 30 microns thickness using the toroidal diamond anvils to create a fitted gasket over the diamonds for sample placement on the culet. A laser drilled hole of 8 microns was used to pack the sample mixture into for compression.

For the R-XRD experiment into *Os* at Beamline 16 BMD, a slightly larger beamsize of 3.4 μm (vertical) x 4.4 μm (horizontal) (FWHM) was used at a similar energy of 30 keV (0.4133 Å). To allow for radial x-ray propagation and diffraction through the to the

sample, a *Be* gasket was employed by indenting with a pair of standard flat culet 70-micron diamond anvils. Electrical discharge machining was used to drill a 25-micron sample hole into the *Be* gasket for sample placement. Recent upgrades in the focusing mirrors and monochromators at Beamline 16-BMD now allow for generation 'pink' x-ray beams that can provide 50 times more flux than previous setups [60]. Higher flux provided better sample statistics that are typically lost by attenuation of the x-ray beam through the gasket. Similar to the other detector distances used, $CeO_2$ diffraction pattern was employed to for a sample–detector distance of 286 mm. This study in R-XRD used the MAR345 Image Plate for XRD collection with the same pixel resolution as the axial compression experiment on 16 IDB. The collected R-XRD data was integrated into 72 segments of azimuthal angles $\delta = 5°$ and Rietveld refined for determination of hydrostatic lattice parameters using MAUD software [70]. Finally, both the axial and radial XRD used the same equation of state parameters of platinum ($K_0$ = 276.4 GPa, $K_0'$ = 5.12 [71]) in the 3$^{rd}$ Order Birch Murnaghan EoS for pressure determination.

### *7.4.3. $Os_2B_3$*

*7.4.3.1. Toroidal DAC Compression.* The transition metal boride $Os_2B_3$ was also studied with two separate experiments, albeit by a broader study into its mechanical properties by including thermo-mechanical responses to simultaneous high pressure–high temperature conditions. This was essential to the understanding of $Os_2B_3$ in extreme environments as $Os_2B_3$ exhibits high resistance to compression and is expected to have excellent resistance to thermal environments despite little to no HPHT work being conducted previously. The

first experiment conducted into $Os_2B_3$ for this dissertation studied the HP effects using axial XRD at beamline 16-BMD. Only one toroidal design (TD-1) was employed and a beam size comprising 3.7 μm (vertical) × 3.8 μm (horizontal) (FWHM) was used. The pressure environment within the DAC is considered non-hydrostatic as no pressure medium was used. $Os_2B_3$ sample was in a powder polycrystalline form that was ordered from American elements with a chemical purity 99.9% and was mixed with *Pt* powder (Alpha Aesar 99.97% purity) for pressure calibration using Yokoo et al. parameters ($K_0$ = 276.4 GPa, $K_0'$ = 5.12) [71]. The sample mixture was placed within a sample hole of 8 microns that was laser drilled into a *Re* gasket previously indented to 25 microns thick. The Pilatus 1M detector to sample distance was calibrated at 344.63 mm using the same $CeO_2$ XRD pattern previously mentioned, and data integration and refinement were done using the same methods as Section 7.4.1. Sample lattice parameters at ambient pressure were taken at the University of Alabama at Birmingham and were determined to be $a_0$ = 2.915 Å and $c_0$ = 12.92 Å.

*7.4.3.2. High Pressure – High Temperature Study of $Os_2B_3$.* For the first time, HPHT studies were conducted on $Os_2B_3$ using the large volume press, known as the Paris-Edinburgh Press (PE Press), at beamline 16-BMB, Advanced Photon Source, Argonne National Laboratories. The PE press does not utilize diamond anvils, but instead uses tungsten carbide (*WC*) anvils that withstand temperatures up to 2000 °C that can be delivered at the beamline. A schematic diagram of the PE press can be seen in Figure 14. The $Os_2B_3$ sample is of the same powder and purity as the previous axial XRD experiment, however, the sample dimensions within the PE press are on the order of

millimeters (1.0 mm (vertical) × 1.5 mm (horizontal)) instead of micrometers. Powder samples sit within a thermally insulating gasket made up of zirconia, boron epoxy, and boron nitride with an inner ring of *MgO* for simultaneous pressure–temperature calibration [72]. The cylindrical shape and large size of the sample helps provide a quasi-hydrostatic compression that is limited to ~7-9 GPa. The x-ray beam produced at beamline 16-BMB does not use monochromatic light but uses a white beam for EDXD ranges between 5-120 keV. This was used to probe nuclear XRD peaks for $Os_2B_3$ as well as provide radiographic imaging of the sample under compression. An example of the radiographic sample image before compression can be seen in Figure 15.

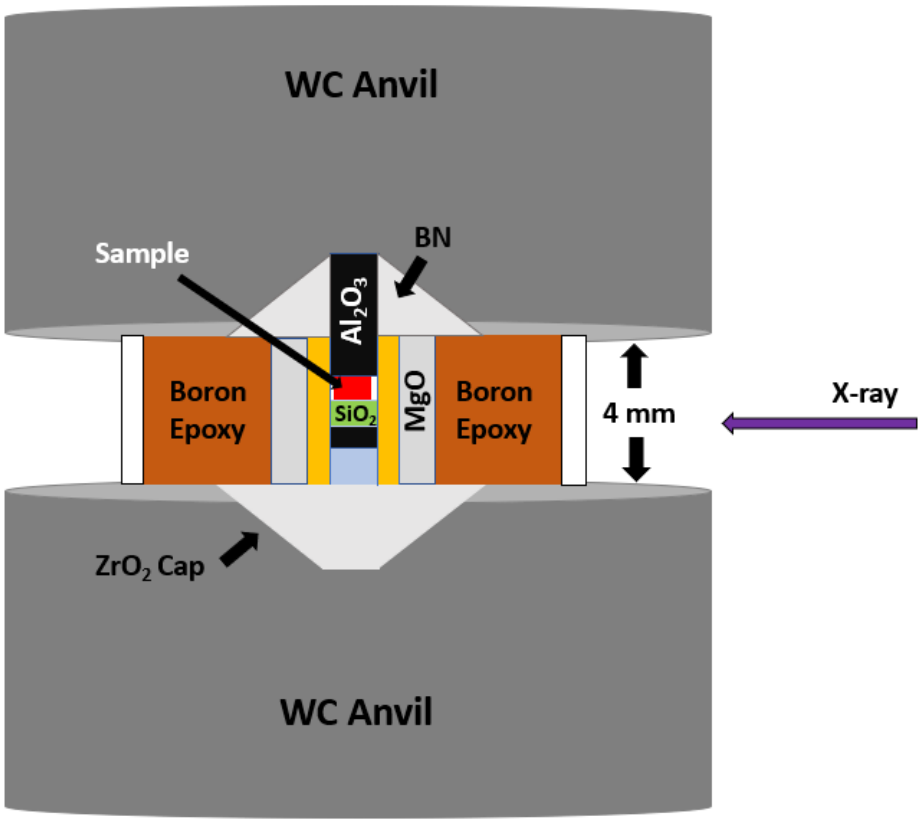


Figure 14. A schematic diagram of the Paris-Edinburgh Press at Beamline 16BM-B. Two *WC* anvils compress a sample within a thermally insulating gasket of boron epoxy, zirconia, and boron nitride. *MgO* is used as a pressure calibration for HPHT conditions.

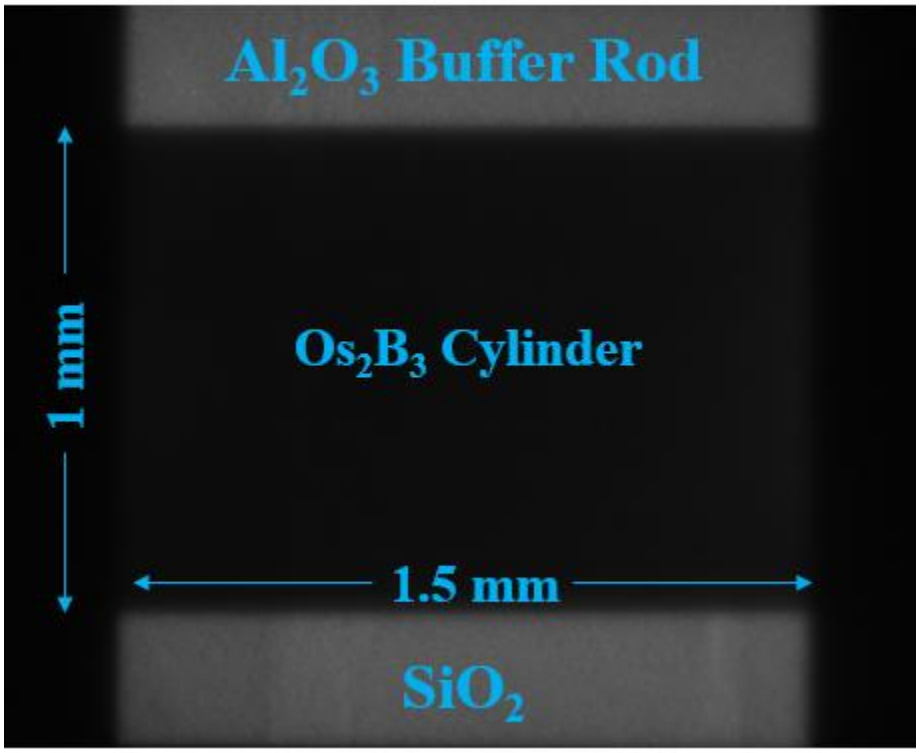


Figure 15. Radiographic image of $Os_2B_3$ sample within the PE press prior to compression.

Heating of the gasket and sample is accomplished by using a radial graphite heater that fits as a sleeve between the two anvils. More detailed diagrams of the setup at beamline 16-BMB can be found in reference [73]. The heating was done in steps of 298 K, 673 K, 873 K, 1073 K, and 1273 K. For each step, temperature was held constant, and pressure was increased in 400psi steps (~0.3 GPa correspondingly) until ~5 GPa was reached with EDXD images taken at each step. Pressure was then released to ambient, and temperature was increased to the next step. The Solid-State *Ge* detector for EDXD data collection was set at a 2θ angle of 15.0167 ± 0.0012 degrees that was calibrated using 50-micron gold wire. The collected EDXD data of Os2B3 *hkl* peaks was analyzed

by using gaussian fitting of energy peaks to convert peak centers to d-spacings and lattice parameters as a function of pressure and temperature.

### *7.4.4. $ReB_2$*

*7.4.4.1. High Pressure EoS Measurements.* The transition metal diboride $ReB_2$ shares similarities in crystal structure with $Os_2B_3$ as both are hexagonal of the $AlB_2$–type, however, mechanical, and thermal properties have been well studied (at low pressure) in comparison to $Os_2B_3$. Here in this study, a $ReB_2$ EoS > 200 GPa was sought and achieved for the first time to study anisotropy noted between the *a* and *c* lattice parameters [52–55]. This was done under non-hydrostatic (NHS) conditions and later compared with hydrostatic values from R-XRD. For the NHS compression, standard 30-micron culet diamond anvils with 8-degree bevel were used for compression to 241 GPa, and a 50-micron diamond anvil was used for lower pressure study to 105 GPa. The experimental setup and data refinement for axial XRD of $ReB_2$ used was identical to the setup for axial compression of $Os_2B_3$ previously discussed (Section 7.4.3.1). $ReB_2$ sample was also purchased from American Elements (purity 99.9% (metals basis)) in powder form and mixed with platinum powder in the same volumetric ratio as the $Os_2B_3$ experiment to high pressure. The ambient lattice parameters of $ReB_2$ were independently determined at the University of Alabama at Birmingham to be $a_0$ = 2.901 Å and $c_0$ = 7.482 Å and were calibrated versus pressure using the Yokoo et al. EoS for *Pt* [71].

*7.4.4.2. Radial XRD Double Compression of $ReB_2$.* All studies into $ReB_2$ have been, at best, in quasi-hydrostatic pressure environments that are limited < 30 GPa because of

crystallization of noble gases used for pressure mediums [54,74,75]. The effect of hydrostatic environments on $ReB_2$ is desirable, as it is unclear to what degree an NHS environment has on the anisotropic nature of $ReB_2$ lattice parameters with pressure. Is the anisotropy seen in $ReB_2$ similarly seen in hydrostatic values, and how does this affect calculations of bulk moduli and volume? There is also the interest in determining strength of $ReB_2$ to high pressure (>30 GPa) which has also not been done. In this study, R-XRD combined with DAC compression of 300-micron flat diamonds was used to determine an estimation of hydrostatic compression values from LST and shear strength of $ReB_2$ to 74 GPa for the first time to address these questions. The experimental setup at beamline 16 BMD for R-XRD is identical to the setup discussed in Section 7.4.2. Only the detector to sample distance varied at 346.16 mm. The same powder $ReB_2$ sample from American elements was used with the same platinum - $ReB_2$ ratio of 1:3.

Given the powder form of the sample, it is also of interest to study how shear strength and strain vary between the powder and an already compressed sample of $ReB_2$. Naturally, including *Pt* into the sample mixture also begs the question if the weaker specimen (*Pt*) will decrease the measured shear strength that is determined from LST. A second R-XRD experiment of powder $ReB_2$ compression to 30 GPa was conducted at beamline 16-BMD using 600-micron flat diamond anvils. After the maximum pressure, the sample was decompressed and then recompressed to 30 GPa. The sample was not added with *Pt* mixture to determine the effect platinum has on measured differential stress and compared with the previous R-XRD study of $ReB_2$ to 74 GPa.

# CHAPTER 8

# ANALYSIS OF DATA - METHODS

## 8.1. Introduction to Rietveld and Lebail Refinement

X-ray diffraction is the most common method of analysis for materials science and can be found generally all reviews and articles of material properties. This has led to many methods of XRD analysis that have become staples in the materials science community. The most popular method of XRD analysis is Rietveld refinement that was developed by Hugo Rietveld [76] that uses a least squares method to match a theoretical XRD profile to one which is measured. As such, a model of the crystal structure of the specimen to be refined is needed and cannot be created from the refinement itself. These are normally stored in CIF files on open databases for general and public use. The process of Rietveld refinement can be defined by the following algorithm:

1. Establish function for baseline of background x-rays
2. Find peak positions using Bragg's Law
3. Refine peak intensities for each *hkl*
4. Model peak shape and width using Gaussian/Lorentzian fits

The process of establishing a background function for background x-rays isolates the desired XRD pattern for refinement. Once done, peak positions are found typically in terms of $2\theta$ and energy, which can be related to the sample d-spacings. This allows for determination of unit cell parameters (*a*,*b*,*c*) and porosity. Information on the atomic

parameters (*x*,*y*,*z*) and preferred orientation (texturing) can be determined from refinement of peak intensities while the peak width and shape rises from properties into grain size, strain, and stress.

Similar to Rietveld refinement in terms of the algorithm, Lebail refinement [77] is another popular method for refining XRD data. As mentioned, a model of the crystallographic structure for a sample under ambient conditions is first needed for Rietveld refinement and is also true for Lebail. However, Lebail refinement does not require information into the structure factor of the sample, which is a mathematical description of how a material scatters radiation. Within Rietveld refinement, the structure factor F(hkl) is used to model sample intensities while in Lebail refinement intensity is arbitrarily chosen and then fitted using a summation of observed intensity ($y_i$(obs)) relative to the calculated ($y_i$(calc)):

$$I(obs) = \frac{\sum y_i(obs) y_i(1)}{y_i(calc)}$$

This method is quicker than that employed in Rietveld but is not considered as physically accurate because of the arbitrarily chosen intensity. However, this will also provide an easier method of refining XRD peaks that are overlapped (similar d-spacings) between two materials since correlation of peak structure factors can cause complications in Rietveld analysis. As such, Lebail refinement can be considered an easier and faster method of data refinement that is expedient for use, though not as inclusive as Rietveld.

In this dissertation, both methods of Rietveld and Lebail refinements are used to determine transition metal and transition metal boride crystal parameters as a function of pressure. The following sections in Chapter 8 will detail the general process and softwares used for the XRD data collected in the Sample Procedures of Chapter 7. This

will also include data reduction of HPHT data from EDXD and shear strength from R-XRD using MAUD software. With the wide scope of materials studied in this dissertation, a table was made to summarize the refinement process with the sample studied.

Table 2
*Refinement Method and Software Used per Sample*

| Sample | Axial XRD Refinement | Radial XRD Refinement | Software |
|---|---|---|---|
| *Ta* | Lebail | N/A | GSAS II |
| *Os* | N/A | Rietveld | MAUD |
| $ReB_2$ | Rietveld | Rietveld | GSAS II/ MAUD |
| $Os_2B_3$ | Rietveld | N/A | GSAS II |

## 8.2.GSAS-II and MAUD Software for XRD Refinement

### *8.2.1. GSAS-II*

GSAS II, or the Generalized Structure Analysis System, is a python based open-source software developed by B. Toby and R. Von Dreele to determine sample crystal structures from diffraction experiments [67]. GSAS II supports many methods of data analysis, including Rietveld and Lebail refinement, among other alternatives such as Pawley refinement and neutron diffraction capabilities. Instrumental profile parameters containing synchrotron beam and detector calibration info can be imported into GSAS II along with sample crystallographic info from Crystallographic Information Files (CIF).

In this dissertation, instrument parameters from the beamlines at HPCAT, Advanced Photon Source, Argonne National Laboratories and CIF from the Crystallography Open Database [78] were used to provide calibration and ambient crystal models for the samples in Table 2. Prior to sample XRD importation into GSAS II, the raw XRD images were integrated into intensity - $2\theta$ plots using Dioptas [66]. The XRD intensity - $2\theta$ plots allow for refinement of intensity and determination of lattice parameters in the Rietveld/Lebail process.

### *8.2.2. MAUD*

The Material Analysis Using Diffraction, or MAUD, software is a Java based analysis program for general Rietveld and Lebail refinement [70]. MAUD combines the LST and texture analysis methods for stress produced from H.R. Wenk et al. [79] to determine hydrostatic components of compression from refinement. To accomplish this, the raw R-XRD images are integrated within MAUD in azimuthal sections of $\delta = 5°$ and plotted in intensity - $2\theta$ plots for Rietveld analysis of each section. This is done sequentially within the software for all 72 sections. Strain models for R-XRD can be chosen to refine the strain $Q(hkl)$ and determine the differential stress and shear strength using the relation $< Q(hkl) > = t/6G$. In this dissertation, MAUD was used for Rietveld refinement and determination of shear strength for the two samples *Os* and $ReB_2$ detailed in Table 2.

## 8.3. Determination of Elastic Moduli in a DAC

One can say that the main purpose the DAC was fabricated for was to determine the elastic moduli for samples under compression. Generally, determining the mechanical responses of d-spacings, lattice planes, and cell unit volume is the "bread and butter" of high-pressure research. The volume of a sample body can be related to the pressure it is subjected to by assuming finite strain and expanding the strain energy of a solid in a Taylor series. This was developed by Murnaghan [80] for treating elastic solids under finite deformation that was later expounded upon by Birch [81]. The corresponding equation of state was so named the Birch-Murnaghan (BM EoS) in dedication to both scientists and relates a material's volume and bulk moduli to the induced pressure. The 3rd Order Birch-Murnaghan is given by the equation:

$$P(V) = \frac{3}{2}K_0\left[x^{\frac{7}{3}} - x^{\frac{5}{3}}\right]\left[1 + \frac{3}{4}(K_0' - 4)\left(x^{\frac{2}{3}} - 1\right)\right] \tag{8.1}$$

where $K_0$ is the bulk modulus, $x$ is the volume ratio $V_0/V$, and $K_0'$ is the first pressure derivative. It is then elementary to determine the bulk modulus through least squares fitting of pressure-volume data.

A more modern technique that is also commonly employed is the EoS produced by Rydberg and Vinet [82] that is under the assumption that finite-strain EoS does not accurately account for volume variation in a solid under compression. This acted as a modification to the Birch-Murnaghan EoS by using a generalized inter-atomic potential to detail spacing between atoms under compression. The expression for the Rydberg-Vinet EoS is given by:

$$P = K_0 3 f_v/(1 - f_V)^2 e^{\eta f_v} \tag{8.2}$$

where $f_v$ = 1-$(V/V_0)^{1/3}$ and $\eta$ = 3($K_0$'-1). The bulk modulus $K_0$ can then be found in the slope of the fit at $f_v$ = 0 as $ln(K_0)$. Both equations of state presented here are in the form of isothermal conditions at ambient temperature. The BM EoS and Ryberg-Vinet were both employed in this dissertation to determine sample bulk moduli. For P-V-T studies, a temperature modification to the BM EoS by Fei [83] gives a volume relation to temperature at zero pressure by:

$$V_{0T} = V_{00}\exp\left(\alpha_0\left(T - T_{ref}\right) + \frac{1}{2}\alpha_1\left(T^2 - T_{ref}^2\right) - \alpha_2\left(\frac{1}{T} - \frac{1}{T_{ref}}\right)\right) \quad (8.3)$$

where $\alpha_0$, $\alpha_1$, and $\alpha_2$ are the thermal expansion coefficients (also written as *a*,*b*,*c*), $T_{ref}$ is used as ambient temperature in this dissertation, and *T* is temperature above $T_{ref}$.

### *8.3.1. Effects of Hydrostatic and Non-Hydrostatic Pressure Environments*

The equations of state listed in the previous section were each used in this dissertation to determine the bulk moduli and elastic properties of the transition metals and TMBs. The choice of which to use is mostly based on preferences and goodness of fit. However, it is important to note and discuss the effects that variations in pressure environment, whether hydrostatic or non-hydrostatic, can affect the calculation of bulk moduli and volume. For example, LST and R-XRD experiments were conducted on *FeO* (*fcc*), *Fe*(*bcc*), and *Fe*(*hcp*) by Singh et al [32] and determined that volume estimated from hydrostatic components of compression were ~1.5% smaller than the non-hydrostatic and had standard deviations 2-10 times as small. This was true for each of the *Fe* samples and suggested that volume strain is underestimated when NHS stress is ignored, thus giving a smaller volume [32]. It is then easy to see that the bulk modulus $K_0 = -\frac{V_0 dP}{dV}$ will also vary assuming the hydrostatic and non-hydrostatic measurements

use the same zero pressure and isothermal volume $V_0$. Truly, the pressure environment within the sample chamber is further complicated as the sample will typically undergo larger plastic flow with initial compression before equilibrium is reached. This can be considered the Reuss (iso-stress) condition and typically will have a higher change in lattice strain. Once the equilibrium is reached, the sample is under a more iso-strain, or Voigt, approximation for the stress state.

This problem of non-hydrostaticity and strain has long plagued DAC high pressure researchers and has led to methods of improving the pressure environment within the sample chamber. It was briefly mentioned in the *Ta* sample procedure that a neon pressure medium was used to provide a quasi-hydrostatic pressure environment. Introducing a noble gas into the DAC sample chamber is a common practice to reduce non-hydrostatic effects, however, this is at best quasi-hydrostatic and limited to ~30 GPa as the gas will crystallize and thus provide a more uniaxial compression [84-85]. The increasing viscosity of the noble gas might also induce more nonhydrostatic pressure prior to crystallization. Many equations of state describing material compression to multi-megabar pressures could underestimate/overestimate volumetric strain if the degree of hydrostaticity is not determined. This highlights the effective use of R-XRD and LST in this dissertation to estimate sample hydrostatic compression for cross-comparison with non-hydrostatic studies and DFT calculations.

## 8.4. High Pressure – High Temperature Data Reduction

Finally, the HPHT data reduction is discussed here for the $Os_2B_3$ sample procedure in Chapter 7, Section 7.4.3.2. The data collected from EDXD was analyzed

using hpMCA software to determine sample d-spacings. A sum of least squares fit was then employed to determine d-spacings from sample *hkl* peaks. This was done for each pressure and temperature step to develop P-V-T curves that were imported into EoSFit7 [86] for equation of state fitting. The 3$^{rd}$ Order BM EoS with the Fei temperature modification was employed to determine pressure-volume relations with temperature and calculate the thermal expansion coefficients.

# CHAPTER 9

# RESULTS

## 9.1. Introduction

The culmination of these studies into transition metals and transition metal borides is presented here in Chapter 9. The broad and encompassing range of the methods and materials used address some of the fundamental questions in current high-pressure studies of transition metals and high strength materials with the following aims:

1. Determine the achievable pressure ranges of custom-made T-DACs in comparison with conventional two-stage diamond anvils
2. Determine the anisotropic compression and anomalies in axial (c/a) ratio in hexagonal phase of TMBs and *Os* metal both in hydrostatic and non-hydrostatic environments
3. Comparison of theoretical and experimental shear strength measurements of TMB $ReB_2$ and *Os* metal.

## 9.2. Toroidal DAC

### *9.2.1. Achieved Pressure Limits*

First, we must look at the T-DAC accomplishments in its original task of comparing to other modern two-stage DAC techniques. The toroidal diamond anvils created via FIB machining are detailed in Table 3 with their achieved maximum

pressures. It is seen that all the toroidal diamond anvils achieved pressures greater than the conventional beveled DAC limit of 250 GPa and exceeded to pressures seen in two-stage diamond anvils (300-400 GPa). However, none made it to the claimed pressures of Sakai [29], Z. Jenei [30] and Dewaele et al. [31]. Indeed, Jenei and Dewaele each claim pressures ~500-600 GPa were achieved, twice the limit of Sample 1 planar design (Table 3) despite the similarities in toroidal anvil dimensions. Sakai et al. delivered a more moderate pressure ~430 GPa, however, they were more thorough in their cross comparison by using different equations of state for pressure calibration. Using the Anzellini EoS parameters for the *Re* pressure marker, Sakai showed a pressure in the range 430-460 GPa was achieved [29]. However, using the parameters for *Re* put forward by the Dubrovinsky group [23], pressure was shown to over-estimate to 600 GPa for the same sample volume data.

Table 3
*Design Parameters for Implementation of T-DAC*

| Sample | Culet/Total Diameter/Height | Design | Maximum Pressure (GPa) |
|---|---|---|---|
| 1. Re-Ta | $16\mu m$ / 60 $\mu m$ / 3 $\mu m$ | Planar | 265 [7] |
| 2. Re-Ta | $8\mu m$ / 30 $\mu m$ / 5 $\mu m$ | Groove | 308 [7] |
| 3. Re-Ta | $16\mu m$ / 60 $\mu m$ / 3 $\mu m$ | Planar | 299* |
| 4. $Os_2B_3$-Pt | $16\mu m$ / 60 $\mu m$ / 3 $\mu m$ | Planar | 358 [10] |
| 5. Os-Pt | $16\mu m$ / 60 $\mu m$ / 5 $\mu m$ | Planar | 288 [13] |

It is worthy of note that the claims of > 500 GPa by Jenei and Dewaele used the EoS parameters from Dubrovinsky for pressure estimation and is suggested that these numbers may be overestimated. This will be the case when the EoS and T-DAC compression *Ta* transition metal is evaluated and cross compared in Section 9.3. In application of the T-DAC and their achieved pressure limits, the experiments were largely successful in achieving up to 360 GPa of applied pressure. This is, however, still 100 GPa less than that put forward by Sakai. It is likely that the choice of anvil has some role to play in this as all diamond anvils employed in this dissertation were single crystal, while those by Sakai were nano-polycrystalline diamond (NPD) (grain sizes <10nm). It has been circulated in the HP community that diamond anvils with nano-sized grains are the key to achieving high pressure [24,29]. Further studies would need to be done to compare whether the difference in grain size of NPD compared to single crystal diamond could cause the 100 GPa difference seen here. With these preliminary studies, the TDAC is an impressive and useful tool for multi-megabar generation.

### *9.2.2. Pressure Gradients Formed at High Pressure*

The increase in achieved pressure limits by T-DAC use was the primary goal of their fabrication, while the secondary goal is to reduce the build-up of pressure gradients and reducing sample outflow. This was conducted using the grooved design of TD-2 on *Re-Ta* sample mixture (Figure 16). The grooved design essentially acts as a crevasse that will ‘pinch’ and trap the gasket material within and thus preventing the sample hole from moving off the culet. This groove can be seen in the SEM picture of Figure 16(a) and (b) which shows both anvils used for the *Re-Ta* sample compression. As the diamond anvil

culets are compressed to high pressure, they will cup inward allowing the grooves of both diamonds to seal the sample within the gasket.

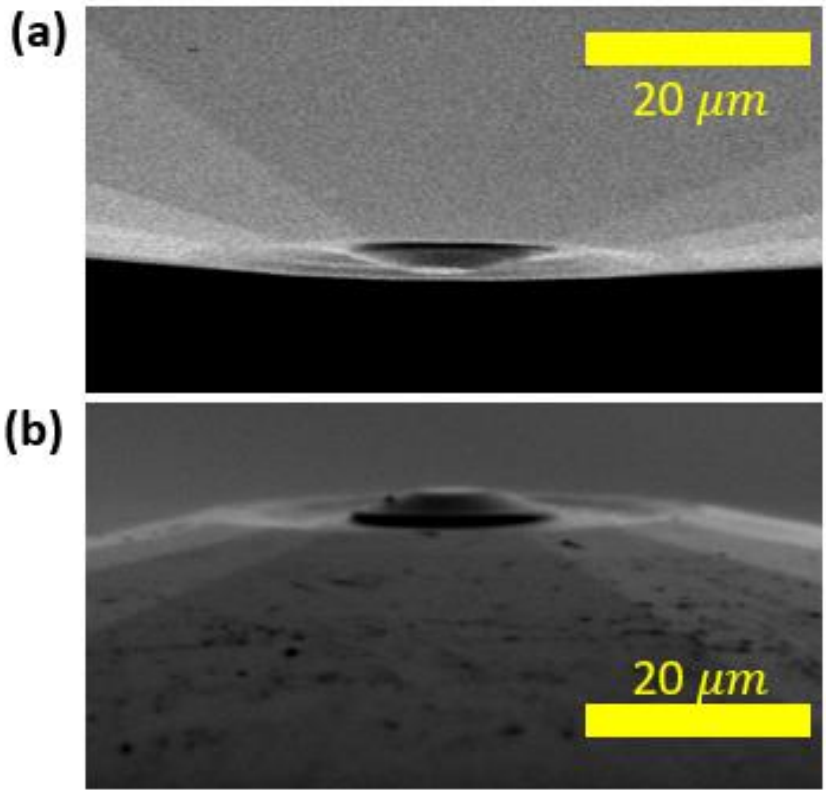


Figure 16. SEM image of both completed grooved toroidal design of TD-2 that were employed in an opposed anvil configuration for *Re-Ta* sample compression.

This cupping can be seen with the 3D image of x-ray transmission taken of the T-DAC at 250 GPa in Figure 17. As this is x-ray transmission, the red indicates higher transmission and thus thinner areas of the DAC sample chamber. The black ring shows the location of the 8-micron culet of the TD-2 design and the location of the *Re-Ta* sample. This is surrounded by a thicker blue region of the *Re* gasket that has been 'pinched' by the diamond cupping and is supporting the sample hole from misshaping or outflowing. Indeed, this at the conventional pressure limit of beveled diamond anvils and shows remarkable symmetry and sample support at such high pressure. This stability indicates the T-DAC is successful in the endeavor of sample placement stability at high pressure.

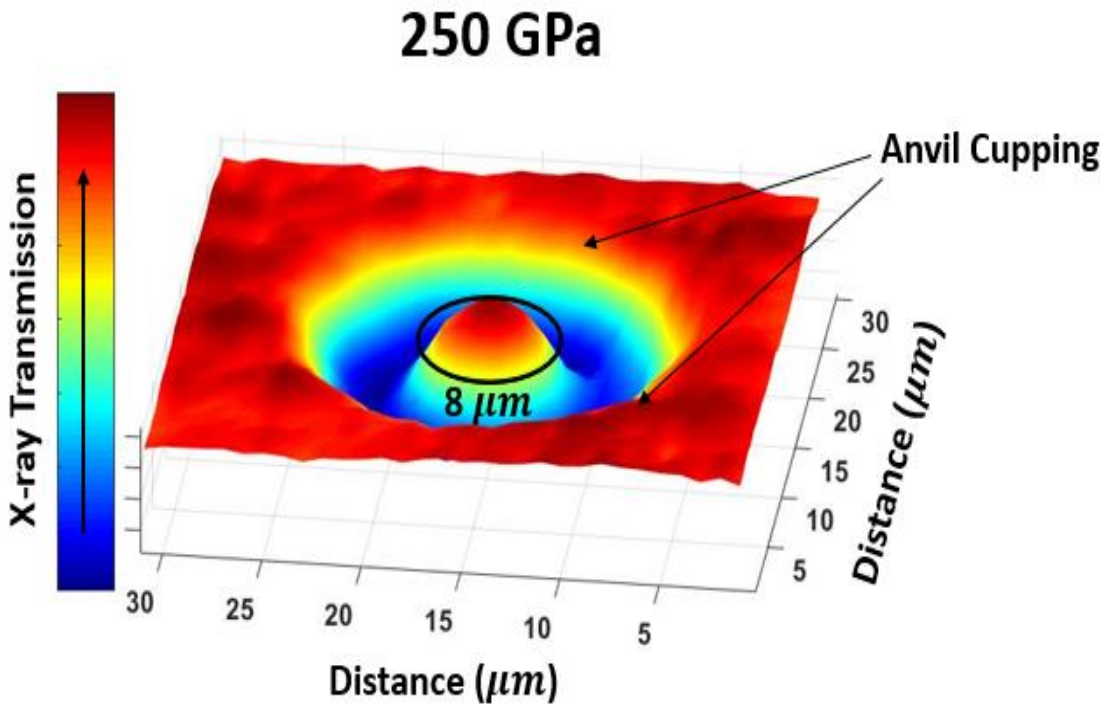


Figure 17. 3D x-ray transmission image of a T-DAC at 250 GPa taken at beamline 16-IDB, Advanced Photon Source, Argonne National Laboratory. The inner black ring indicates the location of the diamond culet and the sample.

The x-ray transmission graph was then converted into a 2D pressure distribution map to probe the pressure gradients of the *Re-Ta* sample T-DAC (Sample 2 in Table 3) at high pressure (Figure 18). In Figure 18(a), the pressure distribution of the *Re-Ta* sample mixture of T-DAC design TD-2 can be seen where Y($\mu m$) = 0 and Z($\mu m$) = 0 indicates the center of the culet at 250 GPa. Just as shown in the x-ray transmission graph, it is seen that the pressure is localized at the center of the sample. This is excellent to note as smooth, low-pressure gradients at the center of the DAC will ensure equally applied and higher achievable pressure. This is likely one of the contributing factors to this anvil's survival > 300 GPa. Figure 18(b) is a 1D x-ray pressure distribution map along the Z-axis to determine the pressure gradients in the red region at the center. A maximum pressure gradient of 13.6 microns is noted within the culet. The pressure drops ~ 40 GPa at 8 microns from the center of the culet along both the Z and Y axis, which shows an overall gradient of ~ 5 GPa/ micron. These low-pressure gradients are excellent news in the application of T-DAC technology and supports their use in reducing high pressure gradients that can fracture diamonds once it exceeds the diamond strength (130 GPa).

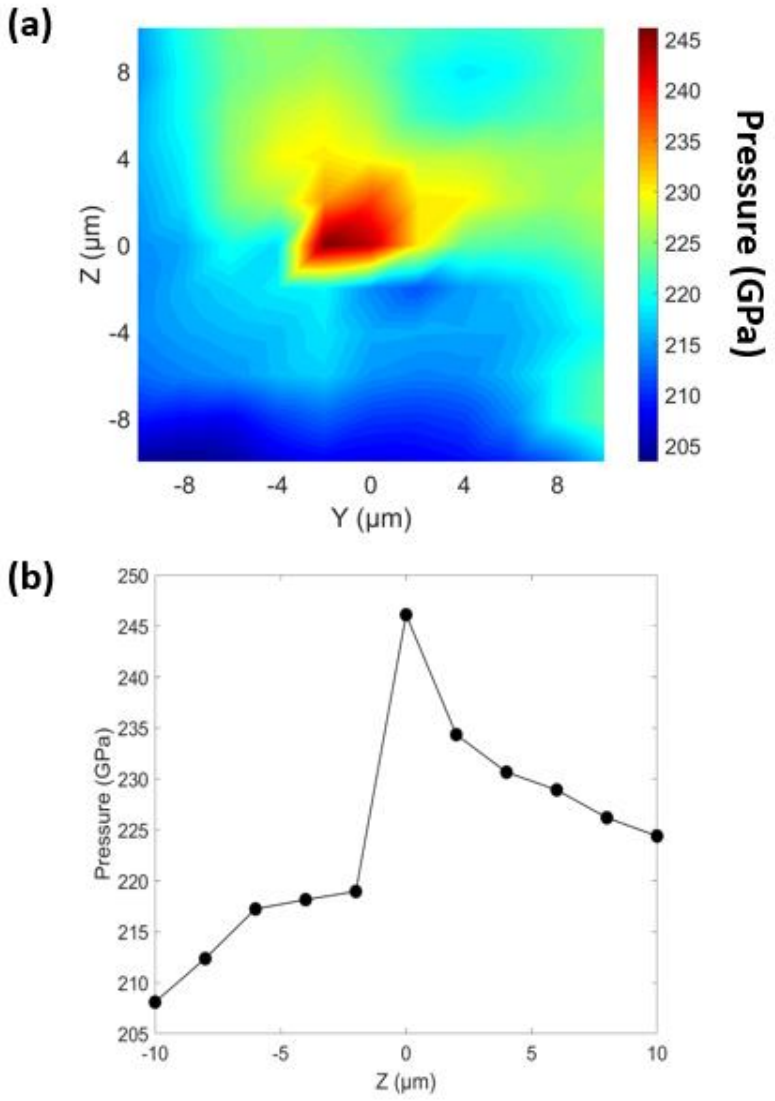


Figure 18. (a) 2D pressure distribution map of *Re-Ta* sample at max pressure of 250 GPa using T-DAC design TD-2. (b) 1D pressure distribution map along the Z-axis of the sample.

### 9.2.3. *Concluding Remarks on TDAC Compression*

The T-DACs employed from Table 3 were successful in achieving ultra-high compression and rivaling conventional two-stage diamond anvils. These also produced excellent sample support at high pressures while reducing the build-up of pressure

gradients and thus accomplishing their created design. The T-DACs produced in my dissertation, however, were systemically lower in achieved pressure than those claimed from other research groups despite similarities in dimensions. This has warranted a closer look into the probable reason for the large discrepancy to completely answer Aim 1 of this dissertation. Investigation from studies of Sakai et al. [29] showed a 200 GPa difference in pressure depending on the EoS used for pressure calibration which calls into question whether the pressures from Jenie and Dewaele are substantiated. However, Sakai used NPD with ultra-small grain sizes that are characteristically different from the single crystal anvils used by the other groups. Therefore, the NPD anvil results may not be the best suitable comparison. To answer this new question in the realistic T-DAC pressure achievement, the *Ta* EoS produced from single crystal T-DAC in this study is used in a cross comparison with other EoS. This is further expounded upon in the following section of 9.3.

## 9.3.Tantalum EoS over 300 GPa

### *9.3.1. Introduction*

Tantalum transition metal offers an excellent opportunity to provide a new high pressure isothermal calibration because of its volumetric stability. This has incentivized this study into > 300 GPa equation of state formation to understand *Ta* behavior at high pressure and offer a cross comparison with other known equations of state to solve this disparity in the high-pressure community of achieving T-DAC static pressures > 400 GPa. The results presented here are from non-hydrostatic compression experiments from Samples 1 and 2 that are displayed in Table 3. Both the planar and grooved T-DAC

design were used to compress the *Ta-Re* sample mixture to 265 GPa and 308 GPa where *Re* was used as the pressure calibration. This work was done in collaboration with Los Alamos National Laboratory–Shock and Detonation Physics Group who provided quasi-hydrostatic compression of to 80 GPa [7].

### *9.3.2. Non-hydrostatic and Quasi-hydrostatic Compression of Ta*

The compression of *Ta* metal was split into three separate DAC experiments as detailed in Chapter 7, Section 7.4.1. Two high pressure non-hydrostatic experiments were conducted using torodial anvil designs TD-1 and TD-2 and will hence be designated as NHS-1 and NHS-2 respectively. The third experiment utilized the standard 200 micron flat dimaond anvils for quasi-hydrostatic compression. The axial XRD images taken at the maximum pressure of NHS-1 (267 ± 6.90 GPa) and NHS-2 (308 ± 8.00 GPa) can be seen in Figure 19(a) and (b). This pressure was determined using the EoS parameters of *Re* put forward by Anzellini et al. [38] with $K_0$ = 352.6 GPa and $K_0$' = 4.56. It becomes worthy of note that the TD-1 design used in NHS-1 produced a more appealing XRD image at the maximum pressure compared to the TD-2 design. This is likely contributed from the larger culet size (16 microns) compared to the x-ray beam size of 1 μm (vertical) ×2 μm (horizontal). A smaller beam-to-culet ratio will reduce the observation of pressure gradients in the material. An excellent example of this is in the smaller culet (8 micron) of NHS-2 where XRD images above 190 GPa display bimodal peaks for each *Ta-Re hkl*.

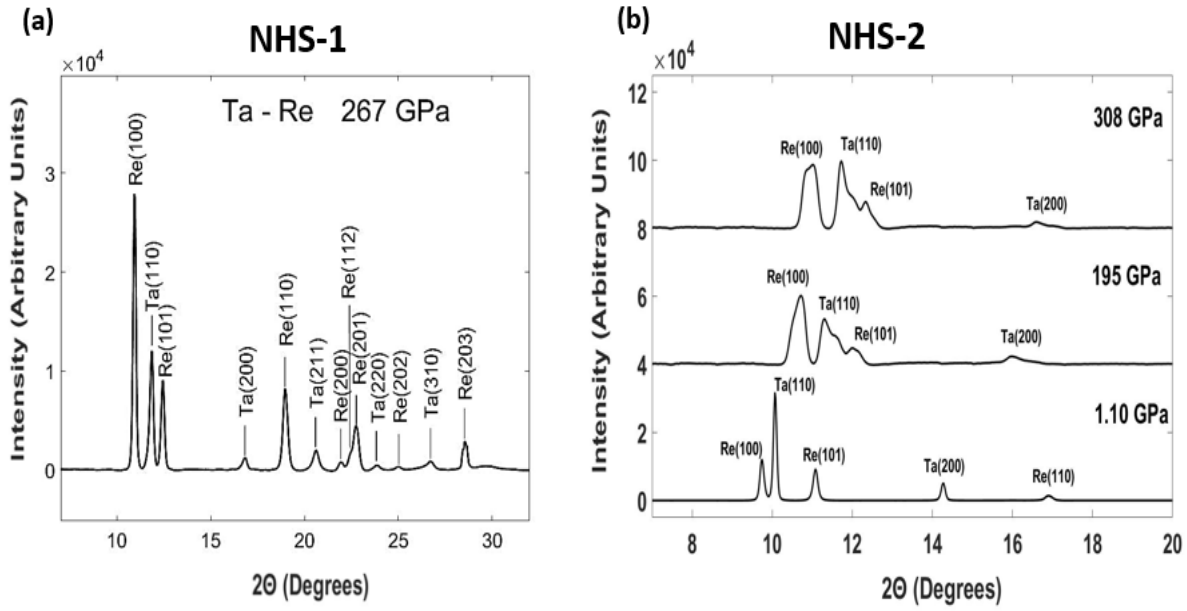


Figure 19. (a) Integrated XRD diffraction patterns of the *Ta-Re* foils at 267 GPa produced by the T-DAC design TD-1. (b) Integrated XRD image of *Ta-Re* at 308 GPa using TD-2 design.

Structural refinement of *Ta* lattice parameters to the maximum pressure revealed it to be stable in the body-centered-cubic form to the maximum pressure giving lattice parameter $a = 2.755 \pm 0.003$ Å with $V/V_0 = 0.581 \pm 0.009$ at 308 GPa. This is evidenced by the smooth pressure – volume curve seen in Figure 20 of the non-hydrostatic pressure and with the quasi-hydrostatic equation of state from the *Ta-Au* mixture in Figure 21 (a). The first interest of a *Ta* EoS is establishing the accuracy of volume response to pressure. As discussed in previous sections, the volume and bulk moduli may vary depending on the type of pressure environment. However, the non-hydrostatic data in NHS-2 is in very good agreement with the quasi-hydrostatic data in Figure 21(b). In fact, it is within a 2.5 GPa difference, which is within the yield strength of *Ta* (4 GPa).

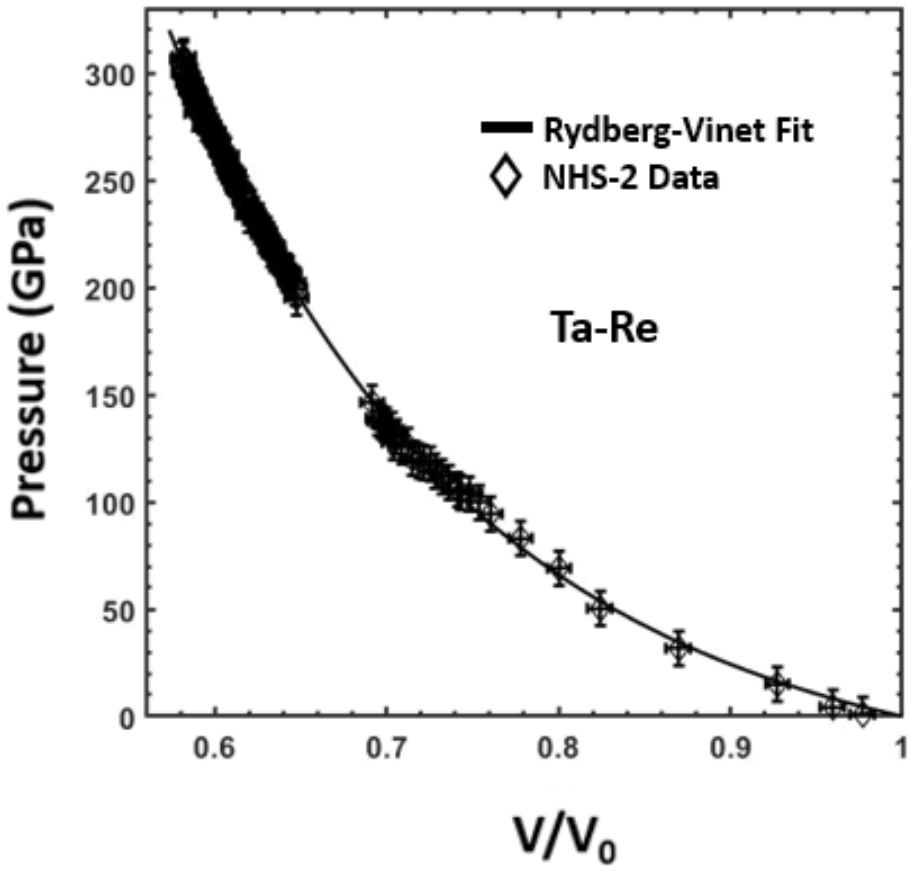


Figure 20. Rydberg-Vinet fit to the *Ta-Re* compression data to a maximum pressure of 308 GPa.

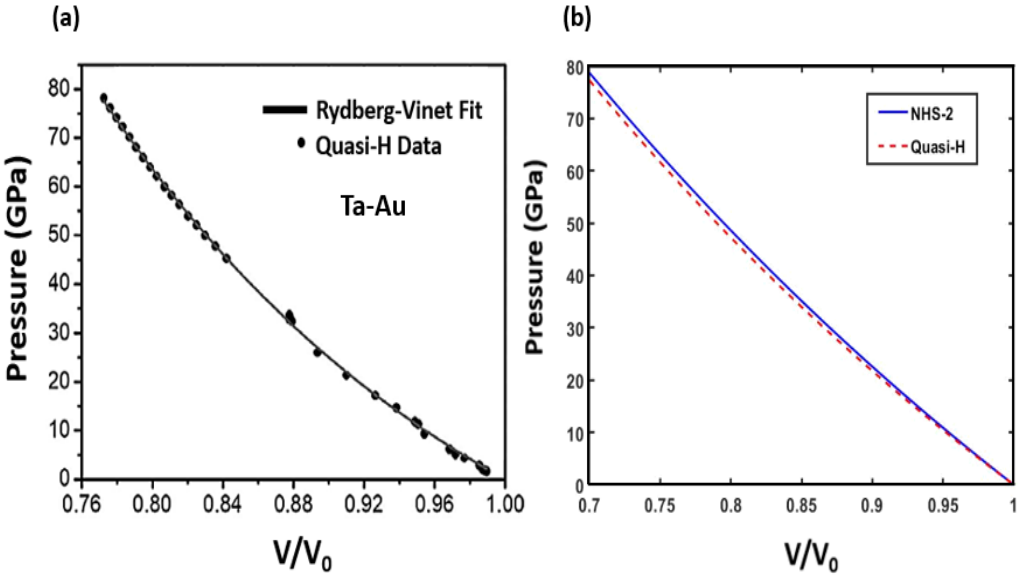


Figure 21. (a) Quasi-hydrostatic compression of *Ta* with *Au* pressure marker to 80 GPa. (b) Comparison of nonhydrostatic and quasi-hydrostatic.

### *9.3.3. Cross Comparison of Tantalum Equation of State*

Aim 1 of this dissertation seeks to use T-DAC to generate ultra-high pressure equations of state for new and intriguing studies into transition metals and their borides. However, pressure achievement previously discussed has posed a problem for Aim 1 as T-DAC compression is only as accurate as the EoS used for calibration. A cross comparison of *Ta* EoS with other studies using *Re* as a pressure marker will serve a dual purpose: 1) determine accuracy of the new *Ta* EoS and 2) conclusively respond to the inability of the T-DAC in this study to achieve > 400 GPa. To begin, the equation of state for *Ta* produced in NHS-1 experiment is plotted with two separate EoS fits and a shock derived isotherm from McQueen et al. [69]. When *Ta* volume data is plotted with EoS parameters of *Re* from Anzellini [38], we can see that there is general agreement to 230 GPa with only ~10 GPa difference at the same volume for the shock data (Figure 22). This is not considerably above the error at the maximum pressure of NHS-1 (267 ± 6.90 GPa). In stark comparison, the same *Ta* data from NHS-1 fitted with Dubrovinky et al. parameters for *Re* [23] shows ~85 GPa disparity for the same given volume at the maximum pressure of 267 GPa. Indeed, this would be a very successful T-DAC design if the pressure of 350 GPa was claimed, however, this difference is also seen with studies from Sakai et al. who also noted a drastic overestimation of pressure when using Dubrovinsky parameters [28,29]. The more conservative value of 267 ± 6.90 GPa is necessitated. This disagreement in pressure calibration is exacerbated when observing the NHS-2 experiment that achieved 308 GPa of static pressure with an Anzellini fit. Here, again we see relative good agreement between the shock derived isotherm and the non-

hydrostatic compression. However, the fit with Dubrovinsky *Re* pressure calibration has overestimated ~114 GPa. The derived bulk moduli from these EoS fits are shown in Table 4.

Table 4

*Determined Equation of State Fit Parameters for Tantalum*

| Experiment | Pressure Marker | Max pressure (GPa) | Bulk Moduli (GPa) |
|---|---|---|---|
| NHS-2 (Anzellini EoS Fit [38]) | Re | 308 | $K_0$ = 186.6 ±2.0, $K_0$' = 4.36±0.05 |
| NHS-2 (Dubrov. EoS Fit [23]) | Re | 422 | $K_0$ = 166.1 ±1.4, $K_0$' = 6.05±0.01 |
| Shock Compr. [74] | -- | 230 | $K_0$ = 189.4 ±1.8, $K_0$' = 3.90±0.05 |
| Quasi-Hydro [7] | Au | 80 | $K_0$ = 201.0 ±2.4, $K_0$' = 3.21±0.11 |

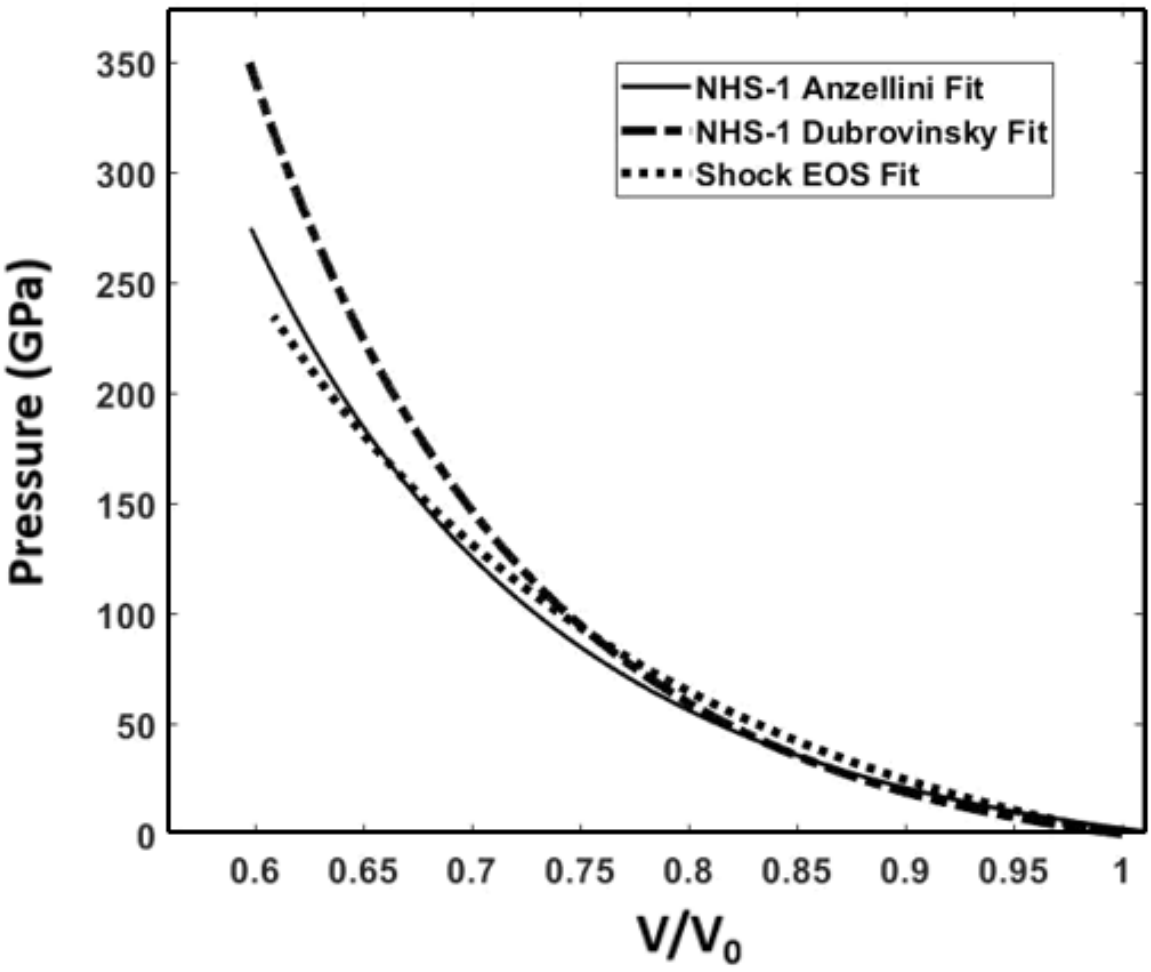


Figure 22. The comparison of *Ta* equation of state using Anzellini et al. *Re* pressure calibration [38], Dubrovinsky et al. [23], and a shock derived isotherm from McQueen at el [69] for NHS-1 experiment.

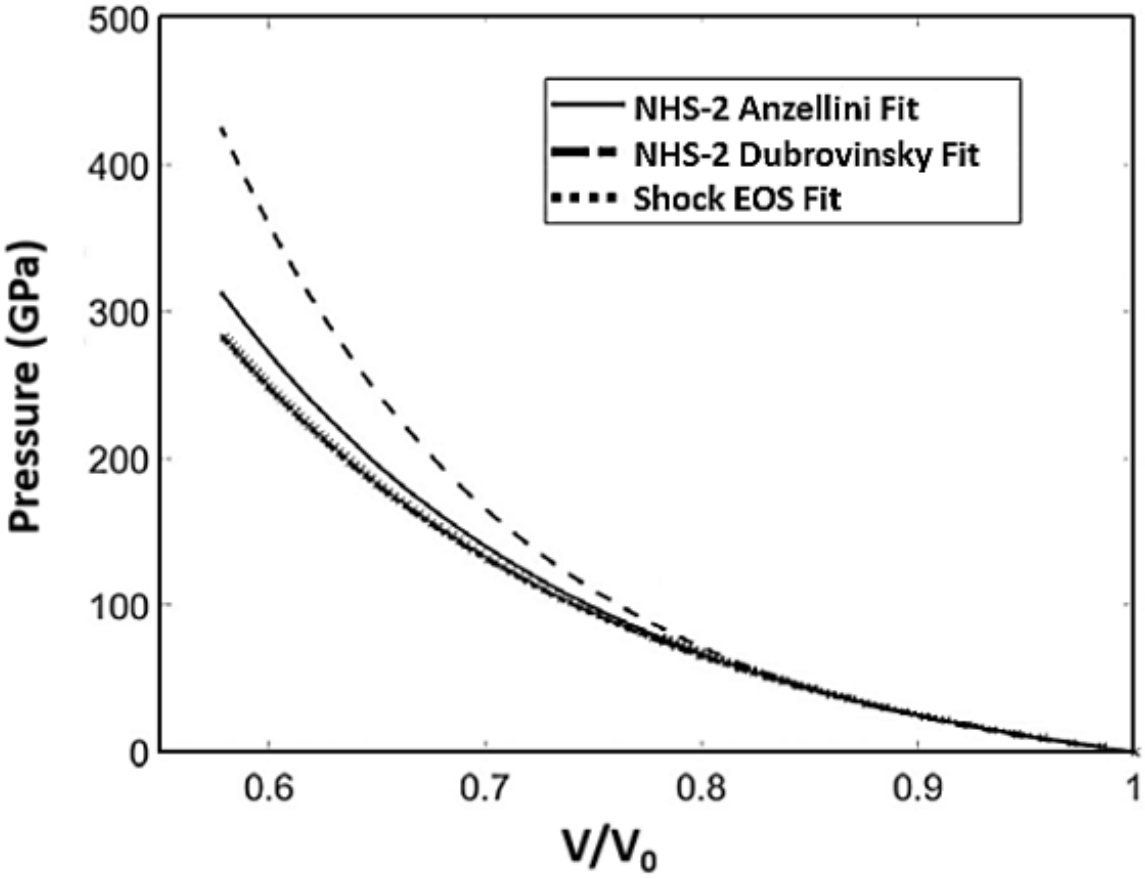


Figure 23. The comparison of *Ta* equation of state using Anzellini et al. *Re* pressure calibration [38], Dubrovinsky et al. [23], and a shock derived isotherm from McQueen at el [74] for NHS-2 experiment.

### *9.3.4. Concluding Remarks on Ta EoS and TDAC Compression*

From Table 4, we can see that the EoS parameters using Anzellini et al. are in very good agreement with those from shock compression and quasi-hydrostatic studies. Therefore, it has been proposed that NHS-2 experimental results to 308 GPa establish an accurate EoS for *Ta* metal and a new high-pressure standard for future DAC experiments. This work has been published in *High Pressure Research* [7] journal and has attracted attention for other studies at Los Alamos National Laboratories where the T-DAC and *Ta* data was used to provide strength measurements of *Ta* for the first time to 276 GPa [15]. This highlights the efficacy of this study into *Ta* and collaboration in a scientific nature.

Finally, it is evidently seen that the success of the T-DAC pressure achievement for > 400 GPa is somewhat overestimated in other literature. Jenie et al. [30] and Dewaele [31] have both claimed > 500 GPa of pressure using the *Re* equation of state from Dubrovinsky et al. As shown in this study, the Dubrovinsky parameters would have given the T-DACs in this study an achieved pressure of up to 422 GPa for *Ta* sample and thus solidifying it as a useful alternative to conventional NCD two-stage anvils. This study, along with Sakai et al. and Anzellini et al. [38], has collectively shown a more conservative limiting pressure of the TDAC to 265–400 GPa depending on culet size, dimensions, and anvil crystalline nature. Further studies into T-DAC developmental characteristics are thus needed to understand the full extent of the T-DAC pressure range. However, this study has shown with *Ta* to 308 GPa (and later $Os_2B_3$ to 358 GPa) that the T-DAC can rival the NCD two-stage anvil and was successful in reducing sample outflow and pressure distribution [7,8,13,15]. Therefore, Aim 1 into developing TDAC in comparison to two-stage NCD anvils has been successfully accomplished.

### 9.4. Osmium Hydrostatic EoS and Shear Strength

Under Aims 2 and 3 of this dissertation, understanding the behavior of transition metal and their borides in extreme environments has brought attention to *Os* metal. *Os* is the most incompressible naturally occurring metal that has given it a high value for industrial applications, however, it has displayed anomalies in axial lattice parameter ratios ($c/a$) that has caused some confusion as to their location with pressure and reason for being. Ocelli et al. claimed anomalies in c/a ratio at the pressure location of 25 GPa [44] while Dubrovinsky et al. claimed an anomaly at 150 GPa [45] while others have

noted a smooth monotonic increase in *c*/*a* [46]. Perreault et al. also noted a large dip in *c*/*a* ratio centered around 70 GPa in non-hydrostatic compression of *Os* to 207 GPa [43]. Indeed, such a broad spectrum of anomaly locations has warranted further study into the *Os* lattice parameters with pressure.

Shear strength measurements of *Os* metal to very high pressure have also not been conducted. This offers an opportunity to use R-XRD and LST to not only provide first time shear strength measurements of *Os* > 150 GPa, but also to use the hydrostatic compression measurements from LST to probe the issue of lattice parameter anomaly and its relation to the induced pressure environment. The results presented here have been published in reference [13] and provide hydrostatic pressure-volume measurements and shear strength of *Os* to 170 GPa and are compared with other non-hydrostatic and DFT calculations. This will show the anomalies in *c*/*a* lattice parameter ratio are indeed related to the non-hydrostatic/hydrostatic pressure state of the sample in a DAC.

### *9.4.1. Report on EoS and c/a ratio for Osmium*

High pressure experiments into *Os* metal using R-XRD was combined with previous compression values from reference [43] using standard DAC compression to 207 GPa. A T-DAC using the planar design of TD-1 was also included to extend the EoS to 280 GPa in comparison with R-XRD measurements to 170 GPa (Chapter 7, Section 7.4.2) [13]. The EoS fit results of the non-hydrostatic *Os*-DAC and *Os*-TDAC experiments are displayed in Figure 24 with a well fitted 3$^{rd}$ Order BM EoS. The derived bulk modulus $K_0$ = 453 GPa and $K_0$' = 3.9 from the combined data is also well represented by other literature values [39-43]. What is of more interest, however, is the axial compression ratio *c*/*a* in comparison with the other literature.

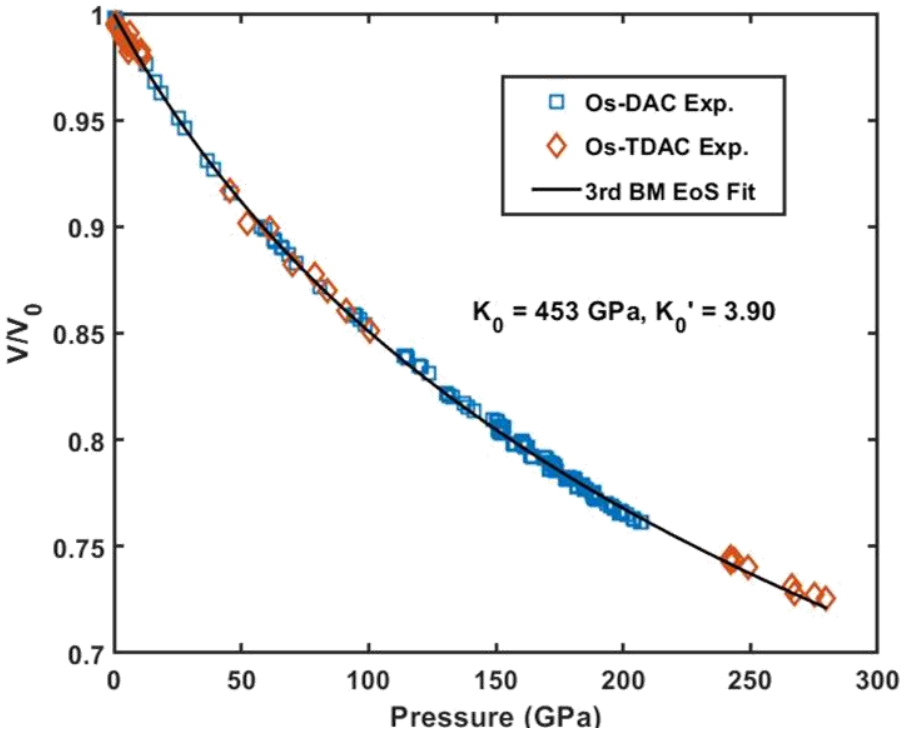

Figure 24. Measured EoS of *Os* up to 280 GPa from standard DAC and T-DAC under non-hydrostatic conditions.

In Figure 25, there is a similar overlay of non-hydrostatic *Os*-DAC and *Os*-TDAC experimental results that feature two anomalies in the *c*/*a*. The first occurs just below 15 GPa and is represented by a steep increase to *c*/*a* =1.584 before descending to the local minimum centered around 70 GPa at *c*/*a* ~ 1.57. The *c*/*a* ratio then takes a monotonic increase up to the maximum pressure and is observed in both separate compression experiments. Neither location of the anomalies corresponds with those cited in other literatures and seems to only complicate this issue. The spread and randomness of the *c*/*a* anomaly amongst the literature values seems to suggest it may be electronic transitions induced by compressive strain from the pressure environments.

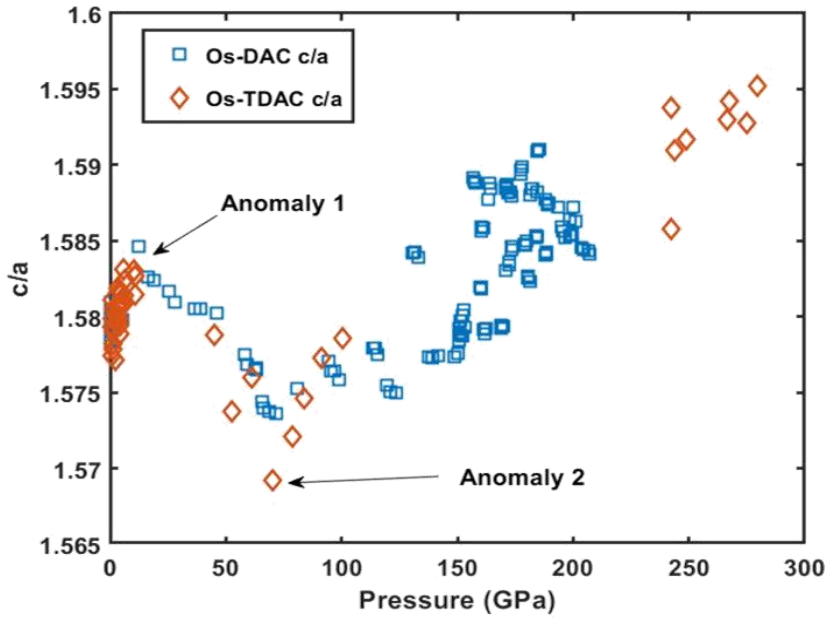


Figure 25. The variation of axial c/a ratio for *Os* to 280 GPa in two different non-hydrostatic experiments showing remarkable reproducibility.

R-XRD measurements of *Os* volumetric and axial compression have allowed the estimation of hydrostatic values by use of LST for the first time to 170 GPa. The fitted EoS of the *Os*-Hydro data can be seen in Figure 26 with the 3rd Order BM fit and derived moduli values $K_0$ = 427 GPa and $K_0$' = 4.51. Again, the fitted results lie in the middle range of literature values (382-476 GPa) and provide an experimental comparison to hydrostatic calculations from DFT-GGA models. These results were published in reference [13] with DFT calculations provided by Chia-Min Lin et al. from the University of Alabama at Birmingham.

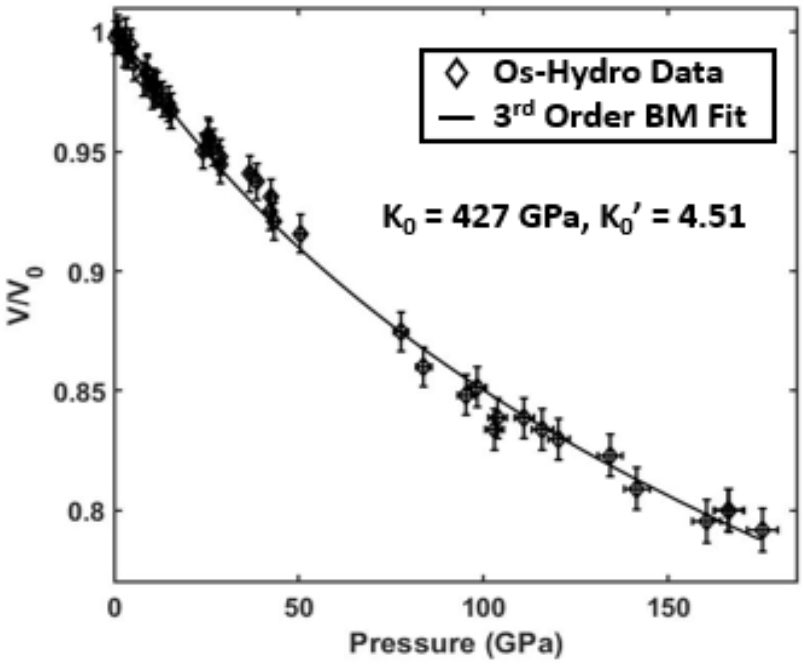


Figure 26. Hydrostatic pressure-volume data from R-XRD for *Os* to 170 GPa and the equation of state fit to the data with fit parameters indicated.

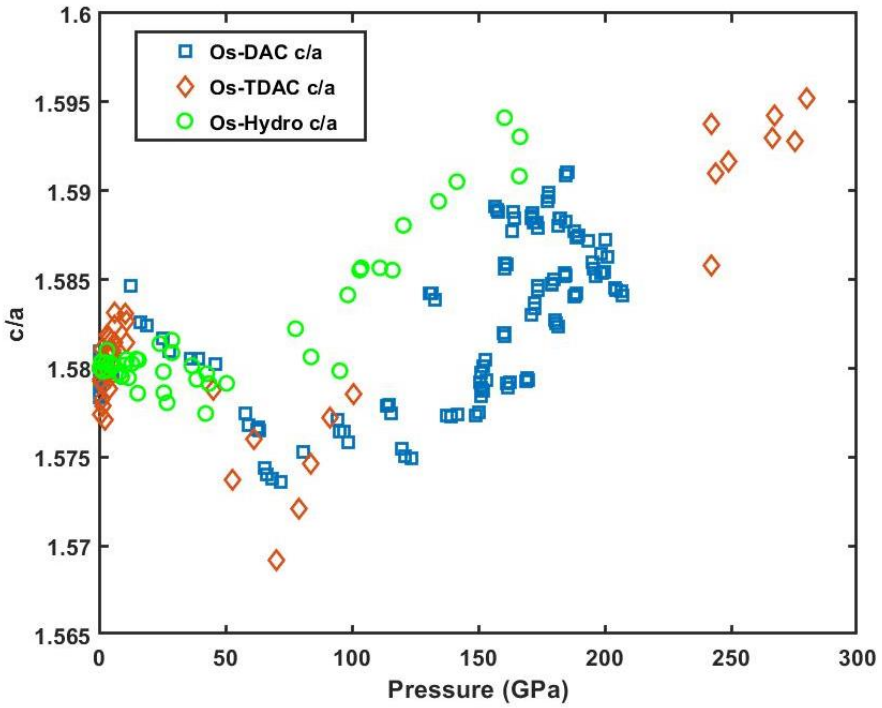


Figure 27. Comparison of axial c/a ratio for nonhydrostatic and hydrostatic compression experiments.

The measured ambient lattice parameters from experimental values $a_0$ = 2.755 Å and $c_0$ = 4.345 Å were only within 1% error from the DFT calculations and were also well represented by DFT volume compression. However, DFT calculations did not provide any simulations that replicated the *c*/*a* anomalies. This is interesting, as the simulations were done under hydrostatic pressure and zero temperature. It may suggest that the anomalies are indeed due to non-hydrostatic compression, but it cannot be ruled out that the anomalies may just not be visible at the zero temperature DFT value. To help validate the DFT calculations, hydrostatic compression values from R-XRD and LST of axial *c*/*a* ratio are presented in Figure 27. The *Os*-Hydro data did not display any anomaly in the *c*/*a* ratio up to the maximum pressure and showed a smoother increase than the non-hydrostatic values and was in better agreement with DFT [13]. However, it is difficult for DFT theory to fully relax the crystal structure to probe the electronic interaction effects in NHS environments. Thus, a conclusive understanding of the root cause of the anomalies is not available yet, but R-XRD studies suggest it is only seen in non-hydrostatic environments.

### *9.4.2. Shear Strength Determination to Multi-Megabar Compression*

Osmium has sealed itself as a highly incompressible material with a bulk modulus rivaling that of diamond, but this does not necessarily translate to a high yield or shear strength. With no shear strength measurements on *Os* to ultra-high pressure, it then becomes intriguing to determine strength measurements into this highly incompressible material to observe the plastic deformation limits. As discussed in Lattice Strain Theory of Chapter 4 and R-XRD in Chapter 7.2, shear strength measurements can be determined

from the measured d-spacing variations with x-ray diffracting angle $\theta$ and azimuthal angle $\delta$ under certain strain/stress models. In this study, the Voigt approximation (iso-strain) for shear modulus $G_V$ was assumed to reduce Equation 4.3 into the form $t = 6G < Q(hkl) >$ where *t* is the differential stress, *G* is the aggregate shear modulus, and *Q(hkl)* is the lattice strain for each Miller indices. This is advantageous as only the aggregate shear modulus *G* is needed as opposed to the Reuss model (iso-stress) that requires a lattice dependent *G(hkl)*.

The integrated R-XRD images of *Os* can be seen in Figure 28 (a) and (b) at low pressure (0.8 GPa) and at 60 GPa. The evidenced 'wavy' feature is noted in the high-pressure image (b) and indicates lattice strain causing variation in d-spacings for each *hkl*. Using Rietveld analysis and LST in MAUD software, the lattice strain term Q(*hkl*) was fitted to match the R-XRD data and determine the average value of lattice strain $< Q(hkl) >$. MAUD Rietveld refinement fits can be seen in Figure 29 (a) and (b) for low pressure and high-pressure *Os-Pt* sample mixture. The MAUD fits are displayed on top while the raw data is on the bottom. The dashed line at azimuthal angle $\delta = 0°$ shows the axis of maximum compression and thus largest distortion of d-spacing.

From the Rietveld refinement with LST in MAUD, *Os* sample hydrostatic d-spacings and lattice strain terms for *Q*(*hkl*) were determined. However, a calculation into *Os* aggregate shear modulus *G* to the pressure of 170 GPa would be needed to determine the differential stress $t = 6G < Q(hkl) >$. This was obtained by DFT calculations [13] and employed to determine an estimate on the shear strength of *Os* by $\tau = t/2$. The results of which are plotted in Figure 29 with hydrostatic *Pt* pressure to 170 GPa.

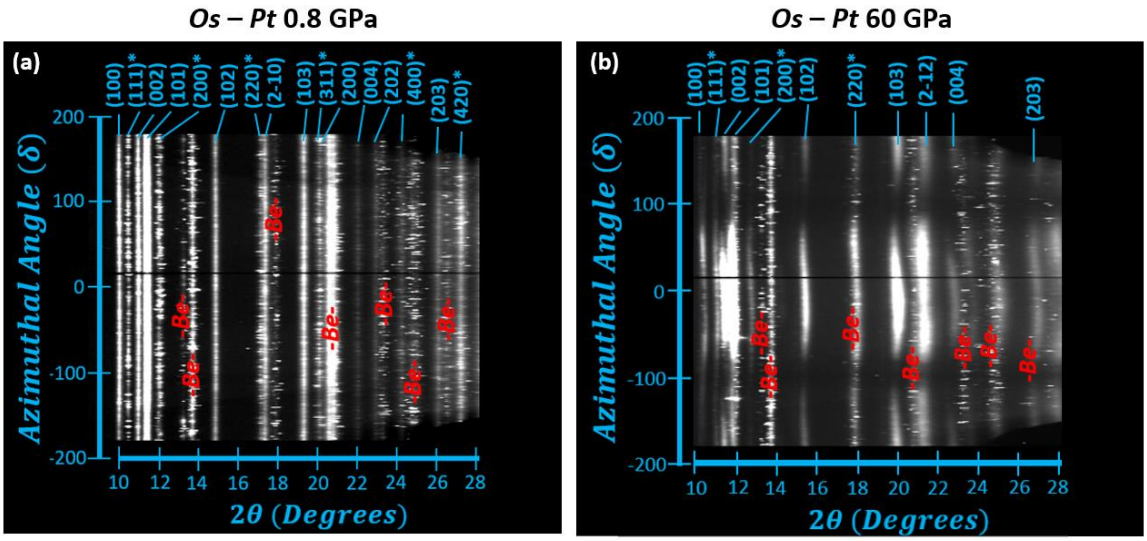


Figure 28. (a) Integrated R-XRD image of *Os-Pt* sample mixture at 0.8 GPa. (b) *Os-Pt* mixture at 60 GPa. The enhancement of 'wavy' *hkl* features indicates an increase in lattice strain from increased differential stress at high pressures. R-XRD labeled with red are *Be* gasket *hkls*.

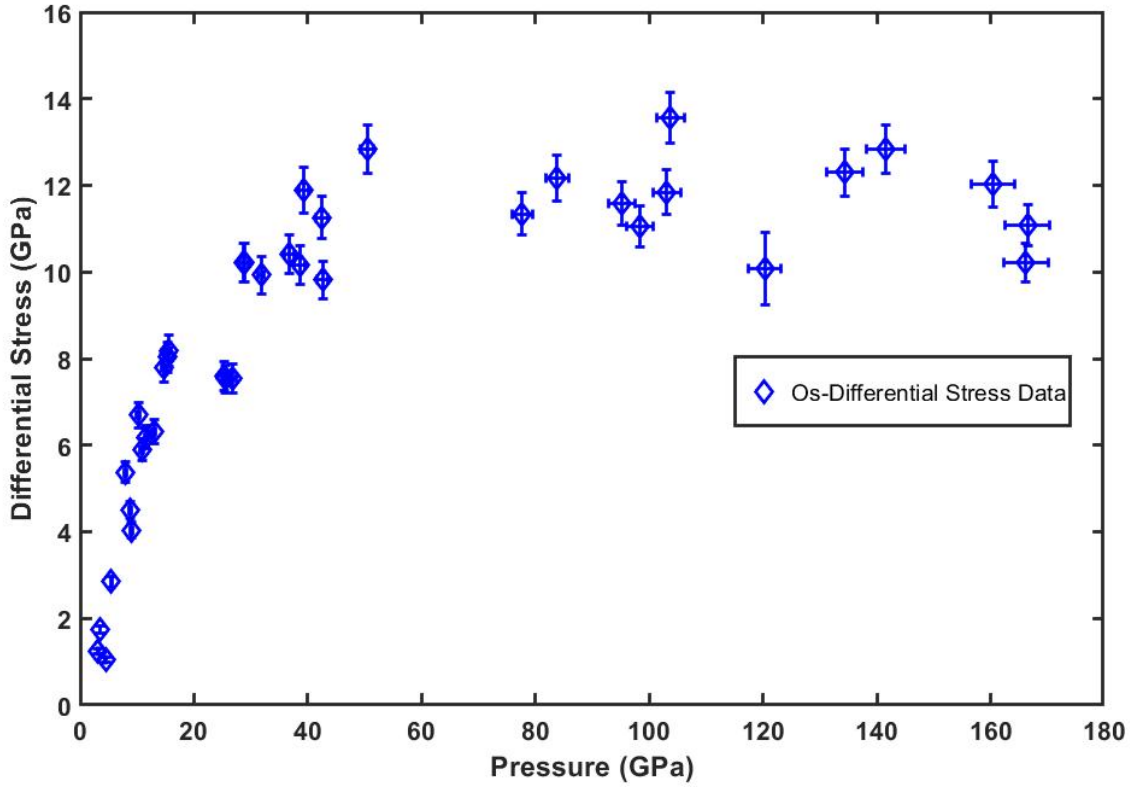


Figure 29. Differential stress in *Os* plotted with hydrostatic pressure measurements from *Pt* pressure marker to 170 GPa.

The plotted differential stress of *Os* plateaus at $t$ ~ 12 GPa after a sharp increase in the compressive region 0–40 GPa. This maximum differential stress corresponds to a shear strength of $\tau \sim 6$ GPa.

### *9.4.3. Comparison of Theoretical and Experimental Shear Strength*

In fulfillment of Aim 3 of this dissertation to compare the experimental strength of transition metals and their borides to those from theoretical derivations, ideal shear stress measurements were done via DFT [13] from Chia Min et al. at UAB to learn more on deformation mechanisms in *Os*. The results of the maximum shear stress $\tau$ from DFT are listed in Table 5.

Table 5
*Max Shear Stress and Critical Strain of Os Sample from DFT Calculations*

| Direction | Max Shear Stress – $\boldsymbol{\tau}$ (GPa) | Critical Strain - $\boldsymbol{\varepsilon}$ |
|---|---|---|
| (001)[110] | 25.99 | 0.16 |
| (001)[1-10] | 23.53 | 0.13 |
| (110)[001] | 35.03 | 0.20 |
| (110)[1-10] | 34.57 | 0.18 |
| (1-10)[001] | 23.67 | 0.12 |
| (1-10)[110] | 30.21 | 0.17 |

We now see from the values in Table 5 that the experimental observation of shear strength $\tau \sim 6$ GPa is much lower than the DFT counterpart. It is important to note that application of the Voigt approximation for shear strength provides a lower bound to the strength as the lattice dependent shear moduli term $G_R(hkl)$ is not addressed. It is also important to note that the DFT calculations were performed under the pretense of perfect crystal and are thus ideal values. Experimental values are from physical samples containing defects or impurities that weaken the mechanical strength. Based on Equation 4.3, a measurement of lattice strain is both dependent on the Reuss ($G_R(hkl)$) and Voigt ($G_V$) approximation for shear modulus:

$$Q\ (hkl) = \frac{t}{3}\{\alpha[2G_R(hkl)]^{-1} + (1-\alpha)(2G_V)^{-1}\}$$

However, there remains an experimental difficulty in determining the how much the weighted value of $\alpha$ varies between 0 (Voigt) and 1 (Reuss) [32,33]. Since this issue was avoided in the experimental study by assuming $\alpha = 0$, a lower bound was provided to *Os* shear strength ($\tau \sim 6$ GPa) and an upper ideal bound was provided by DFT ($\tau \sim 23.5$ GPa) [13].

### *9.4.4. Concluding Remarks on Os Studies*

Indeed, *Os* metal has received no lack of attention in literature due its superb physical qualities. The study into *Os* presented here in this dissertation has sought to extend the knowledge into *Os* by providing a first time look into estimated hydrostatic compression and shear strength values to 170 GPa. The anomalies in *c*/*a* ratio of *Os* from literature [39-46] remained unverified in their location with applied pressure, but hydrostatic measurements helped suggest the possible cause to be non-hydrostatic conditions causing particular electronic interactions. Though *c*/*a* anomalies were unverified by DFT calculations, the lack of anomalies also seen in the hydrostatic values suggests a future experiment into electronic interactions under NHS and hydrostatic conditions that might lead to a better understanding. This work has fulfilled Aims 2 and 3 of this dissertation and can be found in the published article of reference [13].

## 9.5. $ReB_2$ Hydrostatic EoS and Shear Strength

### *9.5.1. Introduction*

Previously, I have shown the transition metals *Ta* and *Os* mechanical behaviors to high pressure using a variety of x-ray diffraction techniques. This has probed into the

effects that hydrostatic and non-hydrostatic pressure environments have had on sample volumetric and axial compression. From here forward, these same experimental techniques are used to express how these pressure environments affect the intriguing field of transition metal borides. To begin, $ReB_2$ is first considered. As detailed in Chapter 6, $ReB_2$ has puckered layers of *B*-atoms that crystallize into a stable hexagonal lattice. The lattice parameters *a* and *c* have shown high anisotropy that increases with applied pressure, however, literature values only have maximum compression to < 50 GPa while maintaining mostly NHS and quasi-hydrostatic pressure mediums.

This section gives high pressure equations of state of $ReB_2$ for the first time to 241 GPa to study anisotropy in lattice parameters and behavior in the multi-megabar regime. These are compared with R-XRD and LST approaches to validate axial anisotropic nature in hydrostatic compression. Finally, differential stress measurements of $ReB_2$ are extended to over 5 times the previous literature value [54] and are compared with double compressed $ReB_2$ to observe the differences in powder vs solid bulk compression. This study has resulted in two publications [9, 12] and further enhanced the understanding of $ReB_2$ under high pressure.

### *9.5.2. High Pressure EoS – Hydrostatic vs Non-Hydrostatic*

Non-hydrostatic compression of $ReB_2$ was done using two separate standard DAC with 30-micron culets for pressures of 105 GPa and 241 GPa (Chapter 7, Section 7.4.4.2). Pressure and volume data determined from Rietveld refinements are plotted for both experiments and fitted with the 3$^{rd}$ Order BM EoS. The NHS compression below 35 GPa for both experiments exhibited a unique feature of uniaxial compression that has not been

noted in other literature [53-55]. This transitions into an NHS compression curve above 35 GPa to the maximum pressure. Fitting the data above the uniaxial region derived a bulk modulus and pressure derivative of $K_0 = 364\ GPa$ and $K_0' = 3.53$ that is in good agreement with lower pressure literature values 334-360 GPa [54-55].

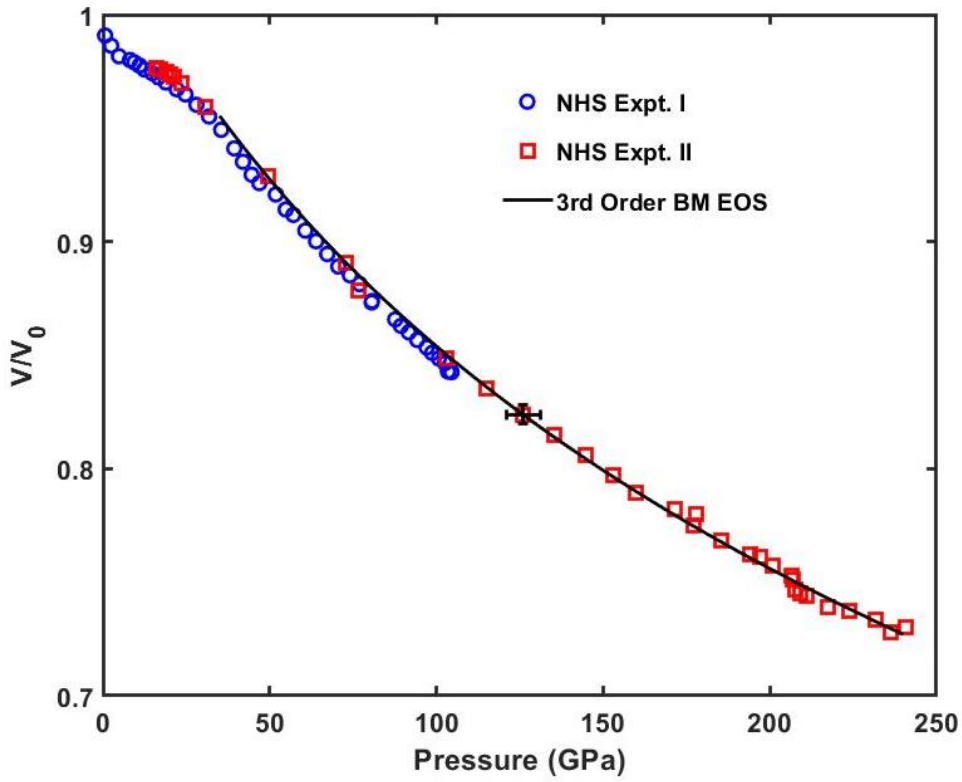


Figure 30. Nonhydrostatic compression data for $ReB_2$ to 241 GPa fitted with the 3rd Order BM EoS. The anomaly at low pressures below 30 GPa is attributed to non-hydrostatic effects.

The NHS axial compression of $ReB_2$ revealed strong anisotropy between the *a* and *c*-axis with the *c*-axis being the most resistant to compression [Figure 31]. In fact, the *c*-axis was only compressed 8% at the maximum pressure of 241 GPa (2/3rd the pressure at

the Earth's core). This strong resistance to compression and anisotropy persisted throughout the duration of compression with lattice parameters $a$ =2.586 ± 0.004 Å and $c$ = 6.882 ± 0.007 Å at the maximum pressure. To understand the cause of high resistance to deformation and increasing anisotropy, DFT calculations were conducted at the University of Alabama at Birmingham by the theoretical studies group led by Dr. Cheng-Chien Chen. DFT calculations with the GGA functional revealed a high density of states (DOS) at the fermi level [9]. The Coulomb repulsion resulting from this is increased with pressure as hydbridizations of *Re-B* and *B-B* bonds increases causing higher electron densities along the *c*-axis more so than the *a*. The DFT calculations of axial compression were in excellent agreement with values $a/a_0$ = 0.891 and $c/c_0$ = 0.919 (within 3% error of experiment) and replicated the anisotropy to 240 GPa. Further details and methods of DFT calculations can be found in reference [9].

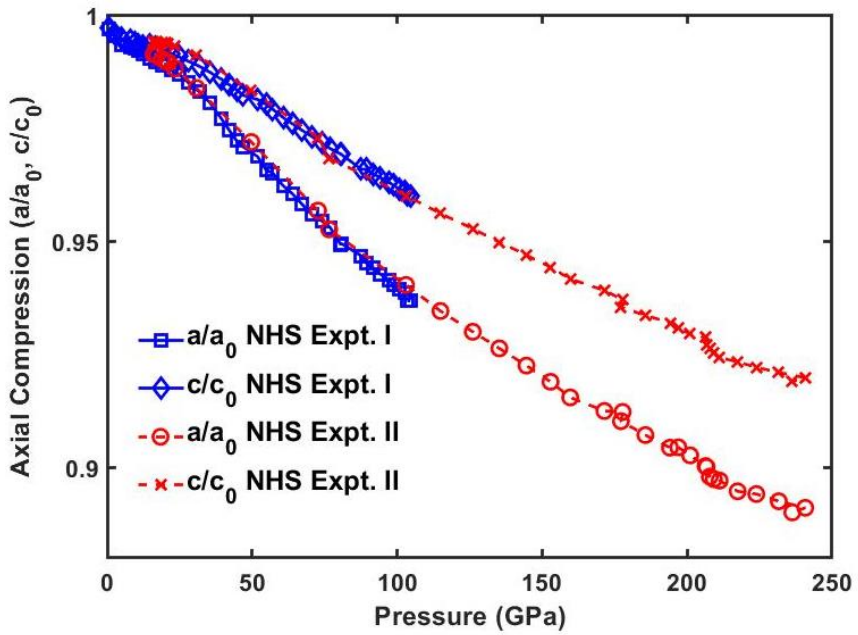


Figure 31. The axial compression of *a*-axis and *c*-axis of hexagonal $ReB_2$ to 241 GPa.

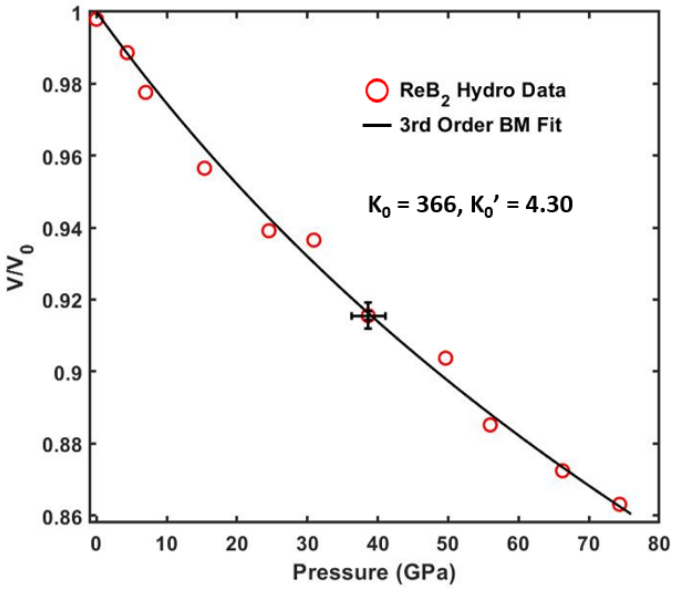


Figure 32. Hydrostatic compression curve of *ReB₂* to 75 GPa with derived bulk moduli values.

The excellent agreement in theory and NHS experiments gives promising insight to the mechanical strength and anisotropy of *ReB₂*, however, anisotropic compression effects had not been validated with hydrostatic measurements until the R-XRD experiments shown in this study. To verify the DFT calculations and compare with NHS experiments, R-XRD and LST were conducted on *ReB₂* in accordance with the experimental details in Chapter 7. The volumetric compression results from LST in Figure 32 reveal the hydrostatic equation of state fit to 75 GPa.

The derived bulk moduli values are in very good agreement with NHS and DFT calculations ($K_0$ = 360 GPa) with values $K_0 = 366\ GPa$ and $K_0' = 4.30$ with no region of uniaxial compression noted in the hydrostatic measurements. Axial compression measurements for the hydrostatic case shows encouraging validation of DFT calculations as the anisotropy is in similar magnitude between the *a* and *c*-axis (Figure 33). This

suggests that changes in electronic structure and interactions leads to anisotropy and high incompressibility in hexagonal $ReB_2$. This technique of R-XRD and LST application has indeed shown intriguing results as hydrostatic values of compression have been given to twice that of other literature values that were at best quasi-hydrostatic [54, 74].

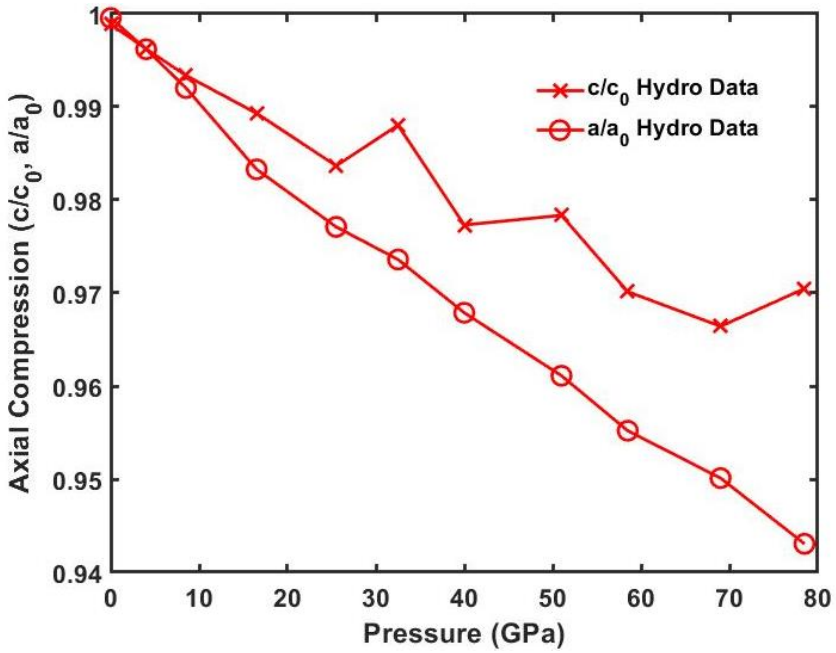


Figure 33. Hydrostatic axial compression of *a*-axis and *c*-axis for $ReB_2$ to 75 GPa.

### *9.5.3. Shear Strength Determination*

Previous DFT results showed the $C_{33}$ and $C_{11}$ elastic constants were enhanced with pressure at a larger rate than the other three ($C_{12}$, $C_{13}$, and $C_{44}$) [9]. This enhancement suggests a large shear strength. Chung et al. [54] showed differential stress measurements to 14 GPa, however, the differential stress was not shown to flatten to a maximum value at the low pressures. The R-XRD in this study has enabled a more comprehensive shear strength study to higher pressure to investigate the value of shear

strength for *ReB₂*. Again, the Voigt approximation was taken to determine a lower bound differential stress and strain $t = 6G < Q(hkl) >$. The measure d-spacings were determined for Rietveld refinement using MAUD software and the variation of d-spacings can be seen as a function of the azimuthal angle $\delta$ (Figure 34). At ambient values, we can see an obvious flatness to the d-spacing relative to the azimuthal angle, showing no strain effects. As pressure increases to the maximum, d-spacing is shown to vary because of the presence of differential stress. This differential stress *t* was determined by using a DFT calculation for the aggregate shear modulus *G* and refining the lattice strain *Q(hkl)* for the (002), (100), and (102) planes. The calculated differential stress *t* can be seen in Figure 35 up to 75 GPa with hydrostatic pressure determined by *Pt* pressure marker.

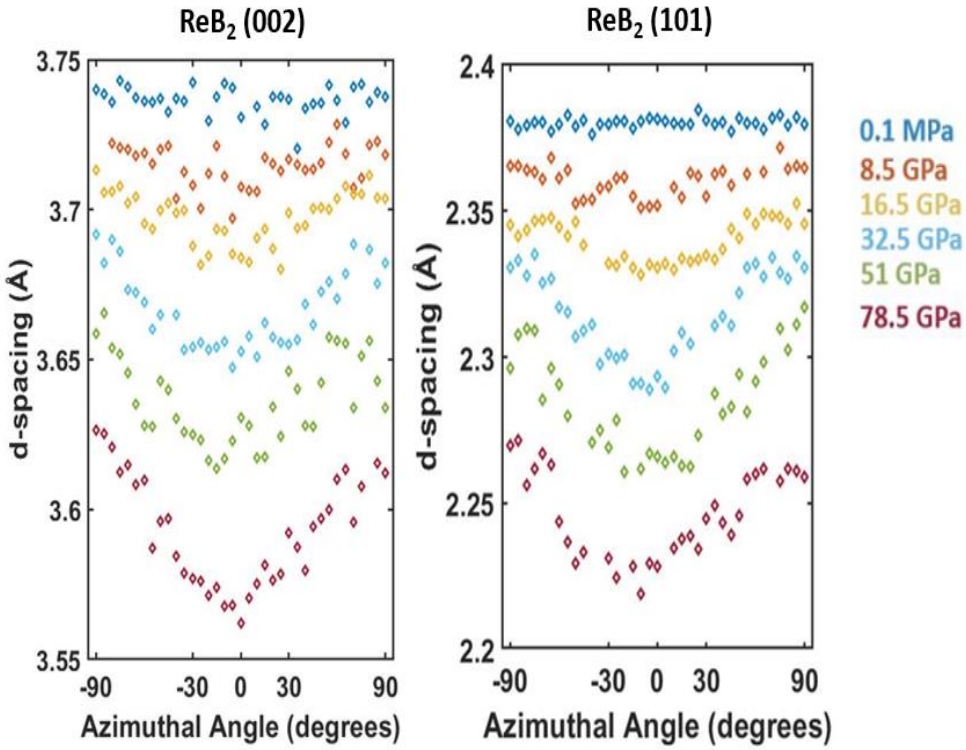


Figure 34. Variation of *ReB₂* d-spacings with azimuthal angle $\delta$ and at various pressures for the (002) diffraction plane and (101) diffraction plane.

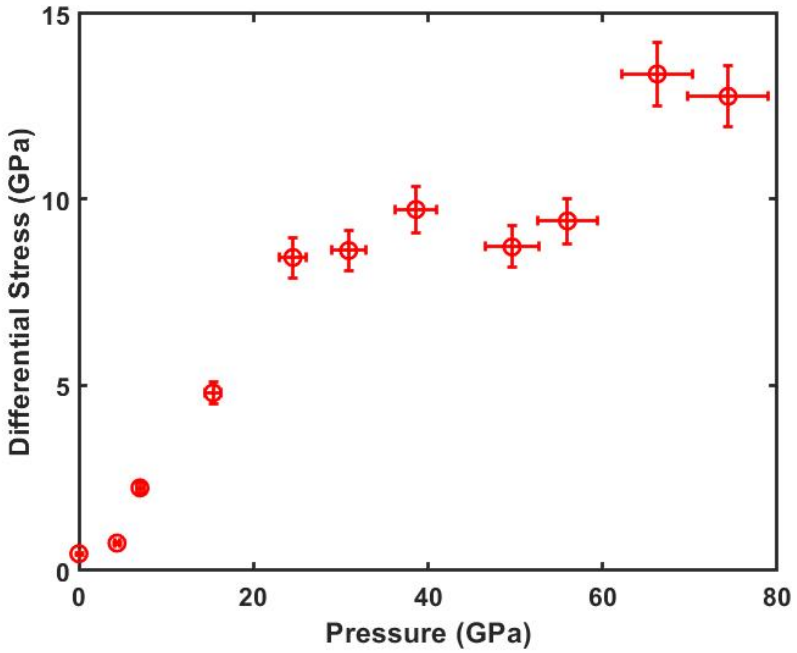

Figure 35. Differential stress of $ReB_2$ up to 78 GPa determined utilizing Pt as a pressure marker.

The differential stress was shown to increase with pressure and did not show a limiting value in the applied pressure range of 78 GPa. Indeed, this is very intriguing results as the most incompressible metal Os had already flattened to a limiting value of t ~ 12 GPa at an applied pressure of 50 GPa. This suggests that $ReB_2$ can support a larger load while maintaining less lattice strain. This is encouraging as to the effect interstitial *B*-atoms have on reducing plastic deformation as *Re* is inferior in mechanical properties to *Os*. compared to theory, however, $ReB_2$ is expected to have a shear strength $\tau \sim 45\ GPa$ based on the relation from the Frenkel Model $\tau \sim G/6$. From Figure 35, it is immediately obvious that experimental shear strength is at a much lower value $\tau = 6.7 \pm 0.4\ GPa$. As mentioned in *Os* shear strength studies, experimental results are typically lower due to imperfections in crystal structures. However, the lower values of *t* in the applied pressure range of 0-15 GPa are systemically lower (~3-4 GPa) than the

differential stress measurements from Chung et al. in the same pressure range [54]. The values from Chung et al. also display a more flat and linear profile with increasing pressure. The limiting pressure range and limited number of data points from Chung et al. make a direct comparison difficult. It is also important to note that the $ReB_2$ sample from Chung et al. was synthesized into a solid ingot while the $ReB_2$ in this study was of a powder form mixed with *Pt* powder and at that point was unclear in the difference this would have in measured shear strength. To address this new question of how differential stress varies with sample bulk properties, double compression shear strength measurements were conducted on $ReB_2$ with no Pt mixture and results are addressed in the following section.

### *9.5.4. Double Compression Effect on Shear Strength of $ReB_2$*

Double compression of $ReB_2$ was conducted to compress a powder $ReB_2$ sample (Compression 1) into a solid foil using a DAC for re-compression measurements (Compression 2). It is speculated that a weaker metal that has been incorporated into a mixture with a stronger metal will reduce the strength of the superior specimen. To ascertain this effect on $ReB_2$, *Pt* pressure marker was not incorporated into the sample for pressure calibration, but instead the hydrostatic EoS previously determined for $ReB_2$ to 78 GPa was used. Double compression of $ReB_2$ was done to 30 GPa each in R-XRD experiments. The overall compression of the sample can be seen in Figure 36. The 1$^{st}$ Compression decreased sample thickness by ~35 microns, while the 2$^{nd}$ Compression only saw a change ~ 10 microns, showing a more foil-like bulk property as compared to the powder $ReB_2$. In comparison, the strain $Q(hkl)$ for both compressions were

determined from Rietveld analysis in MAUD and plotted in Figure 37. The primary *hkl*s (002), (100), and (101) were chosen to compare with lattice strain values from Chung et al. [54] with the same family of planes. We can see that the lattice strain increases from (002), (100), and (101) respectively and is in the same agreement with the observations from Chung. This is also true for the second compression values of *Q(hkl)* for the same lattice planes with only a slight decrease in overall value for the second compression.

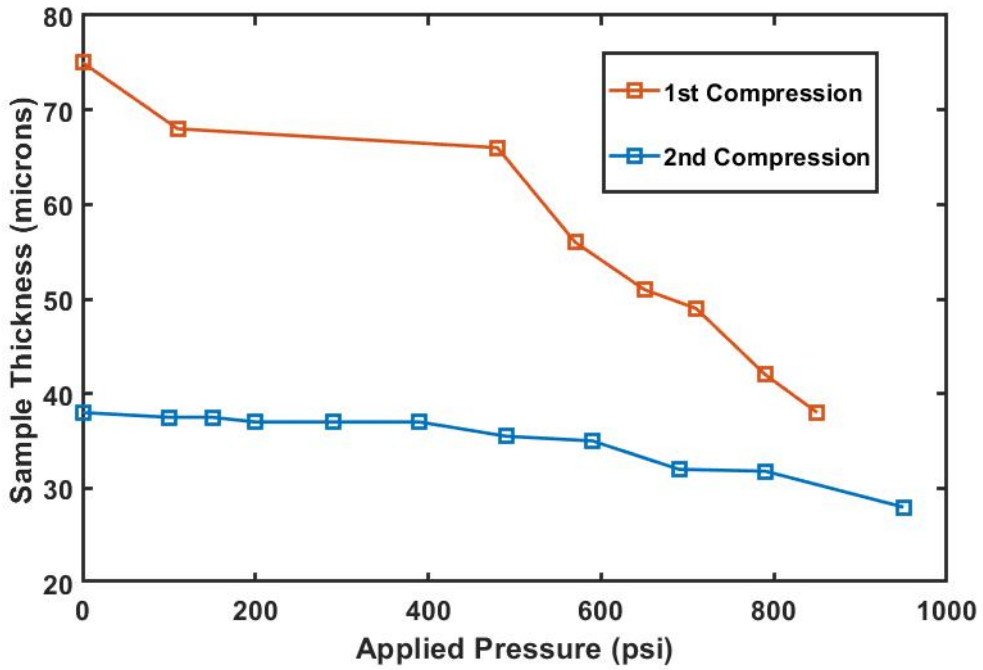


Figure 36. Sample thickness within the DAC for $ReB_2$ polycrystalline sample during 1st Compression followed by a pressure release and then a subsequent 2nd Compression.

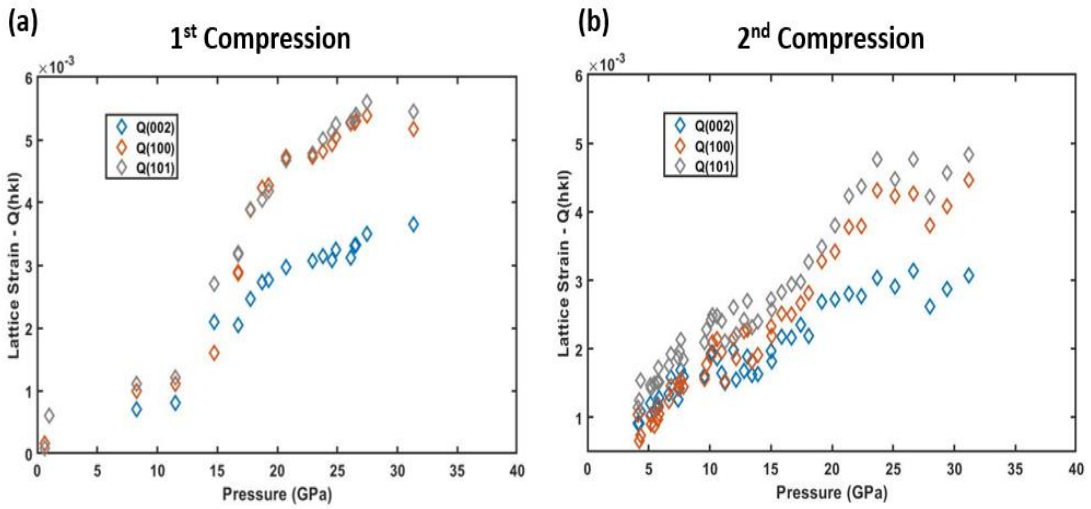


Figure 37. (a) Lattice strain values with increasing pressure for the planes (002), (100), and (101) for the 1st Compression. (b) 2nd compression lattice strain values for (002), (100), and (101) lattice planes.

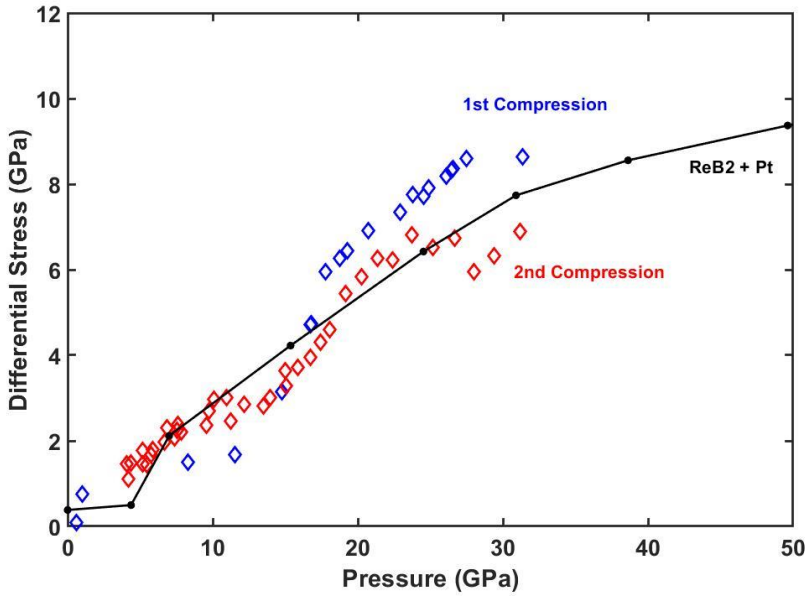


Figure 38. Differential stress for the 1st and 2nd Compression of $ReB_2$ sample plotted with previous differential stress measurements from the $ReB_2$-$Pt$ mixture.

By averaging the lattice strain terms for all three planes (002), (100), and (101) and using the relation $t = 6G < Q(hkl) >$, the differential stress was determined and plotted in Figure 38 up to 30 GPa. Surprisingly, the 2nd Compression differential stress

values were systemically lower than the 1st Compression powder sample, howbeit only slightly and are mostly in agreement. What is of more interest is whether the presence of *Pt* reduces the shear strength measurements of a sample. Indeed, this would cast serious doubt into previous R-XRD and LST studies into transition metals and their borides in this study. Plotted with the $ReB_2$ sample compressions in Figure 38 is the $ReB_2$-*Pt* sample differential stress from the previous experiments to 78 GPa (Figure 35). We can see there is good agreement between the two compressions of unmixed $ReB_2$ and that with homogenous mixing of *Pt*. This seems to suggest *Pt* has little effect on the shear strength in these studies, but further studies into $ReB_2$ sintered sample and various mixing of *Pt* would be needed to fully understand this.

### *9.5.5. Concluding Remarks on $ReB_2$ Studies*

$ReB_2$ has received extensive attention due to its high incompressibility, resistance to temperature, and ease of machining. However, no ultra-high pressure studies combined with DFT and high pressure shear strength measurements have been conducted until now. The robust analysis into $ReB_2$ that combined multiple XRD techniques and theory have provided in depth insight into the class of high strength materials under Aims 2 and 3 of this dissertation. This has resulted in two publications of $ReB_2$ studies [9,12] that provided comparison of non-hydrostatic and hydrostatic compression curves, validation of DFT calculations, and material strength. The broad and in-depth range of these studies will indeed prove useful for application of $ReB_2$ in high strength and extreme environments.

## 9.6. $Os_2B_3$ High Pressure and Temperature Studies

### *9.6.1. Introduction*

The high-pressure behavior of high strength and stable transition metals and TMBs have been the central focus of this dissertation. These studies into the hexagonal $Os_2B_3$ have offered first time electron and mechanical behavior to pressures equating to that at Earth's planetary core. Despite the similarity of hexagonal structure and B-atom packing in the crystal lattice, $Os_2B_3$ has received very little attention with only one high pressure study [57] and with virtually no HPHT studies. This indeed is surprising, as the bulk modulus is greater than even $ReB_2$ with $K_0$ ~ 395 GPa and is expected to have superb resistance to thermal degradation and shearing.

In this study, the compression behavior of high strength $Os_2B_3$ to a staggering 358 GPa using planar TDAC technology detailed in this dissertation. Anisotropy of lattice parameters is compared with DFT values for electron density distributions to ascertain the fundamental properties pf $Os_2B_3$ compression. This is concluded with first time HPHT studies to determine thermal expansion coefficients for $Os_2B_3$.

### *9.6.2. Toroidal DAC Compression of $Os_2B_3$ to 358 GPa*

The most successful T-DAC compression in this dissertation in terms of achieved pressure was in NHS compression of $Os_2B_3$ to 358 GPa using the planar design of TD-1. Ambient lattice parameters for the hexagonal crystal structure were determined here at the University of Alabama-Birmingham prior to compression studies and were $a_0$ = 2.915 Å and $c_0$ = 12.92 Å and were within 1% error of DFT calculations. The axial compression ratios $a/a_0$ and $c/c_0$ determined from Lebail Refinement and *Pt* pressure marker are

plotted in Figure 39 to the maximum achieved pressure and exhibit a similar increase in anisotropy as noted for $ReB_2$. For $Os_2B_3$, the axial compression $c/c_0$ was only ~9.5% compressed at 358 GPa which shows a similar incompressibility to $ReB_2$ $c/c_0$. As pressure is increased, saturation of axial compression is evident, as stiffness is also increased by interatomic interactions. This in good agreement with DFT calculations [8] that showed $a/a_0$ = 0.852 and $c/c_0$ = 0.916 where experimental results were 0.860 and 0.906 respectively, only ~1 % difference.

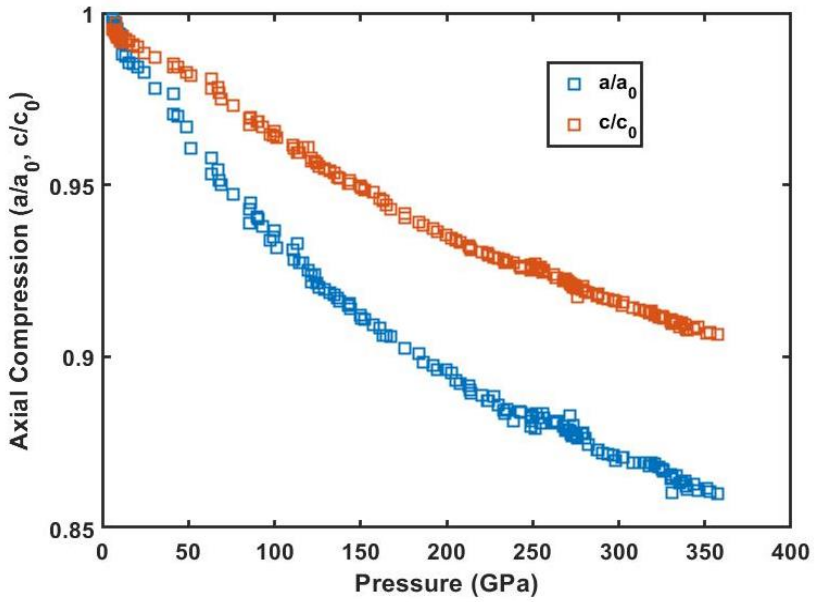


Figure 39. Axial compression ratios for $Os_2B_3$ hexagonal lattice to the maximum pressure of 358 GPa.

Axial compression values were then used to calculate volumetric compression curves to derive experimental bulk moduli of $Os_2B_3$. The NHS compression curve is plotted in Figure 40 and is well fitted with the 2nd Order BM EoS. The derived bulk modulus was an impressive $K_0$ = 397 GPa with the first pressure derivative held at the canonical value of $K_0$' = 4.0. Between the regions of 30-60 GPa the experimental

volumetric data is slightly elevated and is attributed to NHS effects. The theoretical results from DFT showed a bulk modulus of $K_0$ = 391.7 GPa which is again ~1% error

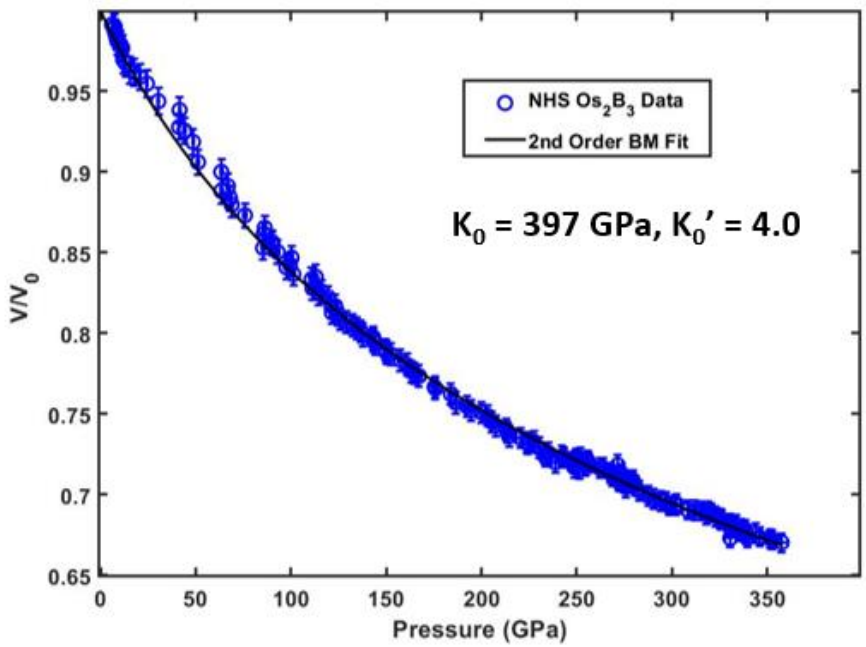


Figure 40. Experimental NHS compression curve of *$Os_2B_3$* to 358 GPa and fitted with the 2nd Order BM EoS.

It now interests to discuss the theoretical calculations in comparison to experimental observations to make conclusions into the electronic structures in *$Os_2B_3$* unit cell under pressure. The details of DFT calculations provided by the research group led by Dr. Cheng-Chien Chen at UAB can be found in the collaborative publication of HP EoS for *$Os_2B_3$* in reference [8]. Here, a summary of the DFT results is presented for comparison purposes. To begin, *$Os_2B_3$* unit cell can be pictured as a direct stacking of alternating layers of *Os* and *B* along the *c*-axis and offset stacking along the *a*-axis. This leads to high electron interactions along the *c*-axis when these bonds are shortened as compared to the a-axis. In DOS calculations, the covalent bonds between *Os-B* are enhanced with

pressure, resulting in a similar increase of $C_{33}$ and $C_{11}$ elastic constants as reported for $ReB_2$. The DFT elastic constants then were used to calculate pressure dependent ratio of bulk (K) and shear (G) moduli *G/K* to provide insight into the ductile or brittle nature of $Os_2B_3$. The results are displayed in Table 6.

Table 6
*DFT Calculations into G/K and Poisson Ratio for $Os_2B_3$*

| DFT Elastic Property | 0 GPa | 360 GPa |
|---|---|---|
| G/K | 0.564 | 0.457 |
| Poisson Ratio | 0.26 | 0.30 |

According to Pugh's criterion [87], if G/K > 0.571, then the specimen exhibits a more brittle nature. For $Os_2B_3$, we see that at ambient pressure G/K is < 0.571 showing it is more ductile with enhancement of ductility as it is lowered to G/K = 0.457 at 360 GPa. Also, this is further supported by Frantsevich's rule that states if the Poisson ratio > 1/3 then the material is ductile [88]. For $Os_2B_3$, we see it is lower than 1/3 but is increased with pressure indicating enhancement of ductility.

The rigid covalent *Os-B* bonds that are stacked along the *c*-axis indicates that the anisotropy between axial lattice parameters should favor the *c*-axis as being the most incompressible. Indeed, this is seen to be the case and results in a highly incompressible material ($K_0$ = 397 GPa, DFT-$K_0$ = 391.7 GPa) that favors ductility and stability. This suggests that $Os_2B_3$ may have a high hardness value as the directionally dependent bonds along the *c*-axis have high electron densities [8]. The sample in this experimental

observation was of a powder form and indentation experiments were not done. However, a Vicker's hardness of 15 GPa has been determined for $Os_2B_3$ at an applied load of ~ 5 N [52]. This is only a moderate hardness as super hard is only considered > 40 GPa but remains impressive in terms of incompressibility.

### *9.6.3. High Pressure – High Temperature Properties of $Os_2B_3$*

The thermoelastic behavior of $Os_2B_3$ has not been well studied despite the extensive thermal and electronic studies into the similar crystal structure of $ReB_2$. For HPHT calibration of $Os_2B_3$ volume changes, *in situ* EDXD measurements were taken at HPCAT beamline 16 BMB, Advanced Photon Source, Argonne National Laboratory. The experimental details can be sound in Chapter 7, Section 7.4.3.2 and is the only experiment in this dissertation that did not employ a DAC or TDAC. Instead, a large volume Paris Edinburgh (PE) press was used to accommodate high temperature application (≤ 1300 K). Simultaneous pressure–temperature EDCD measurements were conducted and analyzed using least squares fit to determine sample volume. Figure 41 displays the P-V-T curve up to the maximum temperature of 1273 K. For the application of the PE press, *MgO* pressure calibration was used [72].

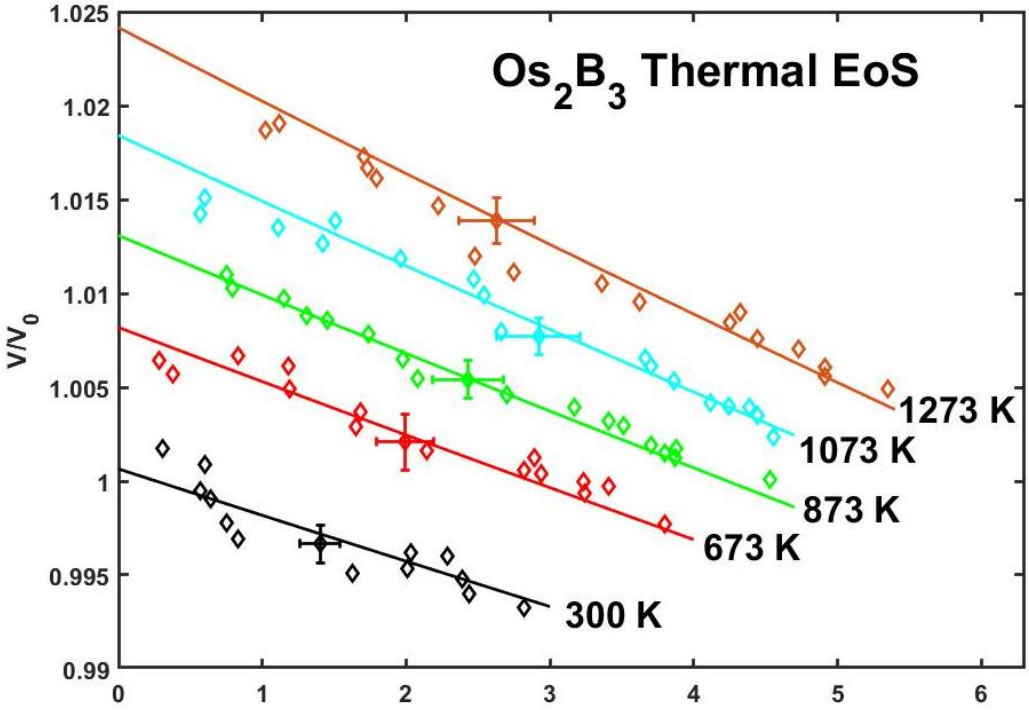


Figure 41. P-V-T curves for *Os₂B₃* to 1273 K and 5.5 GPa. The P-V-T data was fitted with the 3rd Order BM EoS and Fei Thermal Model to derive bulk-modulus and thermal expansion coefficients at high temperatures.

The P-V-T data of *Os₂B₃* was fitted with the 3rd Order BM EoS [80,81] and Fei Thermal Model [89] to determine the experimental bulk moduli and thermal expansion coefficients. Here, the thermal expansion is written in quadratic form to compare with DFT calculations and Equation 8.3:

$$\alpha = \alpha_0 + \alpha_1 T - \alpha_2 T^{-2}$$

where $\alpha_0$, $\alpha_1$, $\alpha_2$ are the thermal expansion coefficients and $T$ is temperature. Fitting of the data yielded $\alpha_0 = 1.862 \times 10^5\ K^{-1}$, $\alpha_0 = 3.31 \times 10^{-9}\ K^{-2}$, and $\alpha_0 = -0.640\ K$ with a measured ambient volume $V_0$ = 95.219 Å$^3$. This volume is slightly larger than the ambient volume measured for the T-DAC compression of *Os₂B₃* ($V_0$ = 95.076) and resulted in a smaller experimental bulk modulus calculation $K_0$ = 358 GPa and $K_0$' = 3.26. However, this is still consistent with other literature values [52, 89] and can be

attributed to the difference in non-hydrostatic (T-DAC) and quasi hydrostatic (PE press) conditions employed between the two studies. From the P-V-T curves, there is no indication of phase change or instability and is supported by the moderately low thermal expansion coefficients thus showing $Os_2B_3$ to be a superb material for HPHT applications.

Naturally, the change in axial *c/a* ratio is of interest to study regarding temperature effects due to previously noted anisotropy. For anisotropic nature in lattice parameters, *c/a* should increase with pressure, but is not seen in this case. Figure 42 shows the *c/a* ratio as a function of pressure and temperature and is mostly isotropic in nature This is most likely because of the low-pressure limit of the PE press not inducing structural anisotropy. The same ambient lattice parameters from the T-DAC compression experiment were used for *c/a* calculation as the $Os_2B_3$ sample used was from the same bulk material. DFT calculations into P-V-T curves and axial compression were provided by the theoretical research group at UAB headed by Dr. Cheng-Chien Chen. Detailed theoretical methods can be found in the collaborative publication of the same work presented here in reference [10].

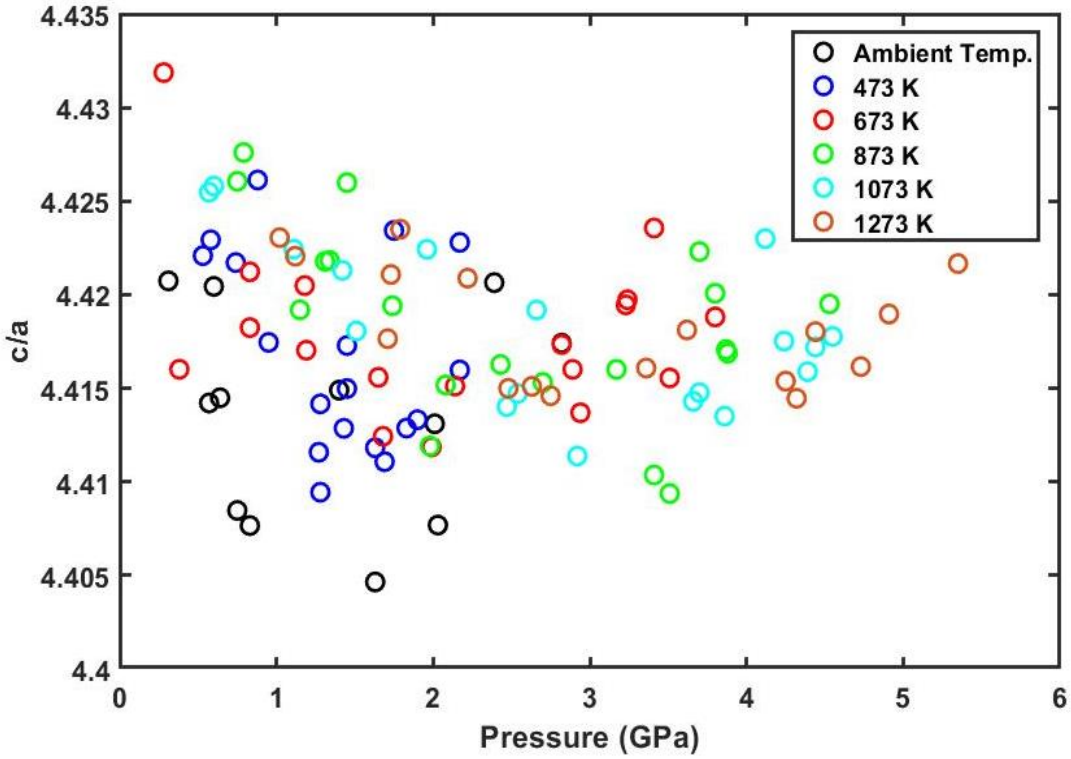


Figure 42. Axial compression ratio *c/a* for $Os_2B_3$ under simultaneous pressure, volume, and temperature. There is no discernable variation with temperature or pressure up to 6 GPa and 1273 K.

A comparison of theoretical and experimental values of $Os_2B_3$ thermal properties can be found in Table 7. It is seen that there is excellent agreement between DFT calculations and experimental observations on the physical and thermal properties of $Os_2B_3$. The calculated bulk modulus is only within 1% difference with DFT and similar lattice parameters are observed. The thermal expansion coefficients between DFT and experiments were also in very good agreement.

Table 7.
*Physical and Thermal Properties of $Os_2B_3$ by Experimental and DFT Calculations.*

| $Os_2B_3$ Properties | Experimental | DFT Calculation |
|---|---|---|
| Lattice Parameters | $a_0$ = 2.915 Å, $c_0$ = 12.92 Å | $a_0$ = 2.914 Å, $c_0$ = 12.860 Å |
| Volume | $V_0$ = 95.219 Å$^3$ | $V_0$= 94.55 Å$^3$ |
| Bulk Modulus | $K_0$ = 358 GPa | $K_0$ = 354 GPa |
| Thermal Expansion Coefficients | $\alpha_0 = 1.862 \times 10^5\ K^{-1}$, $\alpha_0 = 3.31 \times 10^{-9}\ K^{-2}$, $\alpha_0 = 0.640\ K$ | $\alpha_0 = 1.6356 \times 10^5\ K^{-1}$, $\alpha_0 = 2.9742 \times 10^{-9}\ K^{-2}$, $\alpha_0 = 0.4767\ K$ |

### *9.6.4. Conclusions of $Os_2B_3$ Physical and Thermal Properties*

Mechanical and thermal properties of *$Os_2B_3$* discussed in this dissertation have presented a unique look into *$Os_2B_3$* behavior in pressures replicating Earth's core and high temperatures for volatile environments. The derived bulk moduli from both experiment and DFT have revealed an ultra-incompressibility range of $K_0$ ~ 354 – 397 GPa that is within the range of other literature values [52,89]. The high resistance to compression coupled with moderately low thermal expansion suggests *$Os_2B_3$* is an excellent candidate for application into hypersonic engine devices, industrial tools, and reactors.

For future studies, it would be of high interest to apply LST and R-XRD techniques to ascertain the shear strength of *$Os_2B_3$*. The bulk modulus may be slightly higher than that of the similar compound *$ReB_2$*, but this does not necessitate to a high shear resistance. Indeed, hardness tests have only shown a moderate hardness of 15 GPa

[52] which may suggest some limit to its use as an abrasive. However, the highly directional electronic density along the *c*-axis would provide excellent applications into protective coatings. There is even some interest in *B*-atom rich TMBs as they have even been shown to provide neutron shielding comparable to water in reactors [90]. Determining shear strength and hydrostatic compression values would give further insight and validation of theory to the promising mechanical properties of $Os_2B_3$.

# CHAPTER 10

# CONCLUSION

## 10.1. Summary of Work

The major conclusions of research presented in this thesis are as follows:

- The hexagonal transition metal borides ($ReB_2$ and $Os_2B_3$) show anisotropic compression effects whereby *c*-axis is the less compressible than the *a*-axis of the unit cell. The anisotropic compression effects are also observed under true hydrostatic strain conditions and are therefore intrinsic to the electronic structure of these materials. The overlap of electron charge distribution along the *Metal-Boron* bond directed along the *c*-axis and consequent coulomb repulsion makes the *c*-axis relatively incompressible to the highest pressure of 358 GPa achieved in this study.
- The observed anomalies in the axial ratio (*c*/*a*) of the most incompressible metal osmium has been a long-standing debate in the scientific literature. Our hydrostatic compression studies via radial x-ray diffraction have clearly established that the anomalies in axial *c*/*a* ratio are a manifestation of non-hydrostatic conditions experienced by the sample. Under hydrostatic compression conditions, *c/a* axial ratio in osmium shows a monotonous increase with increasing pressure to 280 GPa.

- The experimentally measured differential stress (twice the shear strength) for $ReB_2$ shows a definite dependence on the crystallographic planes with (001) family of planes had the lowest shear strength and plane normal to the basal plane had the highest shear strength. The shear strength of Rhenium Diboride approaches 6.7 GPa at the highest pressure of 70 GPa.
- In all cases of transition metals and transition metal borides where shear strength data has been reported under high pressures, the experimentally measured values are considerably less than the theoretically predicted shear strength. For example, the experimentally measured shear strength of osmium reaches a limiting value of 6 GPa while the theoretical ideal shear strength is 24 GPa. This is due to crystal imperfections present in all polycrystalline materials used in this study which precludes achieving ideal shear strength values expected of perfect single crystalline materials.

The work presented in this dissertation has culminated in multiple publications and collaborations for in-depth studies into new tools and techniques for high pressure generation and new insights into the mechanical properties of transition metals and their borides under extreme environments. The success of these studies has already proven useful as *Ta* equation of state and x-ray diffraction data presented in this study has been used to determine shear strength of *Ta* to 276 GPa and shows good agreement with the strength data obtained by shock compression methods [15]. Cross collaborations between major national laboratories and the UAB high pressure and theoretical research groups have highlighted the ability of theory to accurately predict compression and deformation

behavior of transition metals and transition metal borides. The excitement within the high-pressure community to generate ~ 1TPa of pressure has driven studies into the development of novel design strategies for diamond anvils including nanocrystalline diamond micro-anvils as well as toroidal diamond anvils as documented in this thesis.

We have also demonstrated the viability of high strength materials such as *Os*, $ReB_2$, and $Os_2B_3$ for applications that require retention of mechanical properties and phase stability at high temperatures. The high pressure and high temperature resistance displayed in these materials has drawn interest as new industries into hypersonic travel and production of US-based fusion devices [91] has already caught attention to TMBs [90]. The in-depth studies into the electronic, mechanical, and high temperature behavior of $ReB_2$ and $Os_2B_3$ crystal structures has undoubtedly furthered the field of high strength materials by providing high standards of collaboration with theory and experiment that has provided accurate measurements of axial compression behavior and strength.

## 10.2. Future Studies

### *10.2.1. FIB Machined Toroidal Diamond Anvils*

The T-DACs presented in this study have shown more conservative limits of pressure application (265-360 GPa) than those of other studies claiming > 500 GPa [23,24,30,31]. Based on the equation of state for *Ta* in this dissertation and cross comparison with other studies, these high pressure claims with T-DACs > 500 GPa appear to be inflated [7,29]. Indeed, the limiting pressure of the DAC is not merely governed by the geometry and size of the load bearing surface but also to a large extent by the imperfections present in the diamond itself that can impact its shear strength. The

T-DACs in this study have shown an accurate pressure of up to 358 GPa [8] while those of Sakai et al. [28,29] produced > 430 GPa despite similarities in anvil culet dimensions. The major difference between the two anvils used is that those in this study were of single crystalline nature while Sakai et al. used nano-polycrystalline diamond with grain sizes < 10 nm. It has also been suggested that nano-crystalline diamond with small grain sizes is the key to achieving higher pressures [23,24].

*10.2.2. High Entropy Alloys and Borides*

The high strength and incompressibility of TMBs has brought much attention to incorporation of light covalent atoms into the crystal structures of transitions metals. Recently, this has been utilized in the field of High Entropy Alloys (HEAs) and High Entropy Borides (HEBs). An HEA is a metal alloy that contains five or more equimolar ratios of transitions metals that have been synthesized into one stable phase that has superior mechanical and thermal properties than that of its constituents [92]. The large entropy of mixing in this compound ensures high thermal stability by minimizing the Gibbs free energy. This revolutionary field of high-entropy alloys can be further strengthened by incorporation of *B*-atoms very similar to the TMBs in this study. The resulting metal, now called an HEB, has shown some superior physical qualities while maintaining lower weight than some TMBs [93]. This has brought considerable attention to the field of HEAs and HEBs and has not escaped the attention of the high pressure group here at UAB. We have already published a featured article in AIP Advances of HPHT work into $(Hf_{0.2}\ Ti_{0.2}\ Zr_{0.2}\ Ta_{0.2}\ Mo_{0.2})B_2$ and revealed its thermo-mechanical properties to be on par with $Os_2B_3$ despite the HEB containing weaker constituent

elements than *Os* [11]. This has led to many more studies into HPHT, HP, and shear strength studies currently in process of being completed on *Os* and other *Hf* based HEB compounds. This has facilitated a new research proposal for shock compression studies on these HEB compounds at the Sandia National Laboratory's Z-Machine and will further offer new and intriguing studies into deformation behavior of high-entropy materials.

# 11. REFERENCES


1. Aleksandrov, I. V., Goncharov, A. P., Makarenko, I. N., Zisman, A. N., Jakovenko, E. V., & Stishov, S. M. (1989). Diamond and cubic boron nitride under high pressure: Raman scattering, equation of state and high pressure scale. *High Pressure Research, 1*(5-6), 333–336. https://doi.org/10.1080/08957958908202491
2. Zhou, W., Wu, H., & Yildirim, T. (2007). Electronic, dynamical, and thermal properties of ultra-incompressible superhard rhenium diboride: A combined first-principles and neutron scattering study. *Physical Review B, 76*(18). https://doi.org/10.1103/physrevb.76.184113
3. Friedrich, A., Winkler, B., Juarez-Arellano, E. A., & Bayarjargal, L. (2011). Synthesis of binary transition metal nitrides, carbides, and borides from the elements in the laser-heated Diamond Anvil cell and their structure-property relations. *Materials*, *4*(10), 1648–1692. https://doi.org/10.3390/ma4101648
4. Hebbache, M., Stuparević, L., & Živković, D. (2006). A new superhard material: Osmium Diboride OSB2. *Solid State Communications*, *139*(5), 227–231. https://doi.org/10.1016/j.ssc.2006.05.041
5. Armentrout, M. M., & Kavner, A. (2010). Incompressibility of osmium metal at ultrahigh pressures and temperatures. *Journal of Applied Physics, 107*(9), 093528. https://doi.org/10.1063/1.3369283
6. Frotscher, M., Senyshyn, A., & Albert, B. (2012). Neutron diffraction at metal Borides, Ru2b3and OS2B3. *Zeitschrift Für Anorganische Und Allgemeine Chemie*, *638*(12-13), 2078–2080. https://doi.org/10.1002/zaac.201200350

7. Burrage, K. C., Perreault, C. S., Moss, E. K., Pigott, J. S., Sturtevant, B. T., Smith, J. S., Velisavljevic, N., & Vohra, Y. K. (2019). Ultrahigh pressure equation of state of tantalum to 310 GPa. *High Pressure Research*, *39*(3), 489–498. https://doi.org/10.1080/08957959.2019.1641203
8. Burrage, K. C., Lin, C.-M., Chen, W.-C., Chen, C.-C., & Vohra, Y. K. (2020). Electronic structure and anisotropic compression of OS2B3 to 358 GPA. *Journal of Physics: Condensed Matter*, *32*(40), 405703. https://doi.org/10.1088/1361-648x/ab9ae9
9. Burrage, K. C., Lin, C.-M., Chen, W.-C., Chen, C.-C., & Vohra, Y. K. (2020). Experimental and computational studies on Superhard material rhenium diboride under ultrahigh pressures. *Materials*, *13*(7), 1657. https://doi.org/10.3390/ma13071657
10. Burrage, K. C., Lin, C.-M., Chen, W.-C., Chen, C.-C., & Vohra, Y. K. (2020). Experimental and theoretical P-V-T equation of state for OS2B3. *High Pressure Research*, *41*(1), 27–38. https://doi.org/10.1080/08957959.2020.1858821
11. Iwan, S., Burrage, K. C., Storr, B. C., Catledge, S. A., Vohra, Y. K., Hrubiak, R., & Velisavljevic, N. (2021). High-pressure high-temperature synthesis and thermal equation of state of high-entropy transition metal boride. *AIP Advances*, *11*(3), 035107. https://doi.org/10.1063/5.0045592
12. Burrage, K. C., Park, C., & Vohra, Y. K. (2021). Shear strength measurements and hydrostatic compression of rhenium diboride under high pressures. *Journal of Applied Physics*, *129*(20), 205901. https://doi.org/10.1063/5.0050057

13. Lin, C. M., Burrage, K. C., Perreault, C., Chen, W.-C., Chen, C.-C., & Vohra, Y. K. (2021). Theoretical and experimental studies of compression and shear deformation behavior of osmium to 280 GPa. *Engineering Research Express*. https://doi.org/10.1088/2631-8695/ac34c4
14. Burrage, K.C., Baker P, Vohra Y.K. (2021) Lattice Strain Analysis and Hydrostatic Equation of State for Ti-6Al-4V using Radial X-ray diffraction. *High Pressure Research. Submission Pending.*
15. Perreault C., Huston L., Burrage K., Couper S., Miyagi L., Moss E., Pigott J., Velisavljevic N., Vohra Y., Smith J., Sturtevant B. Strength of tantalum to 276 GPa determined by two x-ray diffraction techniques using diamond anvil cells. *Journal of Applied Physics. Submission Pending*
16. Eremets, M. I., Trojan, I. A., Gwaze, P., Huth, J., Boehler, R., & Blank, V. D. (2005). The strength of diamond. *Applied Physics Letters*, *87*(14), 141902. https://doi.org/10.1063/1.2061853
17. Aleksandrov, I.V., et al., *Diamond at high pressures: Raman scattering of light, equation of state, and highpressurescale.* Sov. Phys. JETP, 1987. **66**: p. 384.
18. Piermarini, G. J. (2001). High pressure x-ray crystallography with the diamond cell At nist/nbs. *Journal of Research of the National Institute of Standards and Technology*, *106*(6), 889. https://doi.org/10.6028/jres.106.045
19. Snider, E., Dasenbrock-Gammon, N., McBride, R., Debessai, M., Vindana, H., Vencatasamy, K., Lawler, K. V., Salamat, A., & Dias, R. P. (2020). Room-temperature superconductivity in a carbonaceous sulfur hydride. *Nature*, *586*(7829), 373–377. https://doi.org/10.1038/s41586-020-2801-z

20. Ho-kwang Mao and Russell J Hemley. The high-pressure dimension in earth and planetary science. Proceedings of the National Academy of Sciences, 104(22):9114–9115, 2007. ISSN 0027-8424. doi: 10.1073/pnas.0703653104.
21. Bragg, W. L. (1966). The diffraction of short electromagnetic waves by a Crystal. Proceedings of the Cambridge Philosophical Society, 17, 43–57 (1913). communicated by professor sir J. J. Thomson. read 11 November 1912. *X-Ray and Neutron Diffraction*, 109–125.
22. Wootton, K.P., Cheng, W., Decker, G., Lee, S.H., Yang, X.B. X-ray Beam Size Monitor Enclosure for the Advanced Photon Source Upgrade. 9th Int. Beam Instrum, conf. (2020).
23. Dubrovinsky, L., Dubrovinskaia, N., Prakapenka, V. B., & Abakumov, A. M. (2012). Implementation of micro-ball Nanodiamond Anvils for high-pressure studies above 6 mbar. *Nature Communications*, *3*(1). https://doi.org/10.1038/ncomms2160
24. Dubrovinskaia, N., Dubrovinsky, L., Solopova, N. A., Abakumov, A., Turner, S., Hanfland, M., Bykova, E., Bykov, M., Prescher, C., Prakapenka, V. B., Petitgirard, S., Chuvashova, I., Gasharova, B., Mathis, Y.-L., Ershov, P., Snigireva, I., & Snigirev, A. (2016). Terapascal static pressure generation with ultrahigh yield strength nanodiamond. *Science Advances*, *2*(7).
25. Moore, S. L., Samudrala, G. K., Catledge, S. A., & Vohra, Y. K. (2018). Rapid growth OF Nanocrystalline diamond on single crystal diamond for studies on materials under extreme conditions. *Scientific Reports*, *8*(1).

26. Samudrala, G. K., Moore, S. L., Velisavljevic, N., Tsoi, G. M., Baker, P. A., & Vohra, Y. K. (2016). Nanocrystalline diamond Micro-anvil grown on single crystal diamond as a generator of ultra-high pressures. *AIP Advances, 6*(9), 095027.
27. Lobanov, S. S., Prakapenka, V. B., Prescher, C., Konôpková, Z., Liermann, H.-P., Crispin, K. L., Zhang, C., & Goncharov, A. F. (2015). Pressure, stress, and strain distribution in the double-stage Diamond Anvil Cell. *Journal of Applied Physics, 118*(3), 035905. https://doi.org/10.1063/1.4927213
28. Sakai, T., Yagi, T., Ohfuji, H., Irifune, T., Ohishi, Y., Hirao, N., Suzuki, Y., Kuroda, Y., Asakawa, T., & Kanemura, T. (2015). High-pressure generation using double stage micro-paired diamond anvils shaped by focused ion beam. *Review of Scientific Instruments, 86*(3), 033905. https://doi.org/10.1063/1.4914844
29. Sakai, T., Yagi, T., Irifune, T., Kadobayashi, H., Hirao, N., Kunimoto, T., Ohfuji, H., Kawaguchi-Imada, S., Ohishi, Y., Tateno, S., & Hirose, K. (2018). High pressure generation using double-stage diamond anvil technique: Problems and equations of state of rhenium. *High Pressure Research, 38*(2), 107–119. https://doi.org/10.1080/08957959.2018.1448082
30. Jenei, Z., O'Bannon, E. F., Weir, S. T., Cynn, H., Lipp, M. J., & Evans, W. J. (2018). Single Crystal toroidal diamond anvils for high pressure experiments beyond 5 megabar. *Nature Communications, 9*(1). https://doi.org/10.1038/s41467-018-06071-x
31. Dewaele, A., Loubeyre, P., Occelli, F., Marie, O., & Mezouar, M. (2018). Toroidal Diamond Anvil cell for detailed measurements under extreme static pressures. *Nature Communications, 9*(1). https://doi.org/10.1038/s41467-018-05294-2

32. Singh, A. K., Balasingh, C., Mao, H.-kwang, Hemley, R. J., & Shu, J. (1998). Analysis of lattice strains measured under nonhydrostatic pressure. *Journal of Applied Physics*, *83*(12), 7567–7575.

33. Merkel, S., Wenk, H. R., Shu, J., Shen, G., Gillet, P., Mao, H.-kwang, & Hemley, R. J. (2002). Deformation of polycrystalline mgo at pressures of the lower mantle. *Journal of Geophysical Research: Solid Earth*, *107*(B11). https://doi.org/10.1029/2001jb000920

34. Errandonea, D., Meng, Y., Somayazulu, M., & Häusermann, D. (2005). Pressure-induced transition in titanium metal: A systematic study of the effects of uniaxial stress. *Physica B: Condensed Matter*, *355*(1-4), 116–125. https://doi.org/10.1016/j.physb.2004.10.030

35. Pettifor, D. G. (1977). Theory of energy bands and related properties of 4D transition metals. I. Band parameters and their volume dependence. *Journal of Physics F: Metal Physics*, *7*(4), 613–633. https://doi.org/10.1088/0305-4608/7/4/013

36. Buckman, R. W. (2000). New applications for tantalum and tantalum alloys. *JOM*, *52*(3), 40–41. https://doi.org/10.1007/s11837-000-0100-6

37. Sakai, T., Yagi, T., Irifune, T., Kadobayashi, H., Hirao, N., Kunimoto, T., Ohfuji, H., Kawaguchi-Imada, S., Ohishi, Y., Tateno, S., & Hirose, K. (2018). High pressure generation using double-stage diamond anvil technique: Problems and equations of state of rhenium. *High Pressure Research*, *38*(2), 107–119. https://doi.org/10.1080/08957959.2018.1448082

38. Anzellini, S., Dewaele, A., Occelli, F., Loubeyre, P., & Mezouar, M. (2014). Equation of state of rhenium and application for ultra-high pressure calibration. *Journal of Applied Physics*, *115*(4), 043511. https://doi.org/10.1063/1.4863300

39. Cynn, H., Klepeis, J. E., Yoo, C.-S., & Young, D. A. (2002). Osmium has the lowest experimentally determined compressibility. *Physical Review Letters*, *88*(13). https://doi.org/10.1103/physrevlett.88.135701

40. Dubrovinsky, L., Dubrovinskaia, N., Bykova, E., Bykov, M., Prakapenka, V., Prescher, C., Glazyrin, K., Liermann, H.-P., Hanfland, M., Ekholm, M., Feng, Q., Pourovskii, L. V., Katsnelson, M. I., Wills, J. M., & Abrikosov, I. A. (2015). The most incompressible metal osmium at static pressures above 750 gigapascals. *Nature*, *525*(7568), 226–229. https://doi.org/10.1038/nature14681

41. Kenichi, T. (2004). Bulk modulus of osmium: High-pressure powder X-ray diffraction experiments under quasihydrostatic conditions. *Physical Review B*, *70*(1). https://doi.org/10.1103/physrevb.70.012101

42. Occelli, F., Farber, D. L., Badro, J., Aracne, C. M., Teter, D. M., Hanfland, M., Canny, B., & Couzinet, B. (2004). Publisher's note: Experimental evidence for a high-pressure isostructural phase transition in osmium [phys. rev. lett.93, 095502 (2004)]. *Physical Review Letters*, *93*(10). https://doi.org/10.1103/physrevlett.93.109901

43. Perreault, C. S., Velisavljevic, N., & Vohra, Y. K. (2017). High-pressure structural parameters and equation of state of osmium to 207 GPA. *Cogent Physics*, *4*(1), 1376899. https://doi.org/10.1080/23311940.2017.1376899

44. Occelli, F., Farber, D. L., Badro, J., Aracne, C. M., Teter, D. M., Hanfland, M., Canny, B., & Couzinet, B. (2004). Experimental evidence for a high-pressure isostructural phase transition in osmium. *Physical Review Letters*, *93*(9). https://doi.org/10.1103/physrevlett.93.095502

45. Dubrovinsky, L., Dubrovinskaia, N., Bykova, E., Bykov, M., Prakapenka, V., Prescher, C., Glazyrin, K., Liermann, H.-P., Hanfland, M., Ekholm, M., Feng, Q., Pourovskii, L. V., Katsnelson, M. I., Wills, J. M., & Abrikosov, I. A. (2015). The most incompressible metal osmium at static pressures above 750 gigapascals. *Nature*, *525*(7568), 226–229. https://doi.org/10.1038/nature14681

46. Kenichi, T. (2004). Bulk modulus of osmium: High-pressure powder X-ray diffraction experiments under quasihydrostatic conditions. *Physical Review B*, *70*(1). https://doi.org/10.1103/physrevb.70.012101

47. Goosey R.E. Metals and Materials; 1989. Chapter 5; p. 451–454

48. Wessel, J.K. (2004). *Handbook of Advanced Materials*. Wiley J & Sons. (Print ISBN: 9780471454755 - Online ISBN: 9780471465188) Chapter 8

49. Jacobs J.J., Sumner D.R., Galante J.O. (1993). Mechanisms of Bone Loss Associated with Total Hip Replacement. *Orthopedic Clinics of North America*. 24:583–588.

50. Nagamatsu, J., Nakagawa, N., Muranaka, T., Zenitani, Y., & Akimitsu, J. (2001). Superconductivity at 39 K in magnesium diboride. *Nature*, *410*(6824), 63–64. https://doi.org/10.1038/35065039

51. Xie, Z., Lugovy, M., Orlovskaya, N., Graule, T., Kuebler, J., Mueller, M., Gao, H., Radovic, M., & Cullen, D. A. (2015). Hexagonal OsB2: Sintering, microstructure,

and mechanical properties. *Journal of Alloys and Compounds*, *634*, 168–178. https://doi.org/10.1016/j.jallcom.2015.01.291

52. Gu, Q., G. Krauss, and W. Steurer. (2008) Transition Metal Borides: Superhard versus Ultra-incompressible. *Advanced Materials. **20**: p. 3620-3626*.
53. Zhou, W., H. Wu, and T. Yildirim. (2007). Electronic, dynamical, and thermal properties of ultra-incompressible superhard rhenium diboride: A combined first-principles and neutron scattering study. *Physical Review B, **76**: p. 184113.*
54. Chung, H.-Y., et al., *Synthesis of Ultra-Incompressible Superhard Rhenium Diboride at Ambient Pressure.* Science, 2007. **316**: p. 436-439.
55. Chrzanowska, J., et al. (2015). The effect of process parameters on rhenium diboride films deposited by PLD. *Surface and Coatings Technology, **277**: p. 15-22.*
56. Lazar, P., X.-Q. Chen, and R. Podloucky. (2009) First-principles modeling of hardness in transition-metal diborides. *Physical Review B, **80**: p. 012103.*
57. Frotscher, M., Senyshyn, A., and Albert B. (2012). Neutron diffraction at metal borides, Ru2B3 and Os2B3 *Z. Anorg. Allg. Chem. 6382078–80*
58. *Advanced Photon Source Upgrade Project preliminary design ...* (n.d.). Retrieved November 16, 2021, from https://www-dev.aps.anl.gov/sites/default/files/APS-Uploads/Aps-Upgrade/Cover%20page%20and%20disclaimer.pdf.
59. *The advanced photon source a U.S. Department of Energy Office of Science User Facility*. Beamlines Information | Advanced Photon Source. (n.d.). Retrieved October 14, 2021, from https://www.aps.anl.gov/Beamlines/Directory/Details?beamline_id=43.

60. Park, C., Popov, D., Ikuta, D., Lin, C., Kenney-Benson, C., Rod, E., Bommannavar, A., & Shen, G. (2015). New developments in micro-x-ray diffraction and X-ray absorption spectroscopy for high-pressure research at 16-BM-D at the Advanced Photon Source. *Review of Scientific Instruments*, *86*(7), 072205. https://doi.org/10.1063/1.4926893
61. C. Park, D. Popov, D. Ikuta, C. Lin, C. Kenney-Benson, E. Rod, A. Bommannavar, and G. Shen. (2015). "New developments in micro-x-ray diffraction and x-ray absorption spectroscopy for high-pressure research at 16-BM-D at the advanced photon source," *Rev. Sci. Instrum. 86(7), 072205*.
62. The GIMP Development Team. (2019). *GIMP*. Retrieved from https://www.gimp.org
63. Dorogokupets, P. I., & Dewaele, A. (2007). Equations of state of mgo, AU, Pt, NaCl-B1, and NaCl-B2: Internally consistent high-temperature pressure scales. *High Pressure Research*, *27*(4), 431–446. https://doi.org/10.1080/08957950701659700
64. Dubrovinsky, L., Dubrovinskaia, N., Prakapenka, V. B., & Abakumov, A. M. (2012). Implementation of micro-ball Nanodiamond Anvils for high-pressure studies above 6 mbar. *Nature Communications*, *3*(1). https://doi.org/10.1038/ncomms2160
65. Anzellini, S., Dewaele, A., Occelli, F., Loubeyre, P., & Mezouar, M. (2014). Equation of state of rhenium and application for ultra high pressure calibration. *Journal of Applied Physics*, *115*(4), 043511. https://doi.org/10.1063/1.4863300
66. Prescher C, Prakapenka VB. DIOPTAS: a program for reduction of two-dimensional X-ray diffraction data and data exploration. High Press Res. 2015;35(3):223–230.

67. Toby, B. H., & Von Dreele, R. B. (2013). GSAS-II: The Genesis of a modern open-source all-purpose crystallography software package. *Journal of Applied Crystallography*, *46*(2), 544–549. https://doi.org/10.1107/s0021889813003531

68. Vinet, P., Ferrante, J., Rose, J. H., & Smith, J. R. (1987). Compressibility of Solids. *Journal of Geophysical Research*, *92*(B9), 9319. https://doi.org/10.1029/jb092ib09p09319

69. MCQUEEN, R. G., MARSH, S. P., TAYLOR, J. W., FRITZ, J. N., & CARTER, W. J. (1970). The equation of state of solids from Shock Wave Studies. *High-Velocity Impact Phenomena*, 293–417. https://doi.org/10.1016/b978-0-12-408950-1.50012-4

70. L. Lutterotti, S. Matthies, and H. Wenk, in MAUD: a friendly Java program for material analysis using diffraction, 1999.

71. Yokoo, M., Kawai, N., Nakamura, K. G., Kondo, K.-ichi, Tange, Y., & Tsuchiya, T. (2009). Ultrahigh-pressure scales for gold and platinum at pressures up to 550 GPA. *Physical Review B*, *80*(10). https://doi.org/10.1103/physrevb.80.104114

72. Kono, Y., Irifune, T., Higo, Y., Inoue, T., & Barnhoorn, A. (2010). P□V□T relation of mgo derived by simultaneous elastic wave velocity and in situ X-ray measurements: A new pressure scale for the mantle transition region. *Physics of the Earth and Planetary Interiors*, *183*(1-2), 196–211. https://doi.org/10.1016/j.pepi.2010.03.010

73. Kono, Y., Park, C., Sakamaki, T., Kenny-Benson, C., Shen, G., & Wang, Y. (2012). Simultaneous structure and elastic wave velocity measurement of Sio2 glass at high pressures and high temperatures in a Paris-edinburgh cell. *Review of Scientific Instruments*, *83*(3), 033905. https://doi.org/10.1063/1.3698000

74. Kavner, A., Armentrout, M. M., Rainey, E. S., Xie, M., Weaver, B. E., Tolbert, S. H., & Kaner, R. B. (2011). Thermoelastic properties of reb2 at high pressures and temperatures and comparison with pt, OS, and re. *Journal of Applied Physics*, *110*(9), 093518. https://doi.org/10.1063/1.3657776

75. Liu, X., Liu, W., He, Q., Deng, L.-W., Wang, H.-J., He, D.-W., & Li, B.-S. (2011). Isotropic thermal expansivity and anisotropic compressibility of reb 2. *Chinese Physics Letters*, *28*(3), 036401. https://doi.org/10.1088/0256-307x/28/3/036401

76. Rietveld, H. M. (1969). A profile refinement method for nuclear and magnetic structures. *Journal of Applied Crystallography*. **2** (2): 65–71. doi:10.1107/S0021889869006558.

77. LeBail, A (2005). Whole Powder Pattern Decomposition Methods and Applications: A Retrospection. *Powder Diffraction*. **20**: 316. doi:10.1154/1.2135315

78. Vaitkus, A., Merkys, A. & Gražulis, S. (2021). Validation of the Crystallography Open Database using the Crystallographic Information Framework. *Journal of Applied Crystallography*, *54*(2), 661-672.

79. Wenk, H. R., Matthies, S., & Lutterotti, L. (1994). Texture analysis from diffraction spectra. *Materials Science Forum*, *157-162*, 473–480. https://doi.org/10.4028/www.scientific.net/msf.157-162.473

80. Murnaghan, F. D. (1944). The Compressibility of Media under Extreme Pressures. *Proceedings of the National Academy of Sciences of the United States of America*. **30** (9): 244–247

81. Birch, F. (1947). Finite Elastic Strain of Cubic Crystals. *Physical Review*. **71** (11): 809–824.

82. Rydberg, R. (1931) Z. Phys. **73** 376–385.

83. Fei, Y. (1995) Thermal expansion in Mineral physics & crystallography: A handbook physical constants, T. Ahrens, ed. AGU, Washington DC, 29-44.

84. Shu-Jie, Y., Liang-Chen, C., & Chang-Qing, J. (2009). Hydrostaticity of pressure media in Diamond Anvil Cells. *Chinese Physics Letters*, *26*(9), 096202. https://doi.org/10.1088/0256-307x/26/9/096202

85. Klotz, S., Chervin, J.-C., Munsch, P., & Le Marchand, G. (2009). Hydrostatic limits of 11 pressure transmitting media. *Journal of Physics D: Applied Physics*, *42*(7), 075413. https://doi.org/10.1088/0022-3727/42/7/075413

86. Gonzalez-Platas, J., Alvaro, M., Nestola, F., & Angel, R. (2016). EOSFIT7-GUI: A new graphical user interface for equation of state calculations, analyses, and teaching. *Journal of Applied Crystallography*, *49*(4), 1377–1382. https://doi.org/10.1107/s1600576716008050

87. Pugh, S. F. (1954). XCII. relations between the Elastic Moduli and the plastic properties of polycrystalline pure metals. *The London, Edinburgh, and Dublin Philosophical Magazine and Journal of Science*, *45*(367), 823–843. https://doi.org/10.1080/14786440808520496

88. Frantsevich, I.N. (1983) *Elastic Constants and Elastic Moduli of Metals and Insulators Handbook* (Kiev: Naukova Dumka).

89. Ozisik, H., Deligoz, E., Surucu, G., & Ozisik, H. B. (2016). Anisotropic elastic and vibrational properties of Ru2B3and OS2B3: A First-principles investigation. *Materials Research Express*, *3*(7), 076501. https://doi.org/10.1088/2053-1591/3/7/076501

90. Windsor, C. G., Astbury, J. O., Davidson, J. J., McFadzean, C. J. R., Morgan, J. G., Wilson, C. L., & Humphry-Baker, S. A. (2021). Tungsten boride shields in a spherical tokamak fusion power plant. *Nuclear Fusion*, *61*(8), 086018. https://doi.org/10.1088/1741-4326/ac09ce.
91. *ITER project*. US ITER. (n.d.). Retrieved November 3, 2021, from https://www.usiter.org/resources/iter-project.
92. George, E. P., Raabe, D., & Ritchie, R. O. (2019). High-entropy alloys. *Nature Reviews Materials*, *4*(8), 515–534. https://doi.org/10.1038/s41578-019-0121-4
93. Gild, J., Zhang, Y., Harrington, T., Jiang, S., Hu, T., Quinn, M. C., Mellor, W. M., Zhou, N., Vecchio, K., & Luo, J. (2016). High-entropy metal diborides: A new class of high-entropy materials and a new type of Ultrahigh Temperature Ceramics. *Scientific Reports*, *6*(1). https://doi.org/10.1038/srep37946